공학박사 학위논문

Multifunctional Hybrids Based on Organosilicate Nanomaterials and Their Applications

유기실리케이트 기반의 다기능성 하이브리드의 제조 및 응용에 관한 연구

2013 년 2 월

서울대학교 대학원

공과대학 화학생물공학부

우 희 제

Abstract

Multifunctional Hybrids Based on Organosilicate Nanomaterials and Their Applications

Heeje Woo

School of Chemical and Biological Engineering

The Graduate School

Seoul National University

Ogranosilicates (OS) are silicon oxide-based materials including organic moieties. Due to the coexistence of silicon oxide frameworks and organic moieties, OS have material properties of silicon oxide and functionalities of organic functional groups at the same time. OS have received intense attention in several decades due to their distinguished material properties such as excellent optical transparency, high thermal and optical stability, processibility, tunability, and biocompatibility. In recent years, hollow silica shells (HSSs), spherical silica colloids with hollow inner space, have been thoroughly investigated due to their unique properties such as hollow inner space, large surface area, low thermal and electrical conductivity, low density. In this

thesis, we present novel multifunctional hybrids based on OS nanomaterials such as OS polymeric ligands and HSSs and their optical, optoelectronic, and thermally insulating applications.

In the first part of the thesis (Chapter 2), a simple method to prepare robust, processible, and bright quantum dot/organosilicate (QD/OS) hybrid films with improved QD distribution within OS matrices using thiol-containing polymeric OS ligands are presented. The surfaces of QDs, initially covered with oleic acids, were modified with thiol-containing OS ligands by the simple ligand exchange. Since this simple surface modification of QDs neither includes any harmful chemicals causing damage to QDs nor requires any harsh process conditions, the QD/OS hybrid films with the uniform distribution of QDs within the OS matrices were obtained without losing any quantum efficiency and any emission spectral shift. We also demonstrated that the QD/OS hybrid films are readily processible (with unconventional imprint lithography) and show excellent optical transparency as well as enhanced environmental stability in hydrochloric acid.

In the second part (Chapter 3), transparent organosilicate hybrid films with thermally insulating and UV-blocking properties based on silica/titania hybrid hollow shells (STHs) are demonstrated. STHs are the attractive candidates to save energy as one of effective insulating materials due to low thermal conductivity originating from hollow inner space as well as the excellent UV-block characteristics of TiO_2. The HSSs were first prepared using poly(acrylic acid) (PAA) colloidal aggregates as templates, tetraethyl orthosilicate (TEOS) as a silica precursor, and ammonia hydroxide as a catalyst based on the

modified Stöber method. Nanoparticle-like TiO_2 outer layers were then coated on the surfaces of HSSs using titanium tetrabutoxide (TBOT) as a titania precursor. The STHs mixed with organosilicate matrices were deposited on glass substrates to realize thermally insulating and UV-blocking layers. The STH-containing organosilicate films show excellent heat- and UV-blocking capabilities, yet maintaining high transparency.

In the third part (Chapter 4), we propose simple and effective strategy for bowing-free and high quality GaN film growth based on HSS-coated sapphire substrates. HSSs were readily prepared by sol-gel reaction and HSS monolayers were uniformly deposited on large-aread sapphire substrates based on simple solution process. ELO of GaN films were successfully induced by HSSs playing the role of mask and the crystallinity of GaN films prepared using HSS-coated sapphire substrates were remarkably improved. In addition, irregular reflection by bumped texture of HSS-coated sapphire substrates and reduced refractive index of GaN film by hollow inner space reduced total internal reflection within GaN films. As a result, the internal and the external efficiency of GaN LEDs were improved with HSS-coated sapphire substrates. Furthermore, the compressive stress in GaN films were relaxed by deformation of HSS and wafer bowing problem on GaN films were relieved. With these advantages, bowing-free and highly efficient GaN LEDs were realized.

In the last part of the thesis (Chapter 5), Ag NP/ SiO_2 hybrid hollow shells (Ag/SiO_2 HHSs) with improved reflectivity and light absorption property are demonstrated. Ag NPs were directly grown on the PVP-coated PS NS surface

and SiO_2 shells were coated onto the Ag NP-decorated PS NS surface. The size and # density of Ag NPs grown on PS NS surface were tunable by varying the synthetic condition. Ag/SiO_2 HHSs prepared presented distinguished optical properties. Ag/SiO_2 HHSs showed improved reflectivity when compared with HSS without Ag NPs due to the high reflectivity of Ag NPs. Furthermore, the light absorbance of Ag NPs within Ag/SiO_2 HHSs was remarkably increased when compared with pristine Ag NPs by enhanced coupling effect of surface Plasmon resonance between Ag NPs within Ag/SiO_2 HHSs.

Keywords: organosilicate(s), hybrid(s), hollow silica shell(s), LED(s), GaN, optical (device), optoelectronic (device), thermal insulator, Ag (nanoparticle)

Student Number: 2006-21360

Contents

List of Tables

List of Figures

Chapter 1. Introduction

1. 1. Organosilicates

Ogranosilicates (OS) are silicon oxide-based materials including organic moieties. Due to the coexistence of silicon oxide frameworks and organic moieties, organosilicates have material properties of silicon oxide and functionalities of organic functional groups at the same time.[1] OS oligomers and polymers can be easily synthesized by sol-gel method using silica precursor and acid or base catalyst.[2] In addition, the composition of organosilicates is tunable by varying the silica precursors.[3] There are various kinds of silica precursors including functional groups such as alkyl chains, amines, carboxylic acids, thiols, phenyl rings, halides, and so on. Thus, we can incorporate such functional groups within organosilicates and functionalized organosilicates can be prepared for specific applications. For example, we can make OS polymers containing phenyl groups can be prepared using phenyl-containing silica precursor such as phenyltrimethoxy silane (PTMS) and the amount of phenyl groups can be manipulated by control of PTMS feed ratio. The morphology and physical properties of organosilicates can be also manipulated. Particular, mesoporous OS materials were thoroughly investigated for low-k materials.[4-7] Many research groups have reported mesoporous OS films by embedding porogen, pore-generating moiety, within OS matrices.

Organosilicates have various advantages on their processibility. Organosilicates were solution processible and OS thin films can be deposited by simple spin casting process.[8,9] We can prepare uniform and large-area OS thin films using convenient spin casting facilities. The thickness of OS films can be manipulated ranging from several tens of nanometers to several micrometers by control of OS concentration in OS solution and spin rate. OS thin films have been applied to photolithographic process due to their distinguished etch resistance. The etch rate of organosilicates under O_2 plasma or F-based plasma is far different from one of the conventional photoresist materials. Thus, OS thin films have been used as a hardmask, etch barrier, in the bilayer and trilayer photoresist systems for the fabrication process of highly integrated semiconductor.[8,9] Moreover, OS films can be readily patterned by unconventional lithography.[10] Because the complex process and large equipments are not needed for unconventional lithography, we can prepare uniform OS patterns at a low cost with unconventional lithography.

Organosilicates show high optical transparency in the visible light range.[11] Due to the high transparency, organosilicates have attracted much attention as promising candidates for optical devices. Many research groups used organosilicates as matrix materials for phosphors such as organic & inorganic dyes and light-emitting nanocrystals. By incorporating within organosiicate matrices, the phosphors can be protected from environmental stimuli and can be formed to the films and the colloids.

Organosilicates have high thermal stability when compared with organic materials.[12-14] Organosilicates can endure high temperature higher than 1000 ℃

without thermal decomposition of silicate domains. Thus, organosilicates, typically OS particles, have been often blended with polymer matrices to enhance the thermal stability of polymer matrices. Many research groups have reported the thermally stable polymer/organosilicate nanocomposites and their practical applications. Furthermore, organosilicates have high optical stability when compared with organic materials which are easily degradable under UV exposure. Organosilicates can endure optical stimuli such as UV without optical degradation and long-term yellowing problem which occurs with epoxy-based matrices.

Organosilicates also have a advantage of biocompatibility.[15] Organosilicates are non-toxic materials for living organisms, so OS nanomaterials can be applied to biomedical applications. Nano-medicines such as drug-containing nanocapsules for controlled release based on organosilicate nanomaterials have been reported by numerous research groups. They introduced hollow silica shells as a nano-container for drug delivery system due to the biocompatibility of silica.

With these advantages, organosilicates have been applied to practical application in various industrial fields. All of them, the semiconductor industry is a representative field of commercial application of organosilicates. In the fabrication process of semiconductor, organosilicates were used as hardmasks for photolithography and low-k gapfill materials of patterned semiconductors. Organosilicate-based nanoobjects and nanohybrids have been also investigated for biomedical and optical applications at the moment.

1. 2. Hollow Silica Shells

Hollow silica shells (HSSs) are spherical silica colloids with hollow inner space. HSSs have been attracted a lot of attention due to their unique properties such as hollow inner space, large surface area, low thermal & electric conductivity, low density, biocompatibility.[16-19] Thus, numerous research groups have reported the preparation of multi-functional HSSs and their practical applications as nano-containers for drug delivery,[20-23] supporting materials for catalysts,[24-27] thermal insulators for heat management,[28,29] and light fillers for nanocomposites.[30]

In general, HSSs were prepared using organic/inorganic colloidal templates and sol-gel reaction of silica precursor based on stöber method.[30,31] For large-sized, ranging from several hundreds of nanometers to several tens of micrometers, HSSs, polymeric colloids such as PS and PMMA spheres are mainly used as templates.[32,33] SiO_2 shells are formed onto the surface of templates and polymeric templates are then removed by thermal degradation or solvent extraction leaving behind SiO_2 shells. For small-sized, several tens of nanometers, HSSs, small-sized templates such as metal/metal oxide nanoparticles, semiconductor nanocrystals, block copolymer micelles, and polymeric aggregates are used.[34-38] Sometimes, template-free synthetic methods are used to prepare HSSs. For example, template-free synthetic procedure of HSSs based on sol-gel reaction in water/oil emulsion,39 synthetic procedure based on difference of dissolution rate of SiO_2 spheres with composition gradient,[40] and self-templated route based on reaction

involving dissolution of SiO_2 core and redeposition of SiO_2 shell were reported.[41]

HSSs have various functionalities due to their hollow structure. Hollow inner space of HSSs can be used as a nano-container of functional materials such as nanomedicines and also applied a as nano-reactor for synthesis within confined space. In addition, HSSs can play the role of selective separator for metal nanoparticles which are easily mergable.[42] Furthermore, HSSs have multifunctional properties with their SiO_2 shells. We can incorporate functional nanomaterials within the SiO_2 shells or onto the surface of SiO_2 shells and surface property of SiO_2 shells can be readily manipulated by surface modification using silica precursors and polymer brushes. The material properties of SiO_2 shells such as porosity and mechanical strength can be also controlled by varying the synthetic condition of SiO_2 shells. Numerous research groups have reported multifunctional HSSs and their applications. For example, HSSs are to enable simultaneous targeting and imaging of specific substance using magnetic nanoparticles and light-emitting nanomaterials and controlled drug delivery system based on them.[17] In addition, hollow spheres with multilayered-shells can be realized based on HSSs.[43,44]

HSSs have a large surface area when compared with filled silica spheres due to their inner surface area. In the case of the HSSs with thin shells, total surface area of HSSs is almost as large as outer surface area. HSSs with a large surface area are good candidate of supporting materials for catalysts.[24-27] Generally, metal nanoparticles used as a catalyst such as Pt and Ag

nanoparticles were adsorbed on the surface of supporting materials to immobilize and avoid merging among the metal catalysts. At fixed volume of supporting materials, as the surface area of supporting materials increased, the amount of adsorbed catalysts also increased. Thus, we can prepare supporting materials with high catalyst content using HSSs when compared with filled silica spheres. And nano- and mesopores within the shell of HSSs enable to transfer small molecules in and outside of HSSs.[45]

HSSs have advantage of low density due to their hollow inner space containing large amount of trapped air. HSSs with low density are often applied to nanocomposites as light filler.[30] The nanocomposites containing HSSs have relatively low weight against volume. HSSs also have low thermal conductivity due to their hollow inner space.[28,29] Air is regarded as a representative of insulating material. For example, polystyrene form containing large amount of air has extremely low thermal conductivity and is widely applied to heat block system. HSSs are also containing large amount of air and their thermal conductivity is far lower than filled silica sphere. Indeed, commercial products based on HSSs such as insulating paints containing HSSs for preventing heat exchange between in and outside of buildings and insulating walls and doors containing HSSs for high performance refrigerators.

With these advantages, HSSs have been regarded as a promising candidate for multifunctional nanohybrid system. We can obtain various functionalities at the same time using HSSs and we can make novel functional hybrids based on HSSs.

In this thesis, we present novel multifunctional hybrid systems based on organosilicate nanomaterials such as OS polymeric ligands and HSSs. First, we prepared thiol-containing polymeric organosilicate ligands for homogeneous quantum dot/organosilicate (QD/OS) hybrid films with uniform QD distribution. The QD/OS hybrid films with uniform QD distribution showed improved quantum yield, environmental stability, and optical transparency as well as patternability by unconventional lithography. Second, we prepared HSSs using PS nanospheres and PAA colloidal aggregates as templates for multifunctional OS insulating films, high quality GaN film growth, and Ag/SiO_2 hybrid hollow shells. The multifunctional OS insulating films based on silica/titania hybrid hollow shells showed excellent heat- and UV-blocking capabilities, yet maintaining high transparency. GaN films grown on the HSSs-coated sapphire substrates showed improved crystallinity and device performance. Ag/SiO_2 hybrid hollow shells also showed enhanced optical properties when compared with HSSs without Ag nanoparticles.

1. 3. References

(1) Baney, R. H.; Itoh, M.; Sakakibara, A.; Suzuki, T. *Chem. Rev.* **1995**, *95*, 1409.

(2) Kudo, T.; Gordon, M. S. *J. Am. Chem. Soc.* **1998**, *120*, 11432.

(3) Suh, H. S.; Kang, H.; Liu, C.-C.; Nealey, P. F.; Char, K. *Macromolecules* **2010**, *43*, 461.

(4) Nguyen, C. V.; Carter, K. R.; Hawker, C. J.; Hedrick, J. L.; Jaffe, R. L.; Miller, R. D.; Remenar, J. F.; Rhee, H.-W.; Rice, P. M.; Toney, M. F.; Trollsås, M.; Yoon, D. Y. *Chem. Mater.* **1999**, *11*, 3080.

(5) Cha, B. J.; Kim, S.; Char, K.; Lee, J.-K.; Yoon, D. Y.; Rhee, H.-W. *Chem. Mater.* **2006**, *18*, 378.

(6) Freer, E. M.; Krupp, L. E.; Hinsberg, W. D.; Rice, P. M.; Hedrick, J. L.; Cha, J. N.; Miller, R. D.; Kim, H.-C. *Nano Lett.* **2005**, *5*, 2014.

(7) Cho, E.-B.; Kwon, K.-W.; Char, K. *Chem. Mater.* **2001**, *13*, 3837.

(8) Sugita, H.; Saito, A.; Konno, K.; Hayasui, A.; Nishiyama, S.; Ebisawa, M.; Nishikawa, M.; Ohta, Y.; Tominaga, T. *J. Appl. Polym. Sci.* **2003**, *88*, 636.

(9) Ray, G. W.; Peng, S.; Burriesci, D.; O'Toole, M. M.; Liu, E.-D. *J. Electrochem. Soc.* **1982**, *129*, 2152.

(10) Bass, J. D.; Schaper, C. D.; Rettner, C. T.; Arellano, N.; Alharbi, F. H.; Miller, R. D.; Kim, H.-C. *ACS NANO* **2011**, *5*, 4065.

(11) Pénard, A.-L.; Gacoin, T.; Boilot, J.-P. *Acc. Chem. Res.* **2007**, *40*, 895.

(12) Burnside, S. D.; Giannelis, E. P. *Chem. Mater.* **1995**, *7*, 1597.

(13) Sung, P.-H.; Hsu, T.-F. *Chem. Mater.* **1998**, *10*, 1642.

(14) Kim, S.; Cho, J.; Char, K. *Langmuir* **2007**, *23*, 6737.

(15) Moudgil, S.; Ying, J. Y. *Adv. Mater.* **2007**, *19*, 3130.

(16) Caruso, F.; Caruso, R. A.; Möhwald, H. *Science* **1998**, *282*, 1111.

(17) Lim, Y. T.; Kim, J. K.; Noh, Y.-W.; Cho, M. Y.; Chung, B. H. *Small* **2009**, *5*, 324.

(18) Jovanovic, A. V.; Flint, J. A.; Varshney, M.; Morey, T. E.; Dennis, D. M.; Duran, R. S. *Biomacromolecules* **2006**, *7*, 945.

(19) Kamata, K.; Lu, Y.; Xia, Y. *J. Am. Chem. Soc*. **2003**, *125*, 2384.

(20) Chen, J.-F.; Ding, H.-M.; Wang, J.-X.; Shao, L. *Biomaterials* **2004**, *25*, 723.

(21) Du, L.; Liao, S.; Khatib, H. A.; Stoddart, J. F.; Zink, J. I. *J. Am. Chem. Soc*. **2009**, *131*, 15136.

(22) Slowing, I. I.; Trewyn, B. G.; Giri, S.; Lin, V. S.-Y. *Adv. Funct. Mater*. **2007**, *17*, 1225.

(23) Zhou, J.; Wu, W.; Caruntu, D.; Yu, M. H.; Martin, A.; Chen, J. F.; O'Connor, C. J.; Zhou, W. L. *J. Phys. Chem. C* **2007**, *111*, 17473.

(24) Joo, S. H.; Park, J. Y.; Tsung, C.-K.; Yamada, Y.; Yang, P.; Somorjai, G. A. *Nat. Mater*. **2009**, *8*, 126.

(25) Arnal, P. M.; Comotti, M.; Schüth, F. *Angew. Chem. Int. Ed*. **2006**, *45*, 8224.

(26) Chen, G.; Xia, D.; Nie, Z.; Wang, Z.; Wang, L.; Zhang, L.; Zhang, J. *Chem. Mater*. **2007**, *19*, 1840.

(27) Moon G. D.; Jeong, U. *Chem. Mater*. **2008**, *20*, 3003.

(28) Yung, K. C.; Zhu, B. L.; Yue, T. M.; and Xie, C. S. *Compos. Sci. Technol*.

2009, *69*, 260.

(29) Yuan, J.; Zhou, G.; Pu, H. *J. Membrane Sci*. **2008**, *325*, 742.

(30) Zou, H.; Wu, S.; Shen, J. *Chem. Rev*. **2008**, *108*, 3893.

(31) Stöber, W.; Fink, A. *J. Colloid Interf. Sci.* **1968**, *26*, 62.

(32) Zou, H.; Wu, S.; Ran, Q.; Shen, J. *J. Phys. Chem. C* **2008**, *112*, 11623.

(33) Yang, J.; Lind, J. U.; Trogler, W. C. *Chem. Mater.* **2008**, *20*, 2875.

(34) Graf, C.; Vossen, D. L. J.; Imhof, A.; van Blaaderen, A. *Langmuir* **2003**, *19*, 6693.

(35) Darbandi, M.; Thomann, R.; Nann, T. *Chem. Mater*. **2007**, *19*, 1700.

(36) Wan, Y.; Yu, S.-H. *J. Phys. Chem. C* **2008**, *112*, 3641.

(37) Darbandi, M.; Thomann, R.; Nann, T. *Chem. Mater*. **2005**, *17*, 5720.

(38) Khanal, A.; Inoue, Y.; Yada, M.; Nakashima, K. *J. Am. Chem. Soc*. **2007**, *129*, 1534.

(39) Li, W.; Sha, X.; Dong, W.; Wang, Z. *Chem. Commun.* **2002**, 2434.

(40) Chen, D.; Li, L.; Tang, F.; Qi, S. *Adv. Mater.* **2009**, *21*, 3804.

(41) Zhang, T.; Zhang, Q.; Ge, J.; Goeble, J.; Sun, M.; Yan, Y.; Liu, Y.-S.; Chang, C.; Guo, J.; Yin, Y. *J. Phys. Chem. C* **2009**, *113*, 3168.

(42) Zhang, W.-M.; Hu, J.-S.; Guo, Y.-G.; Zheng, S.-F.; Zhong, L.-S.; Song, W.-G.; Wan, L.-J. *Adv. Mater.* **2008**, *20*, 1160.

(43) Song, X.; Gao, L. *J. Phys. Chem. C* **2007**, *111*, 8180.

(44) Song, X.; Gao, L. *Langmuir* **2007**, *23*, 11850.

(45) Qian, H. S.; Guo, H. C.; Ho, P. C.-L.; Mahendran, R.; Zhang, Y. *Small* **2009**, *5*, 2285.

Chapter 2. Quantum Dot/Organosilicate Hybrid Films with Uniform QD Distribution Based on Thiol-Containing Polymeric Organosilicate Ligands

2. 1. Introduction

Colloidal quantum dots (QDs) have received intense attention in recent years as the most practicible next generation phosphors for optical and optoelectronic devices due to their excellent optical properties, such as broad absorption above the bandgap, narrow emission spectral bandwidth, emission wavelength tunability ranging from near UV to visible to near-IR, and high photoluminescence quantum yield (PL QY) in solid states at room temperature.[1-3] Particularly, in the area of light-emitting devices, numerous research groups and companies have reported the practical realization of light-emitting devices utilizing QDs as active materials[4-7] or down-conversion phosphors.[8-10]

In order to use QDs for practical applications such as LEDs and photovoltaics,[11-13] it is necessary to preserve their luminescence efficiency and to extend their lifetime against stringent environmental conditions. For that reason, QDs have often been embedded in matrices such as polymers and epoxy, acrylic, or silicon resins to protect the QDs against external

environment and also, at the same time, effectively improve the processibility of QDs.[14-16] However, the embedding of QDs in unsuitable matrices often causes the opposite effect because QDs are typically immiscible with organic matrices and form massive aggregates due to dissimilar chemical properties between the surfactants covering QDs and matrix materials.

To overcome this problem of the massive aggregation of inorganic nanocrystals, the surface modification of inorganic nanocrystals has been developed based on two different approaches: the simple ligand exchange with oligomeric or polymeric ligands containing functional anchor moieties (such as thiols, amines, carboxylic acids, and phosphine oxides) (the grafting-to approach)[17,18] and the direct growth of brushes[19,20] or shells[21-23] from the surfaces of QDs (the grafting-from approach). Through the surface modification of inorganic nanocrystals such as QDs, surface properties of QDs could be easily modified such that QDs are well miscible with matrix materials to guarantee the uniform distribution of QDs within matrix materials and additional functionality and processibility could also be conferred on the QDs.

In this context, we have already reported that the hybridization of QD with polymeric ligands based on the ligand exchange improved the QD distribution within polymeric matrices.[24,25] The surfactants covering pristine QDs (i.e., oleic acids) was effectively replaced with conducting polymers containing thiol anchoring blocks and the surface-modified QDs were then incorporated in conducting polymer matrices. As a result, the surface-modified QDs showed the uniform distribution within conducting polymer matrices when

compared with pristine QDs, forming massive aggregates within the matrices and the electroluminescence performance of devices based on the QD/conducting polymer hybrids was remarkably improved.

In general, inorganic matrices are known to have distinctive thermal and optical resistance when compared with organic or polymeric counterparts. Thus, we expect that inorganic matrices could be good candidates for QD encapsulants in practical applications such as in optical and optoelectronic devices. Silicone-based resins, for example, have been regarded as promising encapsulants for QDs, replacing conventional epoxy encapsulants with weak environmental stability in optical and optoelectronic devices. Particularly, organosilicates (OS) are well known for their outstanding optical transparency in the visible light range and excellent thermal, chemical, and optical endurance without long-term yellowing problem which occurs with epoxy-based matrices.[26,27] Furthermore, material properties and functionalities of organosilicate polymers are tunable by control of precursors and composition ratios, and uniform OS films in large area as well as patterned OS arrays can be readily prepared by simple processes such as spin-casting and unconventional lithography.

Despite the various advantages of organosilicates as matrix materials, QD hybrids based on such organosilicates are quite rare at the moment and no systematic studies on the control of QD morphology within organosilicate matrices have been undertaken.[28] In the recent studies on QDs for down-conversion phosphor applications, the most of the QDs were just applied as an aggregated form or a blended, physically mixed, form with matrix materials

such as silicones and organosilicates. And the QD morphologies within matrices in those studies were not clearly defined.

Herein, we propose a simple method to prepare robust, processible, and bright quantum dot/organosilicate (QD/OS) hybrid films with improved QD distribution within OS matrices using thiol-containing polymeric OS ligands (see Figure 2. 1(a)). The OS ligands used in the present study were easily prepared by the typical sol-gel copolymerization of 3 different OS precursors in the presence of acid catalysts (see Figure 2. 1(b)). The surfaces of QDs, initially covered with oleic acids, were modified with thiol-containing OS ligands by the simple ligand exchange. Since this simple surface modification of QDs neither includes any harmful chemicals causing damage to QDs nor requires any harsh process conditions, the QD/OS hybrid films with the uniform distribution of QDs within the OS matrices were obtained without losing any quantum efficiency and any emission spectral shift. We also demonstrated that the QD/OS hybrid films are readily processible (with unconventional imprint lithography) and show excellent optical transparency as well as enhanced environmental stability in hydrochloric acid.

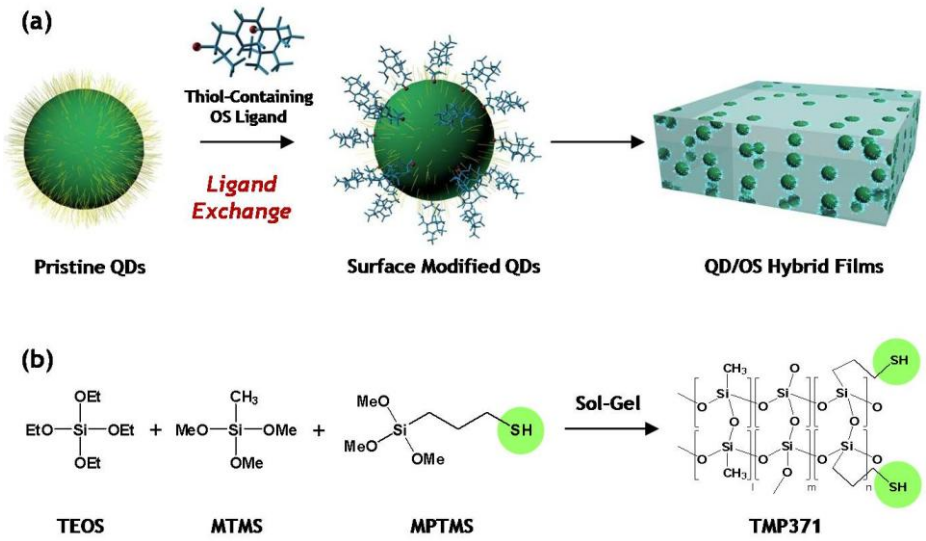

Figure 2. 1. (a) A schematic on the preparation of QD/OS hybrid films and (b) a schematic illustration for the synthesis of thiol-containing polymeric OS ligands (TMP371).

2. 2. Experimental Details

2. 2. 1. Chemicals

Cadmium oxide (CdO, 99.99 %), zinc acetate (99.9 %, powder), selenium (99.9 %, powder), sulfur (99.9 %, powder), trioctylphosphine (TOP, 90 %), oleic acid (OA, 90 %), 1-octadecene (ODE, 90 %), and mercaptopropionic acid (MPA, 99.8 %), tetraethyl orthosilicate (TEOS, 98 %), methyltrimethoxysilane (MTMS, 98 %), (3-mercaptopropyl)trimethoxysilane (MPTMS, 95 %), trimethylethoxysilane (TMES, 98 %), hydrochloric acid (aq, 37 %), and methylisobutylketone (MIBK, 99 %) were used as purchased from Aldrich.

2. 2. 2. Synthesis of Oleic Acid Coated CdSe@ZnS QDs

The OA-coated red, green, and blue CdSe@ZnS QDs were prepared following the one-pot synthetic method, which has already been reported by our laboratory.[29-31] Synthesized QDs are purified repeatedly (three times) by precipitation/redispersion methods to remove residual ligands or unreacted precursors. All QDs are dispersed in toluene (10 mg/ml) and kept under ambient condition before use.

2. 2. 3. Synthesis of (Thiol-Containing) OS Polymeric Ligands

The OS polymers employed as the ligands for the surface modification of QDs as well as OS matrices for hybrid film formation were prepared by the sol-gel copolymerization of OS monomers (TEOS, MTMS, and MPTMS)

using hydrochloric acid as a catalyst.[32] The hydrochloric acid was completely removed by washing several times using distilled water. For OS ligands of TM37 and TMP371, the feed ratios of TEOS, MTMS, and MPTMS were 3 : 7 : 0 and 3 : 7 : 1 by molar ratio, respectively. The detail synthetic condition is described Table 2. 1.

Table 2. 1. Synthetic condition of TM37 and TMP 371

	TM37	**TMP371**
THF (ml)	140	140
TEOS (g)	20.63	18.75
MTMS (g)	31.47	28.61
MPTMS (g)	0	5.89
H_2O (ml)	58.95	58.95
HCl (37 %, g)	0.69	0.69
Rxn. Time (h)	6	6
Rxn. Temp. (℃)	60	60

2. 2. 4. Preparation of QD/OS Hybrid Films

Pristine QDs in toluene were first precipitated using centrifuge and redispersed in OS solutions (OS polymers dissolved in MIBK, 100 mg/ml) for the QD surface modification. The QD solutions in MIBK were sonicated until they became clear. The surface-modified QD solutions were washed with n-hexane and redispersed in MIBK. Additional OS solutions were added to adjust the QD loading amount in OS polymer matrices. The QD loading content was varied from 0.5 to 10 wt% of total OS polymers. To prepare free-standing QD/OS thin films for QD morphology characterization, QD/OS mixture solutions with 10 wt% of OS concentration in MIBK were spun-cast on poly(allylamine hydrochloride) (PAH)-coated Si wafers. The QD/OS hybrid films were further annealed at 70 ℃ for 1 h. After thermal annealing, free standing QD/OS hybrid films were obtained by the removal of the PAH layers in distilled water (film thickness: ~ 150 nm). To characterize the PL QY, the environmental stability, and the transmittance, the QD/OS hybrid films with 5 wt% of QDs were prepared by drop-casting (film thickness: ~ 6 μm). The QD/OS hybrid films prepared were then subject to further curing at 70 ℃ for 1 h.

2. 2. 5. Characterizations

The molecular structure and composition of OS polymeric ligands prepared in the present study were characterized by FT-IR (FT-IR200, JASCO), NMR (500MHz, Avance500, Bruker), solid-state NMR (500MHz, Avance II, Bruker), and Matrix-Assisted Laser Desorption/Ionization Time-of-Flight

(MALDI-TOF) mass spectroscopy (Voyager-DETM STR Biospectrometry Workstation, Applied Biosystems Inc.). The QD morphologies within OS matrices were obtained by energy-filtered transmission electron microscope (EF-TEM; LIBRA 120, Carl Zeiss) and the cross-sectional TEM samples were obtained with an ultra microtome (AT/ULTRACUT R, LEICA Microsystems). The PL spectra and quantum yields of QD solutions as well as QD/OS films were obtained with absolute photoluminescence (PL) quantum yield measurement system combined with an integrating sphere detector (C9920-02, Hamamatsu). The transmittance of QD/OS films was measured with a UV-Vis spectrometer (Lambda 35 UV/VIS Spectrometer, PERKIN ELMER Instruments). The patterned QD/OS films were characterized by a Field-Emission Scanning Electron Microscope (FE-SEM; JSM 6071F, JEOL) and an Image Restoration Microscope (Delta Vision RT, Applied Precision).

2. 3. Results and Discussion

2. 3. 1. Synthesis and Characterization of OS Ligands

Two different types of OS ligands, TM37 and TMP371, were prepared for the surface modification of CdSe@ZnS QDs covered with oleic acids (pristine QDs). To prepare the OS ligands for the QD surface modification, TEOS and MTMS were used as main silicate precusors and a small amount of MPTMS employed as a precursor containing thiol groups, which we believe have energetically favorable interactions with the QD surfaces. TEOS (tetravalent precursor) should make up the network-type OS polymers with relevant molecular weights and MTMS (trivalent monomer) should enable stress relaxation and uniform film formation without forming cracks of TEOS-based OS films.[26] The MPTMS precursors containing propyl thiol end groups should yield OS ligands for effective QD surface modification. The molecular structure and composition of the two different OS ligands prepared in this study were analyzed by FT-IR, 1H-NMR, 29Si-NMR, and MALDI-TOF.

In the FT-IR spectra, TM37 and TMP371 showed almost same FT-IR spectra. In FT-IR spectra, O-H stretching peaks at ~ 3400 cm^{-1}, Si-OH stretching peaks at ~ 890 cm^{-1}, and cross-linked Si-O-Si stretching peaks at ~ 1045 cm^{-1} are appeared without caged Si-O-Si stretching peak which appears at ~ 1130 cm^{-1} (see Figure 2. 2(a)).

^{1}H-NMR spectra of TM37 and TMP 371 showed strong Si-CH_3 peaks at ~ 0.15 ppm, weak and broad Si-OH peaks at ~ 5.72 ppm, and residual methoxy (Si-O-CH_3) and ethoxy (Si-O-CH_2CH_3) peaks at 3.3-3.9 & 1.1-1.4 ppm in

common. In the case of TMP371, additional peaks from propyl thiol moieties in MPTMS were detected at ~ 0.80 ppm (Si-CH_2CH$_2$CH$_2$SH), ~ 1.64 ppm (Si-CH$_2$CH_2CH$_2$SH), and ~ 2.58 ppm (Si-CH$_2$CH$_2$CH_2SH) (see Figure 2. 2(b)). Through the integration of the peaks, the incorporation ratio of MTMS and MPTMS in TMP371 was calculated as follows.

- Incorporation ratio of MTMS : MPTMS = 7.67 : 1

The incorporation ratios of OS precursors in TM37 and TMP371 were thoroughly calculated by Solid ^{29}Si-NMR analysis. The solid ^{29}Si-NMR spectra of the both OS polymers and peak information were presented in Figure 2. 3 and Table 2. 2. Through the integration of the peaks, the incorporation ratios of OS precursors in TM37 and TMP371 were calculated as follows.

- For TM37, incorporation ratio of TEOS : MTMS = 2.17 : 7
- For TMP371, incorporation ratio of TEOS : (MTMS+MPTMS) = 2.53 : 8

Using the results of ^{1}H-NMR and solid ^{29}Si-NMR, the incorporation ratio of three OS precursors in TMP 371 was calculated as follows.

- Incorporation ratio of TEOS : MTMS : MPTMS = 2.74 : 7.67 : 1

The molecular weight and polydispersity index of TM37 and TMP371 were measured by MALDI-TOF. (see Figure 2. 4 and Table 2. 3)

As a result, the TM37 OS ligands which were prepared with TEOS and MTMS precursors are the network-type organosilicate polymers containing residual amount of silanol end groups while the TMP371 OS ligands, prepared with TEOS, MTMS, and a small amount of MPTMS, showed almost the same molecular structure and composition with the TM37 except a small

amount of additional propyl thiol end groups.

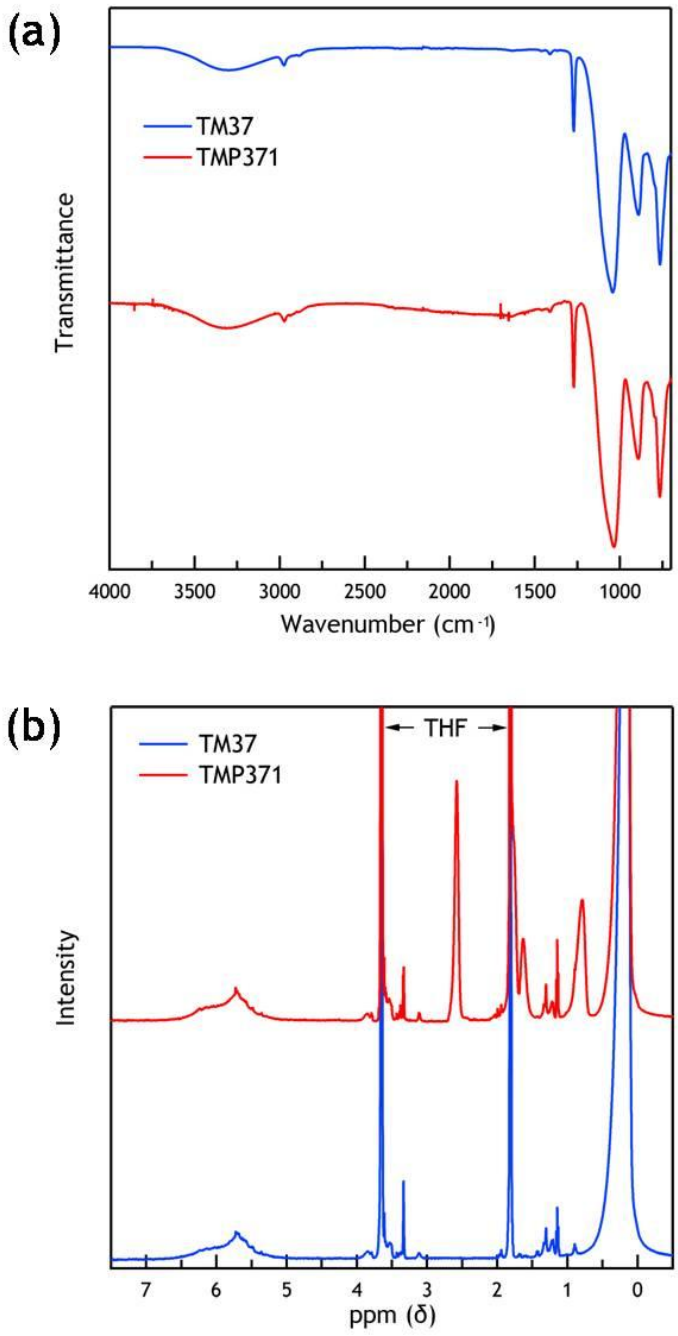

Figure 2. 2. (a) FT-IR spectra and (b) ^{1}H-NMR spectra of TM37 and TMP371.

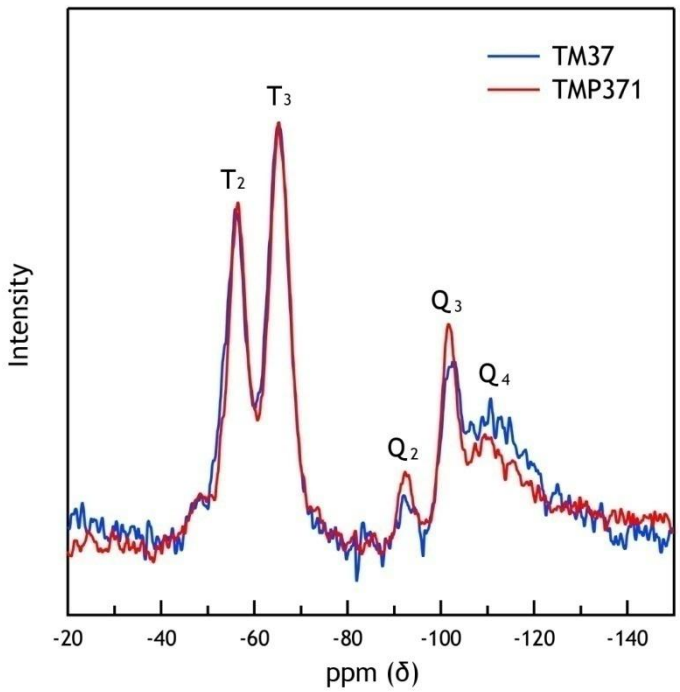

Figure 2. 3. Solid ^{29}Si-NMR spectra of TM37 and TMP371.

Table 2. 2. Peak information of solid ^{29}Si-NMR spectra

Peak	T_2	T_3	Q_2	Q_3	Q_4
Molecular Structure	C*Si*$(OSi)_2$ OH	C*Si*$(OSi)_3$	*Si*$(OSi)_2$ $(OH)_2$	*Si*$(OSi)_3$ (OH)	*Si*$(OSi)_4$
Monomers	MTMS, MPTMS	MTMS, MPTMS	TEOS	TEOS	TEOS

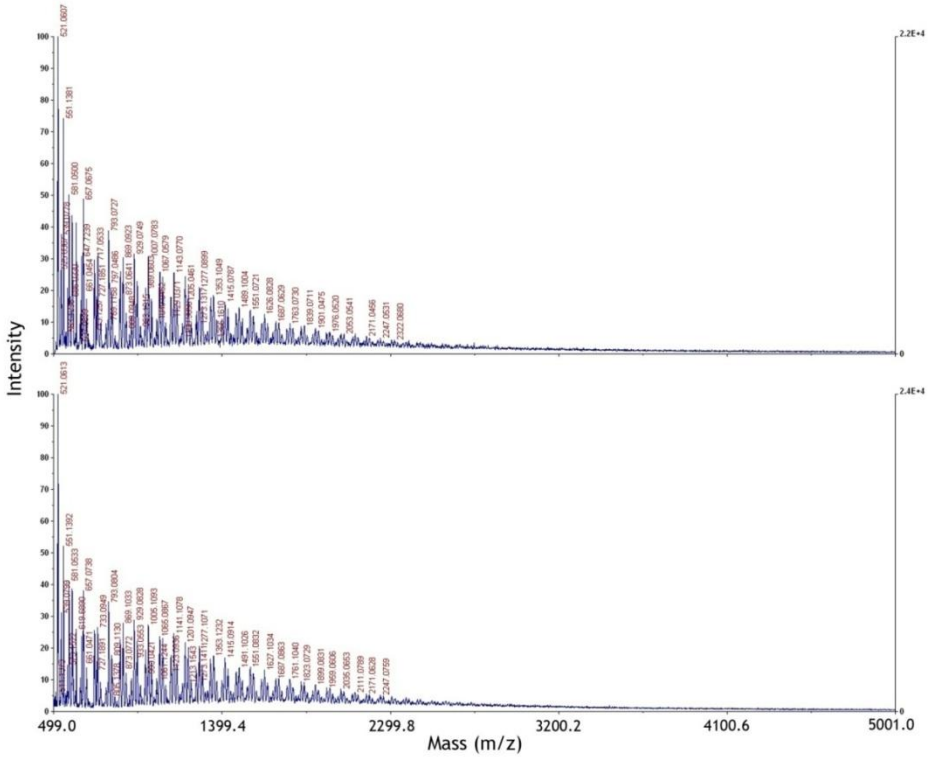

Figure 2. 4. MALDI-TOF spectra of TM37 (top) and TMP371 (bottom).

Table 2. 3. The molecular weight and polydispersity index (PDI) of TM37 and TMP371

	M_n	M_z	M_w	PDI
TM37	1339.02	1618.57	1486.95	1.11
TMP371	1290.32	1611.77	1467.02	1.14

2. 3. 2. Surface Modification of QDs Using OS Ligands

To prepare QD-OS hybrid nanoparticles, the OA surfactants covering the pristine QDs were replaced with the OS ligands based on the simple ligand exchange. The QDs surface modified with either TM37 or TMP371 were denoted as QD-TM and QD-TMP, respectively. The surface modification of QDs with OS ligands was monitored with the change in the solubility of QDs.[24] While pristine QDs covered with oleic acids are dispersed only in non-polar solvents (e.g., hexane, cyclohexane, toluene), after the surface modification with both types of OS ligands they can be rendered only in polar organic solvents, such as acetone, ethanol, DMF, and MIBK, which apparently shows that OSs replace oleic acids and bind with QDs. Figure 2. 5(a) shows the phase transfer of QDs in a layered solvent pair of n-hexane and DMF. Pristine QDs were selectively dispersed in the n-hexane phase (upper layer), however, after the surface modification, the QD-OSs preferentially migrated into the DMF phase (lower layer).

The emission PL spectra and quantum yield of QDs were characterized by absolute PL quantum yield measurement system (see Figure 2. 5(b)). During the surface modification, QDs maintain their optical properties (e.g., peak PL emission wavelength (λ_{peak}) and full-width at half maximum (FWHM)), representing that the OS ligands replace oleic acids and adsorb to the surface of QDs without severe damages on the QDs. Interestingly, slight changes in PL QY of QD-OS hybrids were observed depending on the types of OS ligands. QD-OS hybrids with TMP, which containing thiol (SH) binding

moieties, exhibit slight increase in PL QY of 71.2 % compared with pristine QDs (68 %), while QD-TM hybrids show slight decrease in PL QY to 64.6 %.

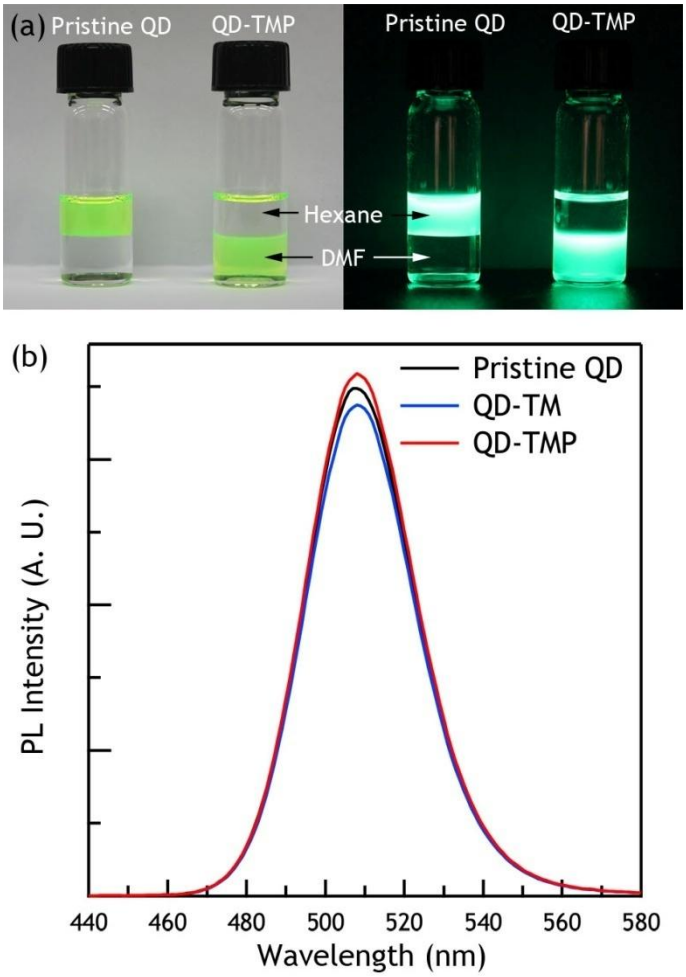

Figure 2. 5. Photographs illustrating the solubility change of QDs by the hybridzation with OS ligands (TMP371) under room light (left) and UV exposure (right, λ_{ex}= 365 nm). Left vial: pristine QDs dispersed in hexane. Right vial: QDs surface modified with thiol-containing OS ligands dispersed in DMF. (b) PL spectra of pristine QD, QD-TM, and QD-TMP solutions in THF. The excitation wavelength for the PL measurement was fixed at 440 nm.

2. 3. 3. Preparation of QD/OS Hybrid Films and the Comparative Studies on the Influence of QD Morphology within OS Matrices

To characterize the QD morphology within OS matrices, QD/OS films with two different types of OS polymers were prepared. In contrast to the similar colloidal solubility change by both types of OS ligands, huge difference in their morphology in films has been observed: QDs are homogeneously dispersed within TMP371 matrices confirmed by plan- and cross-sectional TEM images regardless to the chosen variation in QD contents, while QDs are likely to aggregate within TM37 matrices (see Figure 2. 6). This clear difference in their final morphology suggests that the silanol anchor groups of TM37 do not bind to QD surface sufficiently to disperse them within the OS matrices, while the thiol anchor groups of TMP provide enthalpic attraction between QDs and OS ligands to homogeneously disperse them within the OS matrices.[24] Consequently, QDs surface-modified with TM37 (QD-TM) were partially miscible with the TM37 matrices and the phase separation between QDs and OS matrices occurred during the film formation. Since TMP371 surface modifiers with strong binding thiol anchors could effectively replace the OA surfactants covering pristine QDs, thus improving the miscibility with TMP371 matrices, the QDs surface-modified with TMP371 (QD-TMP) were uniformly distributed within the entire matrices of TMP371 films.

For the comparative study on the influence of QD morphology within OS matrices on PL QY of the QD/OS films, The quantum yields of QDs dispersed within two different OS matrices were characterized at different QD loading amount, as shown in Figure 2. 7(a). As the QD content is increased, the

quantum yield of the QD/TM blend films gradually decreases from 60 % to 55 %. This trend in the QY change is related to the fact that the QDs in TM37 are rarely aggregated at low QD concentration but as the QD loading amount is increased, the QDs are massively aggregated, lowering the quantum yield presumably due to the concentration quenching. On the other hand, the QD/TMP hybrid films based on the TMP371 matrices show almost the consistent quantum yield around 65 - 68 % regardless of the QD loading amount due to the uniform QD distribution within the OS matrices.

To investigate the influence of QD morphology within OS matrices on the environmental stability of QD/OS films, the QD/OS films containing 5 wt% of QDs were exposed to acidic atmosphere. The QD/OS films were placed in hydrochloric acid solution (aq, 18.5 %) and the emission PL intensity of the QD/OS films was monitored as a function of dipping time (see Figure 2. 7(b)). The emission PL intensity of the QD/TM blend films rapidly decreases and all the QDs were almost completely quenched within 30 min of dipping in hydrochloric acid solution while the emission PL intensity of the QD/TMP hybrid films is maintained at 68 % of the initial PL intensity up to 30 min of dipping. The reason for the improved stability in hydrochloric acid of the QD/TMP hybrid films is again due to the uniform QD morphology within the TMP OS matrices. In the case of the QD/TM blend films, all the QDs are located at the top surface of the OS thin films and QDs at the top of the surface are quickly quenched upon exposure to hydrochloric acid. On the other hand, QDs in the QD/TMP hybrid films are slowly quenched upon exposure to hydrochloric acid since the QDs within the TMP matrices are

uniformly distributed within the matrix and the penetration of hydrochloric acid within the TMP matrix is purely diffusional. As a result, QDs in the QD/TMP hybrid films are environmentally much more stable, which is directly related to the degree of QD distribution within OS matrices.[23]

To determine the effect of QD morphology within OS matrices on transparency of the QD/OS films, the transmittance of OS matrices and QD/OS films was measured with a UV-Vis spectrometer (see Figure 2. 8). Both OS films, TM37 and TMP371, show extremely high transmittance more than 99 % in the visible wavelength range. The QD/TMP hybrid films also shows high transparency similar to the pure OS films due to the uniform QD distribution except short wavelength range (< 500 nm) due to the absorption by QDs. In the case of the QD/TM blend films, the films appear to be a little bit opaque and the transmittance measured is also lower than the transmittance of the QD/TMP hybrid films in the whole visible range. Because all the QDs were located at the top surface of the QD/TM blend films, forming an aggregate layer of bigger size, the incident visible light is scattered off the film surface by the QD aggregate layer at the surface, ultimately lowering the transmittance.

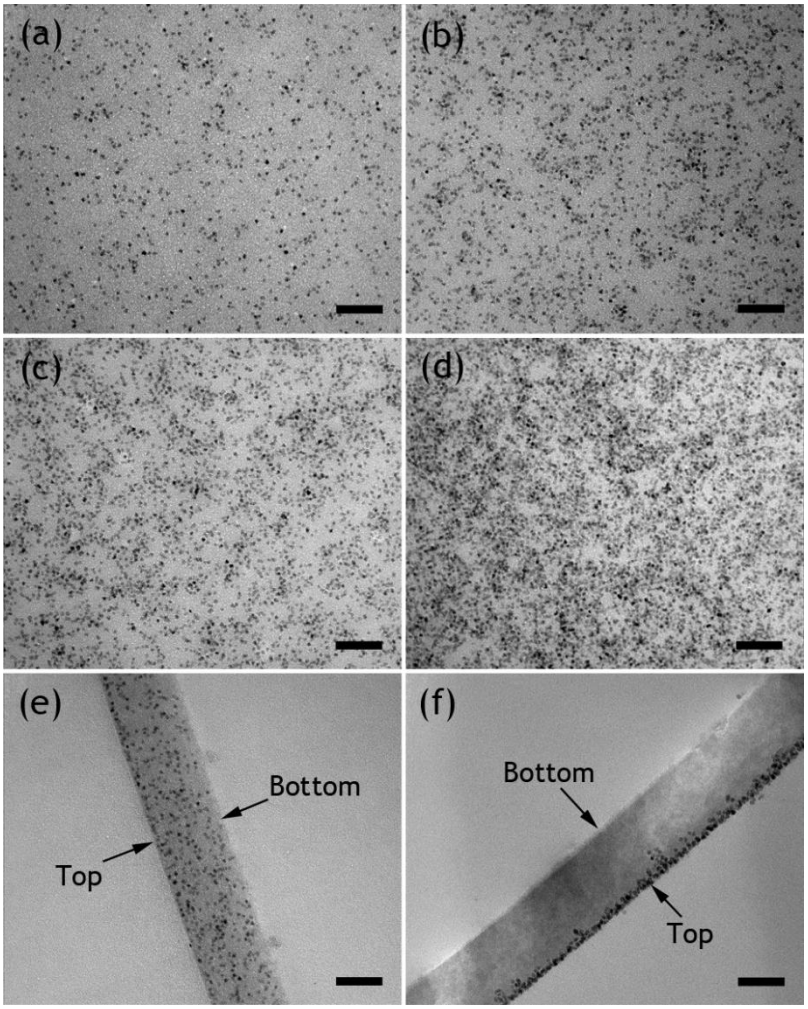

Figure 2. 6. The plan-view TEM images of QD/TMP hybrid films containing different amounts of QD within the films ((a) 1 wt%, (b) 3 wt%, (c) 5 wt%, and (d) 10 wt% of QDs). The cross-sectional views of (e) a QD/TMP hybrid film and (f) a QD/TM blend film containing 5 wt% of QDs. All the films were prepared by spin-casting QD/OS solutions with 10 wt% of OS concentration in MIBK (scale bars: 100 nm).

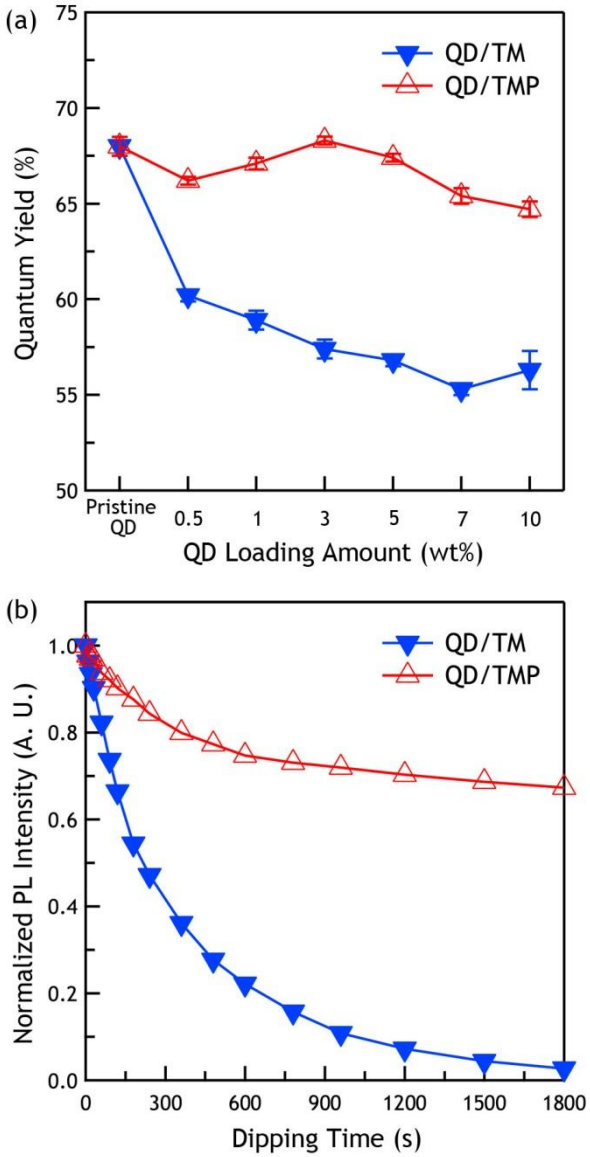

Figure 2. 7. (a) PL quantum yield (QY) of pristine QD solution in THF and QD/OS films (QD/TM and QD/TMP) with different QD loading amount. (b) The change in PL intensity of QD/TM blend and QD/TMP hybrid films exposed to hydrochloric acid solution (aq, 18.5 %) as a function of dipping time. The excitation wavelength for both characterizations was fixed at 440 nm.

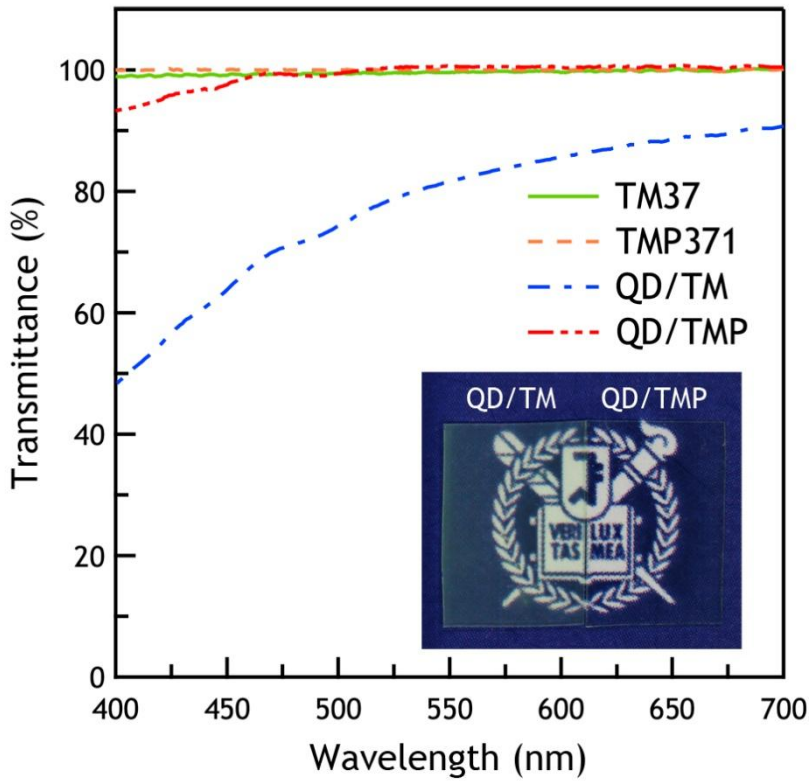

Figure 2. 8. Transmittance of OS (TM37, TMP371) and QD/OS (QD/TM, QD/TMP) films in visible range. The insert photograph showing QD/TM blend film (left) and QD/TMP hybrid film (right) under room light (QD content: 5 wt%, film thickness: 6 μm).

2. 3. 4. Preparation of Red, Green, Blue and White QD/OS Hybrid Films and LED Application

Red, green, blue, and white QD/TMP hybrid films were prepared with three different QDs (with red, green, and blue emissions) and TMP371 matrices (see Figure 2. 9(a)). The QD/TMP hybrid film with white emission was prepared by mixing red, green, and blue QDs in 1 : 4.5 : 2.2 of weight ratio.[33] All the QD/TMP hybrid films showed high transparency under room light and emitted vivid light under UV exposure (λ= 365 nm) exciting QDs. The QD/TMP hybrid films with red, green, and blue emissions showed high color purity and their chromaticity coordinates reside outside the current National Television System Committee (NTSC) standard color triangle in the Commission Internationale de l'Eclairage (CIE) chromaticity diagram. The white QD/TMP hybrid film also retains the reasonable chromaticity coordinate located within the white light region of the CIE chromaticity diagram (see Figure 2. 9(b)).

A white LED based on the QD/OS hybrid films is also demonstrated using a commercial blue InGaN LED chip (λ_{peak}= 447 nm, Haewon Semiconductor, Korea) and a red/green mixed QD/TMP hybrid film used as a down-conversion phosphor. The QD/TMP hybrid film with 5 wt% QDs was deposited on the LED chip surface by drop casting and then cured at 70 ℃ for 1 h. A white emission from LED was observed at 2.5 V and 20 mA of the LED device and its electroluminescence spectrum showing the combination of the emissions from QDs and the blue LED chip is obtained (see Figure 2. 10). The chromaticity coordinates of the white LED were (0.34, 0.35) in the

CIE chromaticity diagram and the color temperature is 5,300 K.

Patterned QD/TMP hybrid films could also be prepared using PDMS stamps by unconventional imprint lithographic method (see Figure 2. 11).[34,35] A PDMS stamp with inverted cylindrical patterns was prepared with a Si master template, which was originally fabricated by the conventional lithographic process. The diameter, center-to-center distance, and depth of the inverted cylindrical patterns in a PDMS stamp are 9, 21, and 10 μm, respectively. The 20 wt% QD/TMP solution containing 5 wt% of QDs in MIBK was first deposited on a PET substrate by drop casting and remained for 20 min to evaporate the solvent. A PDMS stamp was then placed on top of the semi-dried QD/TMP solution and mildly pressed to transfer the cylinder patterns to the QD/TMP hybrid films. After thermal treatment at 70 ℃ for 1 h, the PDMS stamp was removed, leaving behind the solidified QD/TMP patterns. The pattern size and shape of the QD/TMP replicas were exactly copied from the original PDMS stamp and the cylinder height is about 7 μm. From the fluorescence measurement, the cylinder patterns with green emissions from the QDs embedded within TMP matrices are clearly evident.

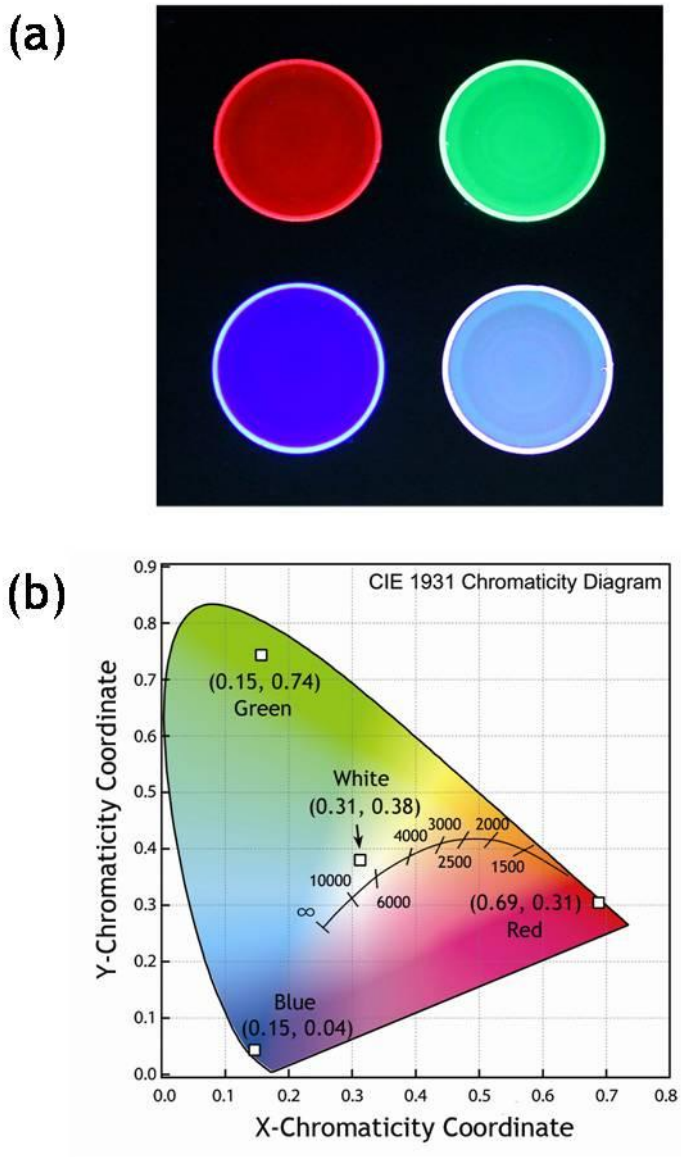

Figure 2. 9. (a) Red, green, blue, and white QD/TMP hybrid films under UV exposure (λ= 365 nm) and (b) their chromaticity coordinates.

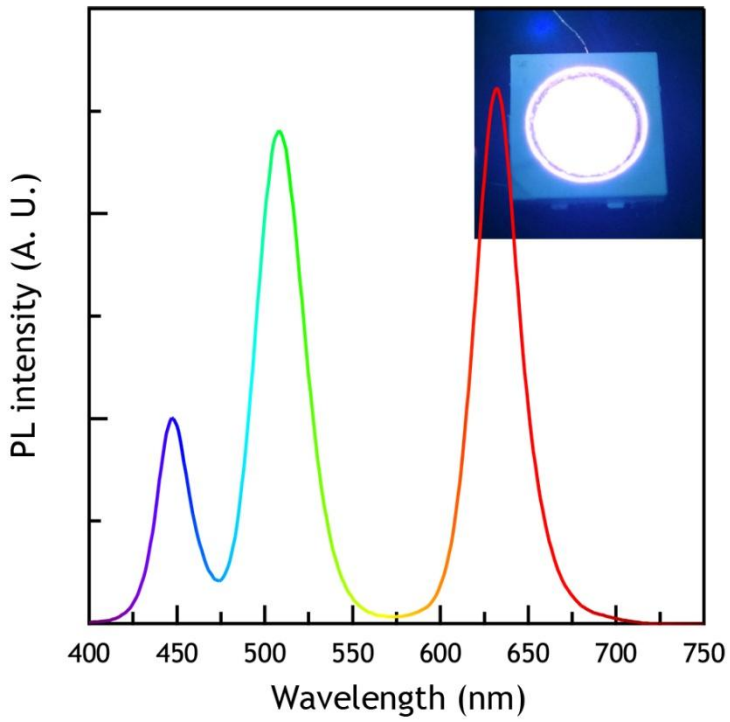

Figure 2. 10. The PL spectrum of a white LED prepared with a red/green mixed QD/TMP film placed on top of a blue LED chip. The insert photograph showing the white LED.

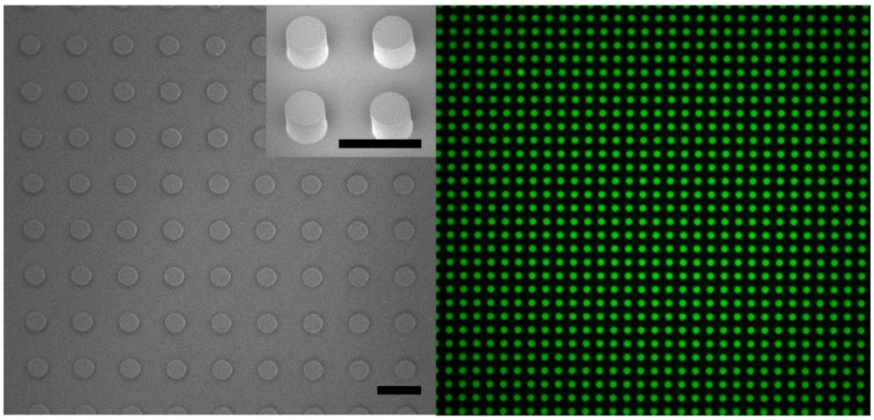

Figure 2. 11. FE-SEM (left) and fluorescence microscopy (right) images of cylinder-patterned QD/TMP hybrid films. The insert picture shows the tilted FE-SEM image (scale bars: 20 μm). The excitation wavelength for fluorescence microscopy was fixed at 490 nm.

2. 4. Conclusion

QD-OS hybrid nanoparticles were first prepared by the surface modification of QDs using thiol-containing OS ligands through the ligand exchange. The QD-OSs obtained from such surface modification showed the solubility change from nonpolar solvents to polar solvents maintaining excellent optical properties (such as peak emission PL wavelength (λ_{peak}), FWHM, and quantum yield). The QD/OS hybrid thin films based on thiol-containing OS ligands (QD/TMP) showed the uniform QD distribution across the entire OS films due to the improved miscibility between QDs and OS matrices employed. The QD/OS hybrid films also showed the enhanced quantum yield and resistance against hydrochloric acid with excellent optical transparency due to the uniform QD distribution within the TMP OS matrices. Using red, green, blue QDs, and their mixture, the QD/OS hybrid films with red, green, blue, and white emissions were obtained and a white LED was fabricated using a blue LED chip as a light source and a red/green mixed QD/OS hybrid film employed as down-conversion phosphors. In addition, a cylinder-patterned QD/OS hybrid film was demonstrated using the unconventional imprint lithographic method. Based on the several advantages deriving from the hybrid films with uniform QD distribution within OS matrices, we expect that the QD/OS hybrid films would be good candidate materials for optical and optoelectronic device applications.

2. 5. References

(1) Brus, L. *J. Phys. Chem*. **1986**, *90*, 2555.

(2) Murray, C. B.; Kagan, C. R.; Bawendi, M. G. *Annu. ReV. Mater. Sci*. **2000**, *30*, 545.

(3) Alivisatos, A. P. *Science* **1996**, *271*, 933.

(4) Colvin, V. L.; Schlamp, M. C.; Alivisatos, A. P. *Nature* **1994**, *370*, 354.

(5) Coe, S.; Woo, W. K.; Bawendi, M.; Bulovic, V. *Nature* **2002**, *420*, 803.

(6) Achermann, M.; Petruska, M. A.; Kos, S.; Smith, D. M.; Koleske, D. D.; Klimov, V. I. *Nature* **2004**, *429*, 642.

(7) Sun, Q.; Wang, Y. A.; Li, L. S.; Wang, D.; Zhu, T.; Xu, J.; Yang, C.; Li, Y. *Nat. Photonics* **2007**, *1*, 717.

(8) Chen, H. S.; Wang, S. J. J. *Appl. Phys. Lett*. **2005**, *86*, 131905.

(9) Lim, J.; Jun, S.; Jang, E.; Baik, H.; Kim, H.; Cho, J. *Adv. Mater*. **2007**, *19*, 1927.

(10) Ziegler, J.; Xu, S.; Kucur, E.; Meister, F.; Batentschuk, M.; Gindele, F.; Nann, T. *Adv. Mater*. **2008**, *20*, 4068.

(11) Huynh, W. U.; Dittmer, J. J.; Alivisatos, A. P. *Science* **2002**, *295*, 2425.

(12) Plass, R.; Pelet, S.; Krueger, J.; Gratzel, M.; Bach, U. *J. Phys. Chem. B* **2002**, *106*, 7578.

(13) Johnston, K. W.; Pattantyus-Abraham, A. G.; Clifford, J. P.; Myrskog, S. H.; Mac Neil, D. D.; Levina, L.; Sargent, E. H. *Appl. Phys. Lett*. **2008**, *92*, 151115.

(14) Lin, C. C.; Liu, R.-S. *J. Phys. Chem. Lett*. **2011**, *2*, 1268.

(15) Kim. K.; Woo, J. Y.; Jeong, S.; Han, C.-S. *Adv. Mater*. **2011**, *23*, 911.

(16) Wang, X.; Li, W.; Sun, K. *J. Mater. Chem.* **2011**, *21*, 8558.

(17) Mattoussi, H.; Mauro, J. M.; Goldman, E. R.; Anderson, G. P.; Sundar, V. C.; Mikulec, F. V.; Bawendi, M. G. *J. Am. Chem. Soc*. **2000**, *122*, 12142.

(18) Uyeda, H. T.; Medintz, I. L.; Jaiswal, J. K.; Simon, S. M.; Mattoussi, H. *J. Am. Chem. Soc*. **2005**, *127*, 3870.

(19) von Werne, T.; Patten, T. E. *J. Am. Chem. Soc*. **1999**, *121*, 7409.

(20) Skaff, H.; Sill, K.; Emrick, T. *J. Am. Chem. Soc*. **2004**, *126*, 11322.

(21) Mulvaney, P.; Liz-Marzán, L. M.; Giersig, M.; Ung, T. *J. Mater. Chem*. **2000**, *10*, 1259.

(22) Gerion, D.; Pinaud, F.; Williams, S. C.; Parak, W. J.; Zanchet, D.; Weiss, S.; Alivisatos, A. P. *J. Phys. Chem. B* **2001**, *105*, 8861.

(23) Murase, N.; Yang, P. *Small* **2009**, *5*, 800.

(24) Zorn, M.; Bae, W. K.; Kwak, J.; Lee, H.; Lee, C.; Zentel, R.; Char, K. *ACS NANO* **2009**, *3*, 1063.

(25) Kwak, J.; Bae, W. K.; Zorn, M.; Woo, H.; Yoon, H.; Lim, J.; Kang, S. W.; Weber, S.; Butt, H.-J.; Zentel, R.; Lee, S.; Char, K.; Lee, C. *Adv. Mater*. **2009**, *21*, 5022.

(26) Baney, R. H.; Itoh, M.; Sakakibara, A.; Suziki, T. *Chem. ReV*. **1995**, *95*, 1409.

(27) Kudo, T.; Gordon, M. S. *J. Am. Chem. Soc*. **1998**, *120*, 11432.

(28) Selvan, S. T.; Bullen, C.; Ashokkumar, M.; Mulvaney, P. *Adv. Mater*. **2001**, *13*, 985.

(29) Bae, W. K.; Char, K.; Hur, H.; Lee, S. *Chem. Mater*. **2008**, *20*, 531.

(30) Bae, W. K.; Nam, M. K.; Char, K.; Lee, S. *Chem. Mater*. **2008**, *20*, 5307.

(31) Lim, J.; Bae, W. K.; Lee, D.; Nam, M. K.; Jung, J.; Lee, C.; Char, K.; Lee, S. *Chem. Mater*. **2011**, *23*, 4459.

(32) Lee, J. K.; Char, K.; Rhee, H. W.; Ro, H. W.; Yoo, D. Y.; Yoon, D. Y. *Polymer* **2001**, *42*, 9085.

(33) Demir, H. V.; Nizamoglu, S.; Erdem, T.; Mutlugun, E.; Gaponik, N.; Eychmüller, A. *Nano Today* **2011**, *6*, 632.

(34) Ro, H. W.; Jones, R. L.; Peng, H.; Hines, D. R.; Lee, H.-J.; Lin, E. K.; Karim, A.; Yoon, D. Y.; Gidley, D. W.; Soles, C. L. *Adv. Mater*. **2007**, *19*, 2919.

(35) Yoon, H.; Oh, S.-G.; Kang, D. S.; Park, J. M.; Choi, S. J.; Suh, K. Y.; Char, K.; Lee, H. H. *Nat. Commun*. **2011**, *2*, 455.

Chapter 3. Transparent Organosilicate Hybrid Films with Thermally Insulating and UV-Blocking Properties Based on Silica/Titania Hybrid Hollow Colloidal Shells

3. 1. Introduction

Hollow silica shells (HSSs) have been attracted a lot of attention due to their unique properties such as hollow inner space, large surface area, low thermal conductivity, low density, biocompatibility.[1-4] Thus, numerous research groups have reported the preparation of multi-functional HSSs and their practical applications as nano-containers for drug delivery,[5-8] supporting materials for catalysts,[9-12] thermal insulators for heat management,[13,14] and light fillers for nanocomposites.[15]

Particularly, in the area of thermal insulators, HSSs have been regarded as a promising candidate for heat-blocking materials due to their hollow inner space with large amount of trapped air. Indeed, commercial products based on HSSs such as insulating paints containing HSSs for preventing heat exchange between in and outside of buildings and insulating walls and doors containing HSSs for high performance refrigerators. However, such HSS-based insulators are not easy to be applied to transparent substances such as exterior glasses, windows, and windscreens because they typically have large size

from several hundreds of nanometers to several tens of micrometers which is opaque in the visible range.

The transparency of nano-objects within the matrices depends on the size, shape, refractive index, and distribution state of nano-objects. In terms of size, it is well known that to be transparent in the visible range, the average size of HSSs should be small-sized about several tens of nanometers.[16] The synthetic strategies for such small-sized HSSs were already reported by several research groups. They applied nano-objects like metal/metal oxide nanoparticles, block copolymer micelles, polymeric colloidal aggregates as templates for small sized HSSs which have tens of nanometer-sized diameter.[17-21] The small-sized HSSs were successfully prepared with various synthetic routes, however, neither attempts to transparent insulators based on small-sized HSSs nor conjunctive studies on transparency and heat-blocking property of small-sized HSSs has been undertaken yet. Furthermore, multi-functional hybrids based on small-sized HSSs with extended functionality are quite rare at the moment.

Herein, we propose transparent organosilicate hybrid films with thermally insulating and UV-blocking properties based on silica/titania hybrid hollow shells (STHs) (see Figure 3. 1). STHs are the attractive candidates to save energy as one of effective insulating materials due to low thermal conductivity originating from hollow inner space as well as the excellent UV-block characteristics of TiO_2 shells.[13,14,16,24] The HSSs were first prepared using poly(acrylic acid) (PAA) colloidal aggregates as templates, tetraethyl orthosilicate (TEOS) as a silica precursor, and ammonia hydroxide as a catalyst based on the modified Stöber method.[19] Nanoparticle-like TiO_2 outer

layers were then coated on the surfaces of HSSs using titanium tetrabutoxide (TBOT) as a titania precursor.[22] The average diameter of STHs was varied from 30 to 100 nm. The organosilicate matrices were also prepared by the sol-gel reaction with TEOS, methyltrimethoxysilane (MTMS), and dimethyldimethoxysilane (DMDMS) as silica sources along with hydrochloric acid as a catalyst. The STHs mixed with organosilicate matrices were deposited on glass substrates to realize thermally insulating and UV-blocking layers. The STH-containing organosilicate films show excellent heat- and UV-blocking capabilities, yet maintaining high transparency.

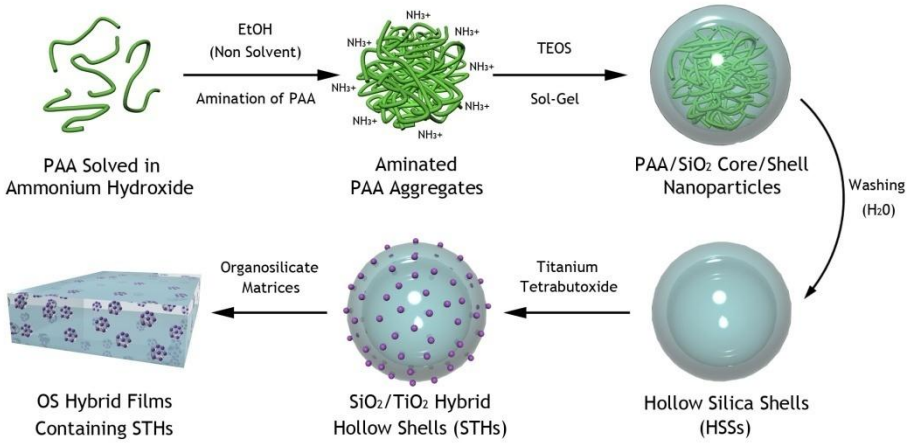

Figure 3. 1. A schematic on the preparation of multi-functional OS hybrid films containing STHs.

3. 2. Experimental Details

3. 2. 1. Chemicals

Poly(acrylic acid) (PAA, Mw= 1.8 k), tetraethyl orthosilicate (TEOS, 98 %), methyltrimethoxysilane (MTMS, 98 %), dimethyldimethoxysilane (DMDMS, 95 %), titanium tetrabutoxide (TBOT, 97 %) acetic acid (99.7 %), and ammonium hydroxide solution (aq, 28-30 %) were used as purchased from Aldrich.

3. 2. 2. Synthesis of SiO_2/TiO_2 Hybrid Hollow Shells

0.25 g of PAA solved in 5 ml of ammonium hydroxide solution was rapidly injected in 100 ml of ethanol which was stirred in 250 ml-round bottom flask using magnetic stirrer. After 2 h, 2.5 ml of TEOS was added in PAA/ethanol mixture by dropwise for 10 h maintaining vigorous stirring at room temperature. After the injection of TEOS and 4h of further reaction, PAA@SiO_2 core@shell nanoparticles with 52 nm of average outer diameter could be obtained. The synthesized PAA@SiO_2 nanoparticles were washed with distilled water several times by precipitation/redispersion methods to remove the PAA cores leaving behind the SiO_2 shells and then redispered in mixture of 100 ml of ethanol and 0.75 ml of distilled water. To form the TiO_2 outer layer on SiO_2 shell surface, 0.3 g of TBOT solved in 20 ml of ethanol was added in hollow silica shell dispersion by dropwise for 2 h and maintained with vigorous stirring at 80 ℃ for 1 h. After reaction, the

synthesized SiO_2/TiO_2 hybrid hollow multi-shell nanoparticles were purified repeatedly (three times) with ethanol to remove the unreacted precursors. The detail synthetic procedure is described elsewhere.[19,22]

3. 2. 3. Preparation of SiO_2/TiO_2 Hybrid Hollow Shell Containing OS Films

OS films containing STHs were prepared by embedding of STHs within OS matrices. 0.834 g of TEOS, 1.908 g of MTMS, 0.24 g of DMDMS, and 0.312 g of acetic acid solution (aq, 50 wt%) were first mixed and then pre-cured at room temperature for 48 h. The STHs in ethanol were added in pre-cured OS precursor mixtures and ethanol was removed by evaporation at room temperature. After solvent evaporation and 48 h of further maintenance, the mixtures were deposited on substrates using doctor blade and cured at 100 ℃ for 24 h.

3. 2. 4. Characterizations

The images of synthesized hollow nanoparticles were obtained by an energy-filtered transmission electron microscope (EF-TEM; LIBRA 120, Carl Zeiss) and the cross-sectional TEM samples were obtained with an ultra microtome (AT/ULTRACUT R, LEICA Microsystems). The morphologies of the OS hybrid films and atomic composition of hollow nanoparticles were characterized by a field-emission scanning electron microscope (FE-SEM; JSM 6071F, JEOL). The transmittance of the OS hybrid films was measured with a UV-Vis spectrometer (Lambda 35 UV/VIS Spectrometer, PERKIN

ELMER Instruments). The thermal diffusivity of the OS hybrid films was characterized by a laser flash instrument (LFA 457, NETZSCH). The specific heat of the OS hybrid films was measured with a differential scanning calorimetry (DSC; DSC 404 C, NETZSCH). The density of the OS hybrid films was measured with a dilatometer (DIL 402 C, NETZSCH).

3. 3. Results and Discussion

3. 3. 1. Synthesis and Characterization of Small-Sized Hollow Silica Shells

The HSSs were first prepared using PAA colloidal aggregates as templates, TEOS as a silica precursor, and ammonia hydroxide as a catalyst based on the modified Stöber method. The carboxylic acid groups in PAA was aminated by ammonium hydroxide (i.e., α- or β-amination) and the aminated PAA was put into the excess of ethanol, the non solvent of PAA, to form nano-sized aggregates due to their poor solubility against ethanol.[19] The TEOS was slowly injected into the aggregate solutions to form the silica shells on the aminated PAA aggregates. The size of the hollow silica shells could be manipulated by control of the PAA concentration in ethanol (see Table 3. 1). As the PAA concentration was increased, the average size and size distribution of HSSs were increased and the average outer diameter of HSSs was changed from 25 nm to 90 nm with 8 - 10 nm of shell thickness according to the PAA concentration. Figure 3. 2 presents the synthesized HSSs and their average size and size distribution. The HSSs prepared with 0.5, 1.5, 2.5, 3.5,

and 5.0 mg/ml of PAA concentration were denoted as HSS1, 3, 5, 7, and HSS10, respectively. HSS1, the smallest HSS, showed small-sized outer diameter blow than 30 nm and uniform narrow size distribution, however, the volume fraction of hollow inner space not enough to apply for thermal insulator. In the case of HSS10, broad size distribution was observed and the size of HSS10 was too large to maintain transparency in visible range. Among the HSSs, HSS5 showed appropriate particle size and reasonable size distribution for transparent and thermally insulating nano-filler within OS matrices.

Table 3. 1. Synthetic condition of HSSs

	Temp. (℃)	**PAA (g)**	**Ammonium Hydroxide (ml)**	**EtOH (ml)**	**TEOS (ml)**
HSS1	RT	0.05	5	100	2.5
HSS3	RT	0.15	5	100	2.5
HSS5	RT	0.25	5	100	2.5
HSS7	RT	0.35	5	100	2.5
HSS10	RT	0.50	5	100	2.5

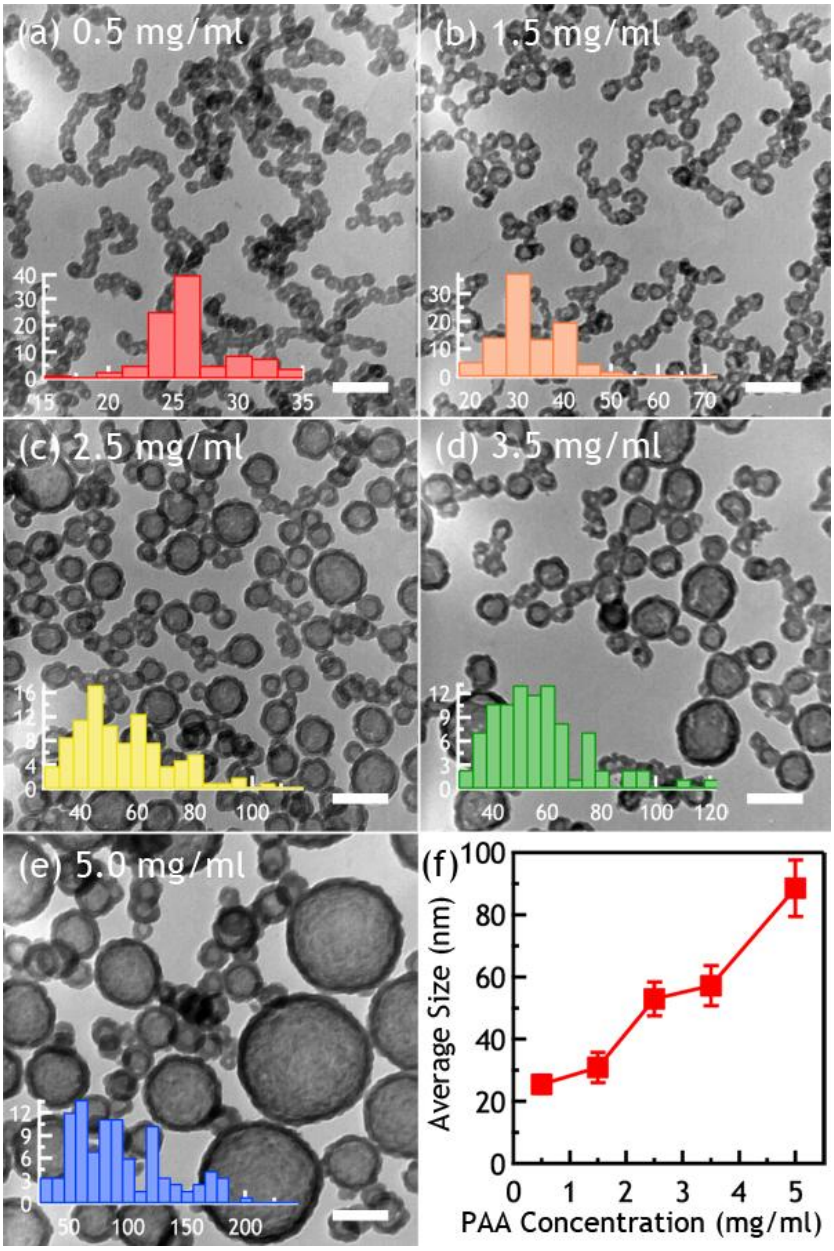

Figure 3. 2. (a-e) TEM images of HSSs with different PAA concentration (scale bars: 100 nm). Insert diagrams show the size distribution of corresponding HSSs (x-axis: outer diameter (nm), y-axis: # fraction of HSSs (%)). (f) Average size of HSSs as a function of PAA concentration.

3. 3. 2. Morphology and Transparency of HSS Containing OS Hybrid Films

To prepare OS hybrid films containing HSSs, three kinds of OS precursors, TEOS, MTMS, and DMDMS, were used. TEOS (tetravalent precursor) should enable sufficient crosslink among the OS precursors and MTMS (trivalent precursor) and DMDMS (divalent precursor) should enable stress relaxation and uniform film formation without forming cracks of TEOS-based OS films. With the mixture of 2 : 7 : 1 of TEOS : MTMS : DMDMS by molar ratio, uniform, substantial, and crack-free OS films were obtained. The morphology of HSSs within the OS matrices was characterized by FE-SEM and TEM (see Figure 3. 3). The OS hybrid films cut within liquid nitrogen to measure cross-sectional view FE-SEM. In FE-SEM images, while OS films without HSSs showed smooth and clean surface, HSS-containing OS films showed bumped and spherical texture from HSSs. As the average size of HSSs was increased, the roughness of the texture was also increased. From the crushed HSSs within the OS hybrid films, the hollow inner space of HSSs was confirmed. The hollow structure of HSSs within the OS hybrid films was also characterized by a cross-sectional view TEM. From the TEM image, we could find bright and circular spots which indicate hollow inner space of HSSs (see Figure 3. 4).

The transparency of HSS-containing OS hybrid films was measured with a UV-Vis spectrometer. To investigate the influence of HSS size within the OS hybrid films on transparency, 50 μm-thick OS hybrid films containing 5 different HSSs (HSS1, 3, 5, 7, 10) were prepared with fixed loading amount

(10 wt%) (see Figure 3. 5). The most of the OS hybrid films show extremely high transmittance about 99 % in the visible range due to the small size of HSSs except HSS10-containing OS hybrid film. In the case of the OS hybrid films containing HSS10, the films appear to be a little bit opaque and the transmittance measured is also lower than the transmittance of other OS hybrid films in the whole visible range. Because HSS10 include large-sized particles more than 100 nm and the volume fraction of HSS10 against the OS matrix is far more than other HSSs, the incident visible light is scattered off the film surface by large sized HSSs and cracks, lowering the transmittance.[16] To determine the effect of HSS concentration within OS matrices on transparency, OS hybrid films containing HSS5 and HSS7 were prepared with different loading amount (10, 20, 30 wt%) (see Figure 3. 6). As the loading amount of HSSs was increased, the transmittance of the OS hybrid films was rapidly decreased. In the case of the OS hybrid films with 30 wt% of loading amount, transmittance was almost zero and films were fragile due to the cracks formed among the HSSs. The photography of the OS hybrid films shows turbidity of the OS hybrid films according to the QD loading amount.

The volume fraction of HSSs within OS hybrid films were calculated using average size and size distribution of HSSs, average SiO_2 shell thickness, weight fraction of HSSs against whole OS hybrid films. The average SiO_2 shell thickness was assumed 9 nm for all HSSs. The calculated volume fraction of HSSs is presented in Figure 3. 7. In the case of HSSs with fixed loading amount, the volume fraction of HSSs was increased as the average size of HSSs was increased. The OS hybrid films containing HSS1, 3, 5, 7,

and HSS10 with 10 wt% of loading amount showed 10.37, 11.70, 15.45, 16.18, and 23.97 % of HSS volume fraction, respectively. The volume fraction of OS hybrid films containing HSS5 and HSS7 with different loading amount was also calculated. The OS hybrid films containing HSS5 with 10, 20, and 30 wt% of loading amount showed 15.45, 29.14, and 41.34 % of HSS volume fraction and the OS hybrid films containing HSS7 with 10, 20, and 30 wt% of loading amount showed 16.18, 30.29, and 42.69 % of HSS volume fraction, respectively. From the both of calculation results, we drew that the OS hybrid films with HSS volume fraction less than 20 % maintain high transparency in visible range. On the other hand, the OS hybrid films with HSS volume fraction more than 20 % were turbid, in particular, the OS hybrid films with HSS volume fraction more than 40 % were totally turbid.

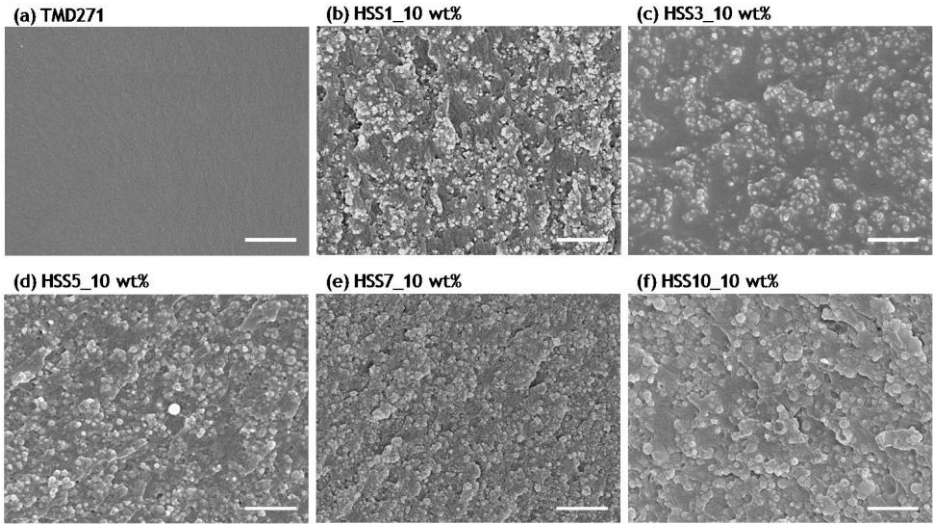

Figure 3. 3. The cross-sectional view FE-SEM images of (a) OS films without HSSs and (b-f) OS hybrid films containing HSS1, 3, 5, 7, and HSS10. The loading amount of HSSs was 10 wt% fixed (scale bars: 1 μm).

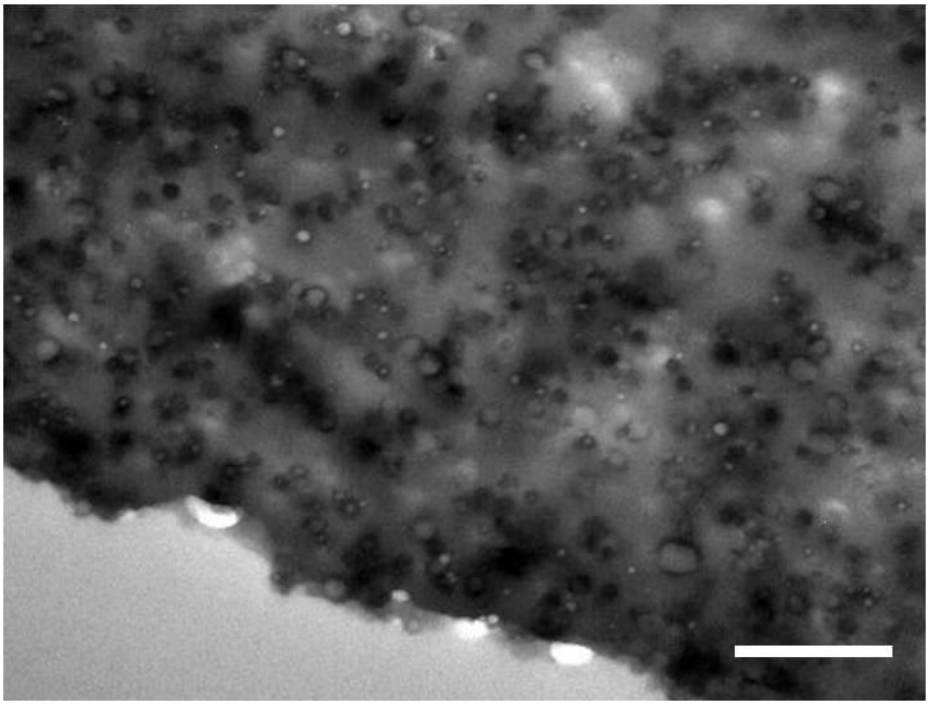

Figure 3. 4. The cross-sectional view TEM image of OS hybrid films containing 10 wt% of HSS5. (scale bars: 500 nm).

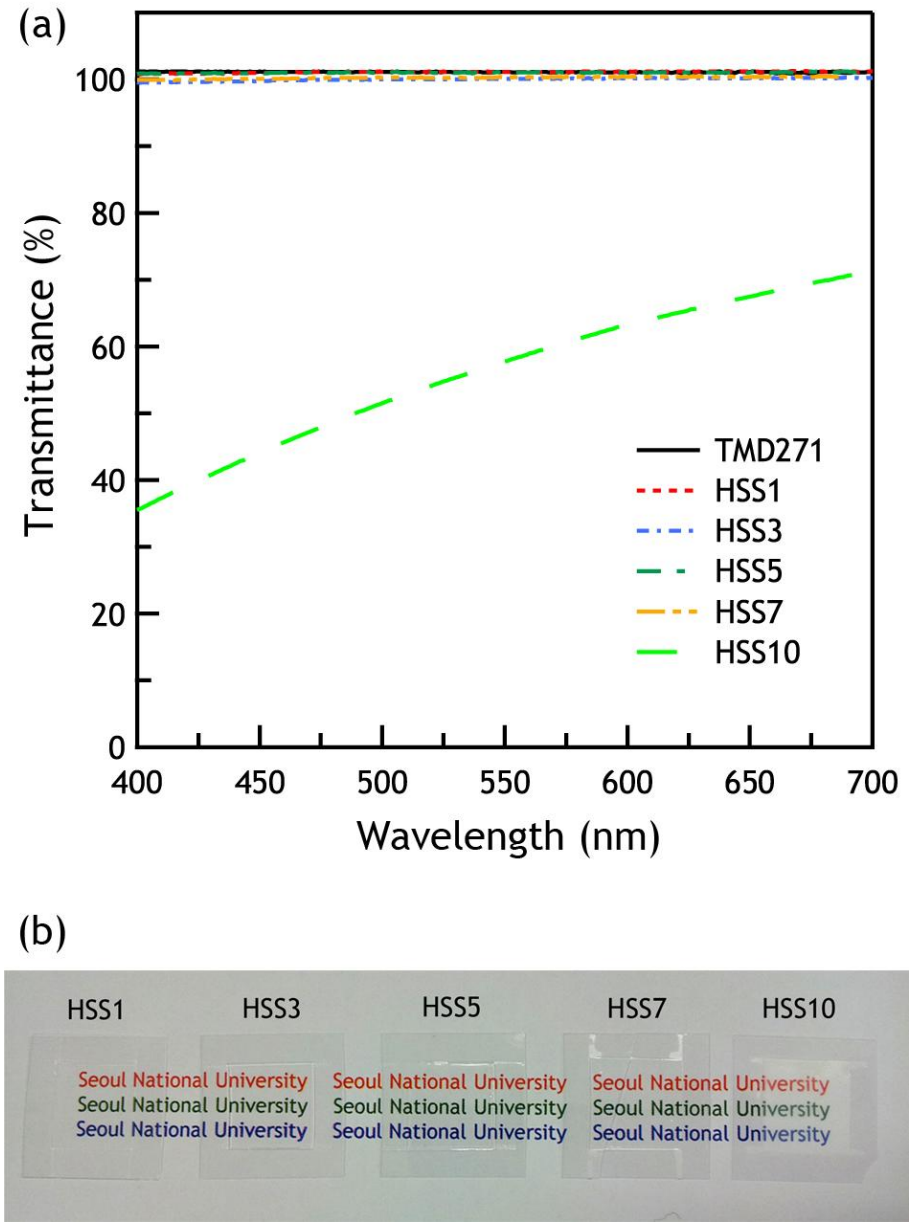

Figure 3. 5. (a) Transmittance and (b) photograph of OS hybrid films containing various HSSs with fixed loading amount (10 wt%) (film thickness: ~ 50 μm).

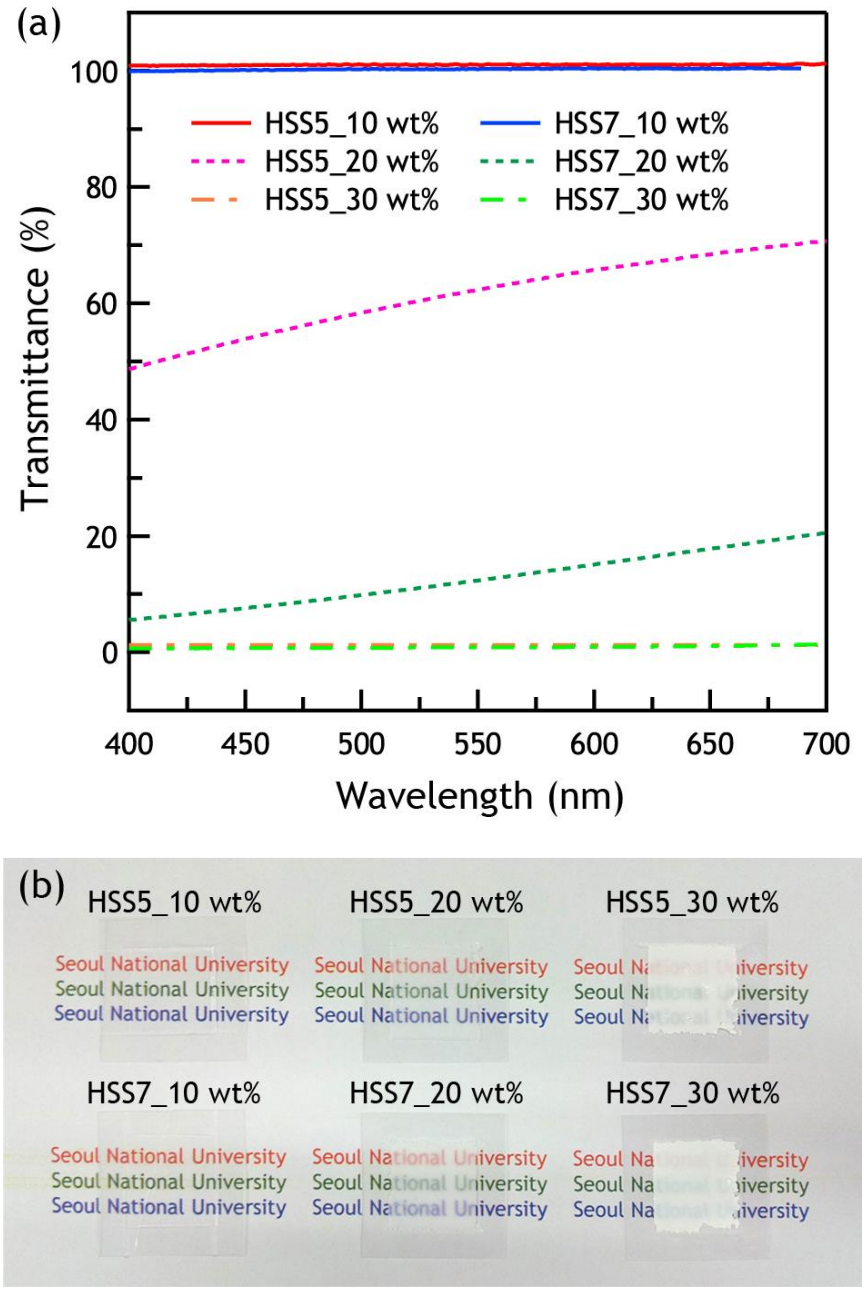

Figure 3. 6. (a) Transmittance and (b) photograph of OS hybrid films containing HSS5 and HSS7 with different loading amounts (film thickness: ~ 50 μm).

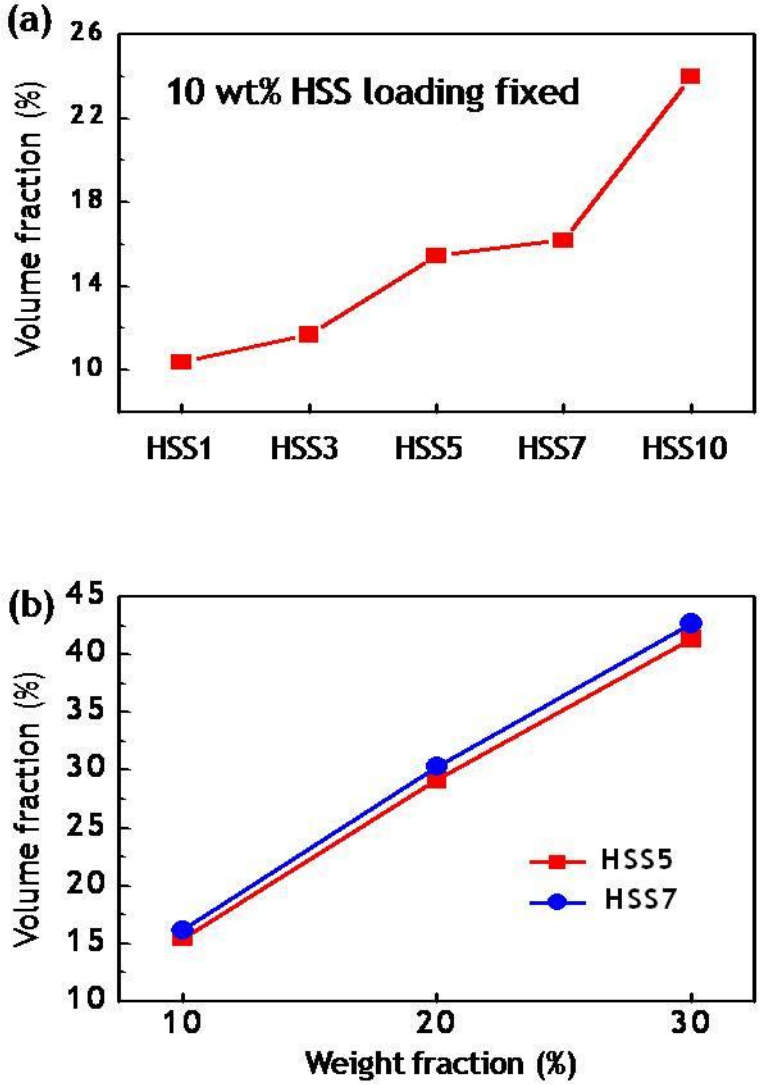

Figure 3. 7. (a) The volume fraction of HSSs against whole OS hybrid films with fixed loading amount (10 wt%). (b) The volume fraction of HSS5 and HSS7 against whole OS hybrid films with different loading amount (10, 20, 30 wt%).

3. 3. 3. Synthesis and Characterization of Silica/Titania Hybrid Hollow Shells

To introduce UV-blocking property into the OS hybrid films, SiO_2/TiO_2 hybrid hollow shells (STHs) were prepared. HSS5 showing appropriate particle size and reasonable size distribution was applied as a HSS template for TiO_2 shell formation.[23] TiO_2 outer layer was coated onto the SiO_2 shell surface by sol-gel method.[22] SiO_2/TiO_2 hybrid hollow shells prepared using HSS5 were denoted as STH5. To minimize the change in the volume fraction of hollow inner space in overall films due to the increase in outer diameter by the additional formation of TiO_2 outer layer, which directly influences the thermal insulation, as well as the reduction in optical transmittance in the OS hybrid films containing SiO2/TiO2 hybrid hollow shells by the increase in the size of hollow spheres and the large difference in refractive index between SiO_2 and TiO_2, a trace of TiO_2 were formed on HSS5 surface. The prepared STH5 showed almost same average diameter and size distribution with HSS5. To confirm the formation of TiO_2 layer on the SiO_2 shell surface, the surface morphology of HSS5 and STH5 was examined by TEM with high magnification. In the TEM images, while HSS5 showed a smooth and clean surface (Figure 3. 8(a)), STH5 showed nano-sized bumpy textures which are believed to be TiO_2 nanoparticles (not as a layer) grown mostly on top of the SiO2 shell surface (Figure 3. 8(b)). To further characterize the composition of TiO2, the atomic % of the hollow spheres was analyzed by EDX (Figure 3. 8(c)). The EDX spectra represent the distinct peaks of Si, C, O, and Ti and their atomic %.[25] In the case of HSS5, Si and O from silica shell and C from

unreacted ethoxy groups in TEOS were observed. In the case of STH5, Ti from TiO_2 shell was additionally detected and the atomic % of Ti was only 0.1 %. It means that tiny amount of TiO_2 was formed onto the SiO_2 shell surface which is barely observed by TEM measurement. Furthermore, STH5 shows relatively high Si atomic % and low C and O atomic % compared with HSS5 in consequence of further condensation of unreacted ethoxy groups in TEOS during the TiO_2 shell formation.

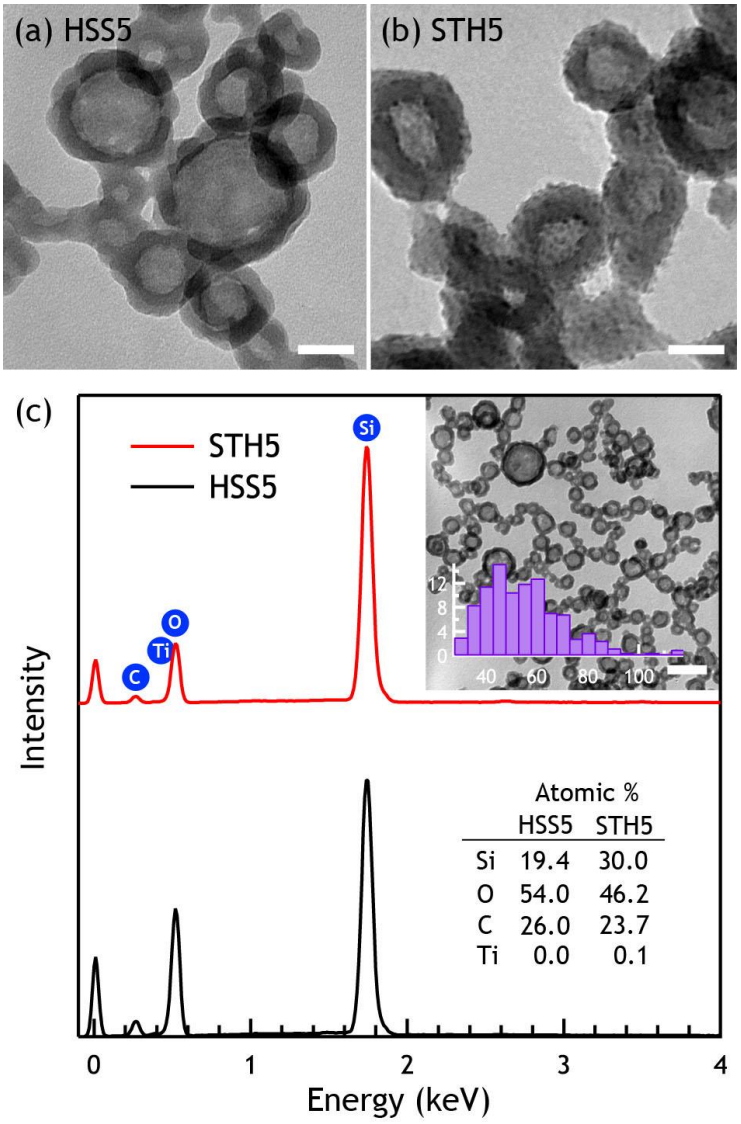

Figure 3. 8. TEM images of (a) HSS5 and (b) STH5 (scale bars: 30 nm). (c) EDX spectra and the atomic composition of HSS5 and STH5. Insert picture and diagram show the TEM image with the size distribution of STH5 (scale bar: 100 nm).

3. 3. 4. Optical and Thermal Properties of STH-containing OS Hybrid Films

To characterize transparency and UV-blocking property of the STH-containing OS hybrid films, the transmittance of STH-containing OS hybrid films was measured with a UV-Vis spectrometer from visible to UV range. The OS hybrid films containing STH5 with different loading amount (2, 5, 10 wt%) and reference OS films without STH5, TMD271, were prepared for transmittance measurement (film thickness: ~ 50 μm). In the visible range, all the films showed excellent transparency more than 95 %, on the other hand, in UV region, the transmittance of STH5-containing OS hybrid films was rapidly decreased due to the UV-absorption property of TiO_2 (see Figure 3. 9). The UV absorption property of OS hybrid films was thoroughly investigated according to the type of UV light (see Figure 3. 10). UV light was divided into 3 regions, UVA (400-315 nm), UVB (315-280 nm), UVC (280 nm-). In UVA region, all the OS hybrid films showed relatively high transmittance more than 90 %. However, from UVB region, the transmittance of OS hybrid films was rapidly decreased due to the UV-absorption by STH5. In UVC region, most of the UV light was absorbed by OS hybrid films. The UV-blocking property of OS hybrid films was increased as the loading amount of STH5 was increased. In the case of the OS hybrid films containing 10 wt% of STH5, 8.0 % of UVA, 66.2 % of UVB, and 99.4 % of UVC were blocked by OS hybrid films.

To investigate the thermally insulating property of the OS hybrid films, thermal conductivity of the OS hybrid films was calculated. Thermal

conductivity is represented as the product of thermal diffusivity, specific heat, and density. Thermal diffusivity, specific heat, and density of the OS hybrid films were measured with laser flash instrument, DSC, and dilatometer, respectively. The thermal diffusivity of OS hybrid films was measured with flash method (see Figure 3. 11). The details about laser flash method for thermal diffusivity measurement could be obtained from corresponding references.[26,27] The thermal diffusivity of the OS hybrid films containing STH5 with 10 wt% of loading amount were decreased about 18 % compared with the OS films without STH5, TMD271 (film thickness: ~ 200 μm). We assume the reason of reduced thermal diffusivity of OS hybrid films is that the hollow inner space in the OS hybrid films interrupts the heat flow across the films and traps the heat their inside. And the specific heat of OS hybrid films was a little bit increased and the density was slightly decreased compared with OS films without STH5 due to their hollow inner space. As a result, the thermal conductivity of OS hybrid films (0.201 W/m·K) was decreased about 20 % compared with the thermal conductivity of OS films (0.252 W/m·K). 20 % of decrease in thermal conductivity is meaningful value for thermal insulator (see Table 3. 2).

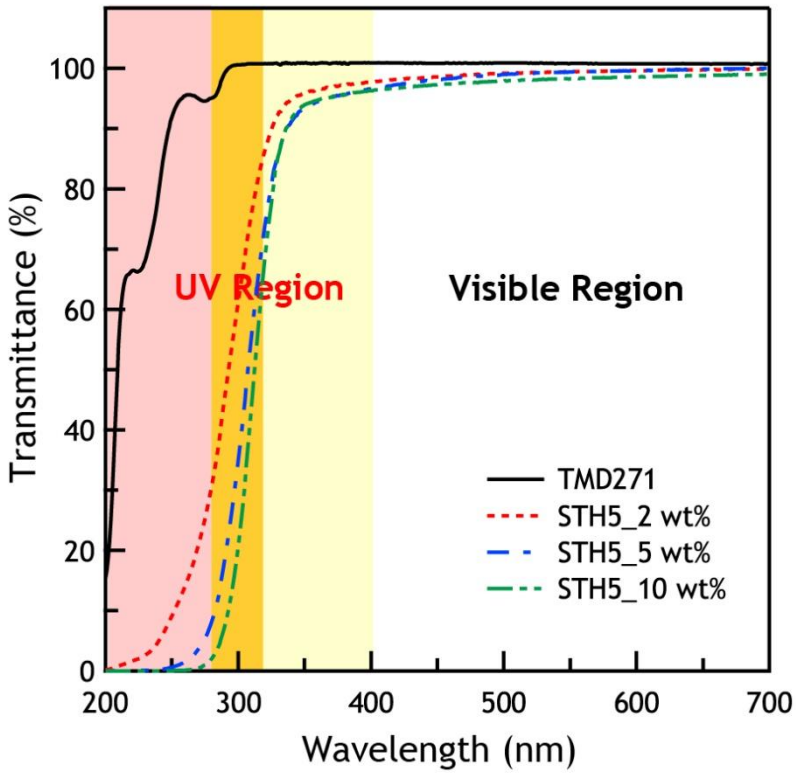

Figure. 3. 9. Transmittance of OS hybrid films containing STH5 with different loading amounts from visible to UV range (film thickness: ~ 50 μm).

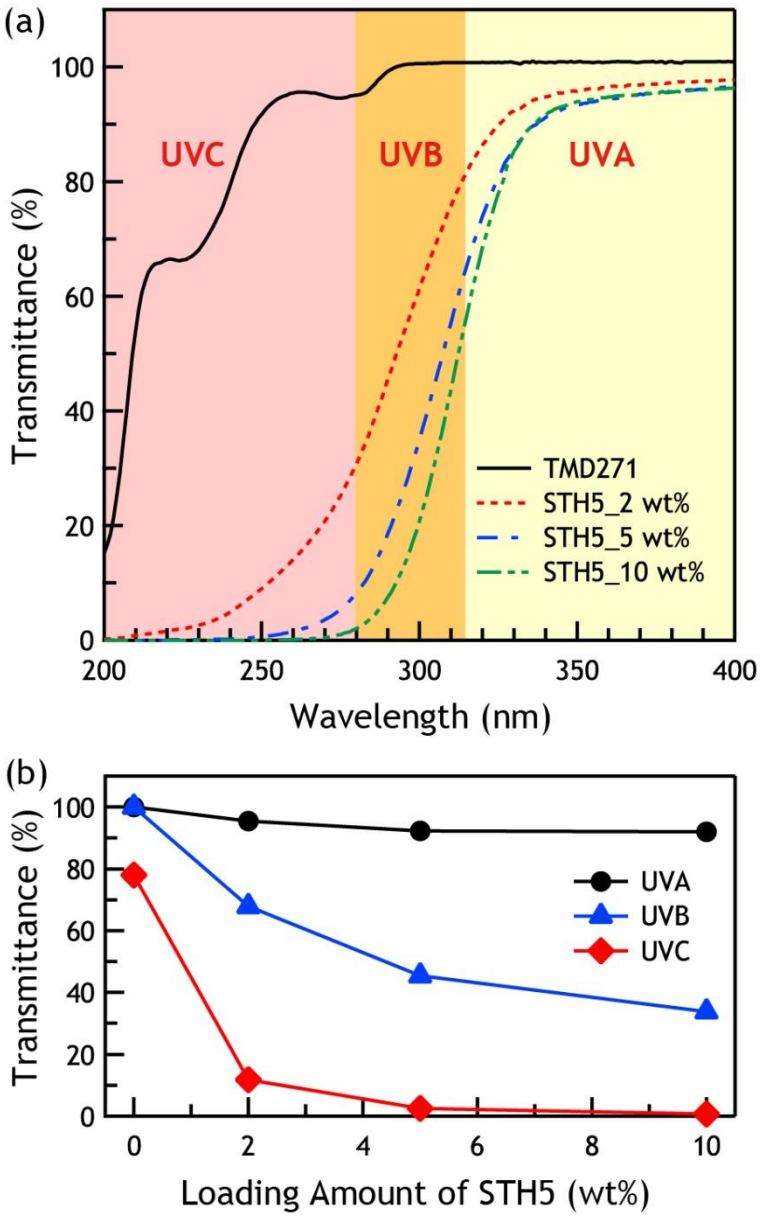

Figure 3. 10. (a) Magnified UV-Vis spectra in UV region (film thickness: ~ 50 μm). (b) Classified transmittance of OS hybrid films containing STH5 with different loading amounts by type of UV light.

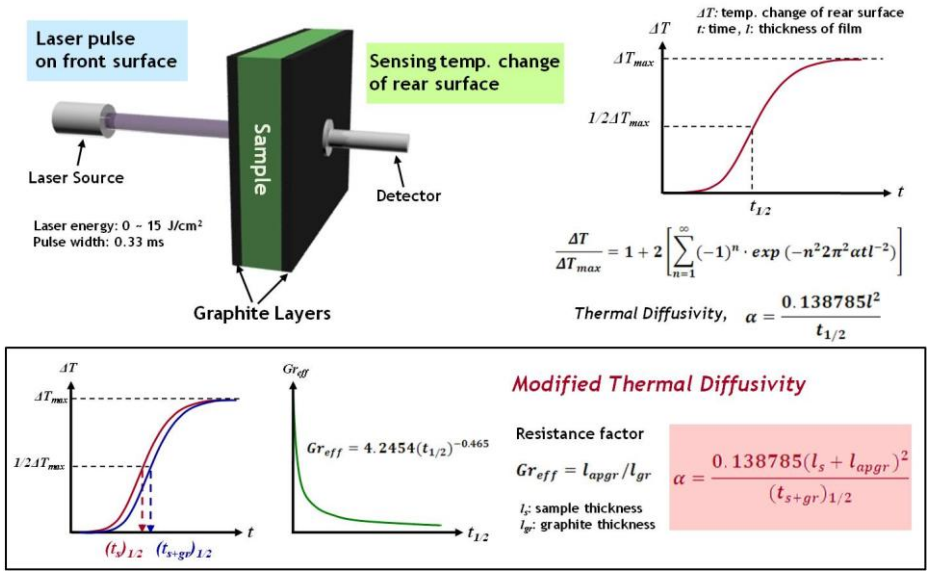

Figure 3. 11. Schematic illustration of flash method for thermal diffusivity measurement.

Table 3. 2. Thermal diffusivity, specific heat, density, and thermal conductivity of OS films (TMD271) and OS hybrid films containing 10 wt% of STH5 (film thickness: ~ 200 μm)

	Thermal Diffusivity (α, mm^2/s)	**Specific Heat (Cp, J/g·K)**	**Density (ρ, g/cm^3)**	**Thermal Conductivity (W/m·K)**
W/o STH5	0.149	1.283	1.320	0.252
STH5_10 wt%	0.122	1.341	1.232	0.201

3. 4. Conclusion

Transparent, thermally insulating, and UV-blocking OS hybrid films were prepared based on nano-sized silica/titania hybrid hollow shells (STHs). HSSs were first synthesized using nano-sized PAA colloidal aggregates as template, and TEOS as a silica precursor. The average size of HSSs was varied from 25 nm to 90 nm by control of PAA concentration. And TiO_2 shells were then formed onto HSS surface to introduce UV-blocking property. The prepared OS hybrid films containing STHs showed high transparency in visible range due to small-sized STHs about 50 nm as well as excellent UV-blocking property due to the UV-absorbing nature of TiO_2. Furthermore, OS hybrid films presented reduced thermal conductivity compared with OS films without STHs because the hollow inner space within the STHs the interruption of heat flow and the reduction of thermal diffusivity of the OS hybrid films. With these advantages, transparent OS hybrid films with thermally insulating and UV-blocking properties were successfully achieved.

3. 5. References

(1) Caruso, F.; Caruso, R. A.; Möhwald, H. *Science* **1998**, *282*, 1111.

(2) Lim, Y. T.; Kim, J. K.; Noh, Y.-W.; Cho, M. Y.; Chung, B. H. *Small* **2009**, *5*, 324.

(3) Jovanovic, A. V.; Flint, J. A.; Varshney, M.; Morey, T. E.; Dennis, D. M.; Duran, R. S. *Biomacromolecules* **2006**, *7*, 945.

(4) Kamata, K.; Lu, Y.; Xia, Y. *J. Am. Chem. Soc*. **2003**, *125*, 2384.

(5) Chen, J.-F.; Ding, H.-M.; Wang, J.-X.; Shao, L. *Biomaterials* **2004**, *25*, 723.

(6) Du, L.; Liao, S.; Khatib, H. A.; Stoddart, J. F.; Zink, J. I. *J. Am. Chem. Soc*. **2009**, *131*, 15136.

(7) Slowing, I. I.; Trewyn, B. G.; Giri, S.; Lin, V. S.-Y. *Adv. Funct. Mater*. **2007**, *17*, 1225.

(8) Zhou, J.; Wu, W.; Caruntu, D.; Yu, M. H.; Martin, A.; Chen, J. F.; O'Connor, C. J.; Zhou, W. L. *J. Phys. Chem. C* **2007**, *111*, 17473.

(9) Joo, S. H.; Park, J. Y.; Tsung, C.-K.; Yamada, Y.; Yang, P.; Somorjai, G. A. *Nat. Mater*. **2009**, *8*, 126.

(10) Arnal, P. M.; Comotti, M.; Schüth, F. *Angew. Chem. Int. Ed*. **2006**, *45*, 8224.

(11) Chen, G.; Xia, D.; Nie, Z.; Wang, Z.; Wang, L.; Zhang, L.; Zhang, J. *Chem. Mater*. **2007**, *19*, 1840.

(12) Moon G. D.; Jeong, U. *Chem. Mater*. **2008**, *20*, 3003.

(13) Yung, K. C.; Zhu, B. L.; Yue, T. M.; and Xie, C. S. *Compos. Sci. Technol*.

2009, *69*, 260.

(14) Yuan, J.; Zhou, G.; Pu, H. *J. Membrane Sci*. **2008**, *325*, 742.

(15) Zou, H.; Wu, S.; Shen, J. *Chem. Rev*. **2008**, *108*, 3893.

(16) Naganuma, T.; Kagawa, Y. *Compos. Sci. Technol*. **2002**, *62*, 1187.

(17) Graf, C.; Vossen, D. L. J.; Imhof, A.; van Blaaderen, A. *Langmuir* **2003**, *19*, 6693.

(18) Darbandi, M.; Thomann, R.; Nann, T. *Chem. Mater*. **2007**, *19*, 1700.

(19) Wan, Y.; Yu, S.-H. *J. Phys. Chem. C* **2008**, *112*, 3641.

(20) Darbandi, M.; Thomann, R.; Nann, T. *Chem. Mater*. **2005**, *17*, 5720.

(21) Khanal, A.; Inoue, Y.; Yada, M.; Nakashima, K. *J. Am. Chem. Soc*. **2007**, *129*, 1534.

(22) Song, X.; Gao, L. *J. Phys. Chem. C* **2007**, *111*, 8180.

(23) Seriani, N.; Pinilla, C.; Cereda, S.; Vita, A. D.; Scandolo, S. *J. Phys. Chem. C* **2012**, *116*, 11062.

(24) Yang, H.; Zhu, S.; Pan, N. *J. Appl. Polym. Sci*. **2004**, *92*, 3201.

(25) Guo, Y.-G.; Hu, J.-S.; Liang, H.-P.; Wan, L.-J.; Bai, C.-L. *Adv. Funct. Mater*. **2005**, *15*, 196.

(26) Kim, S.-K.; Kim, Y.-J. *Thermochim. Acta* **2008**, *468*, 6.

(27) Lim, K.-H.; Kim, S.-K.; Chung, M.-K. *Thermochim acta* **2009**, *494*, 71.

Chapter 4. High Performance GaN LEDs Based on Hollow Silica Shell-Coated Sapphire Substrates

4. 1. Introduction

GaN, III-V compound semiconductor, have received immense attention as a blue light-emitting source for optoelectronic devices such as light-emitting diodes (LEDs) and laser diodes (LDs).[1-3] Particularly, white LEDs based on GaN LEDs have been widely used from lightings to back light unit for display. GaN LEDs are typically prepared using sapphire substrate for heteroepitaxial growth of GaN films. However, there are several problems lowering device efficiency of GaN LEDs originated from different material properties between GaN and sapphire.

Dislocations generate within GaN film during the GaN film growth due to the lattice mismatch at the interface of GaN and sapphire, and such dislocations reduce the internal efficiency of GaN LEDs.[4,5] Total internal reflection which occurs within the GaN films due to the different refractive[6] index of GaN and sapphire decreases the external efficiency of GaN LEDs.[7-10] In addition, different thermal expansion coefficient of GaN and sapphire induce the wafer bowing during GaN growth process and compressive stress is pressurized on the bended GaN films. Wafer bowing is also a disadvantage in LED chip fabrication process.

To overcome such problems, various growth strategies for GaN films were

developed. Most of all, epitaxial lateral overgrowth (ELO) is renown as s representative process for high quality GaN film growth. The dislocation density on GaN films surface were effectively reduced with ELO. For ELO of GaN, SiO_2 mask coated[11-14] or patterned[15] sapphire substrates have been typically used. In addition, void-embedding GaN films were grown using muti-step GaN growth including patterning and etching process.[16-18] However, these methods require complex fabrication process and high cost. Solution processible silica spheres were applied on sapphire substrates as a mask for simple fabrication process, but there is no advance in wafer bowing problem.[19,20]

Herein, we propose simple and effective strategy for bowing-free and high quality GaN film growth based on hollow silica shell (HSS)-coated sapphire substrates (see Figure 4. 1). HSSs were readily prepared by sol-gel reaction and HSS monolayers were uniformly deposited on large-aread sapphire substrates based on simple solution process. ELO of GaN films were successfully induced by HSSs playing the role of mask and the crystallinity of GaN films prepared using HSS-coated sapphire substrates were remarkably improved. In addition, irregular reflection by bumped texture of HSS-coated sapphire substrates and reduced refractive index of GaN film by hollow inner space reduced total internal reflection within GaN films. As a result, the internal and the external efficiency of GaN LEDs were improved with HSS-coated sapphire substrates. Furthermore, the compressive stress in GaN films were relaxed by deformation of HSS and wafer bowing problem on GaN films

were relieved.[21] With these advantages, bowing-free and highly efficient GaN LEDs were realized.

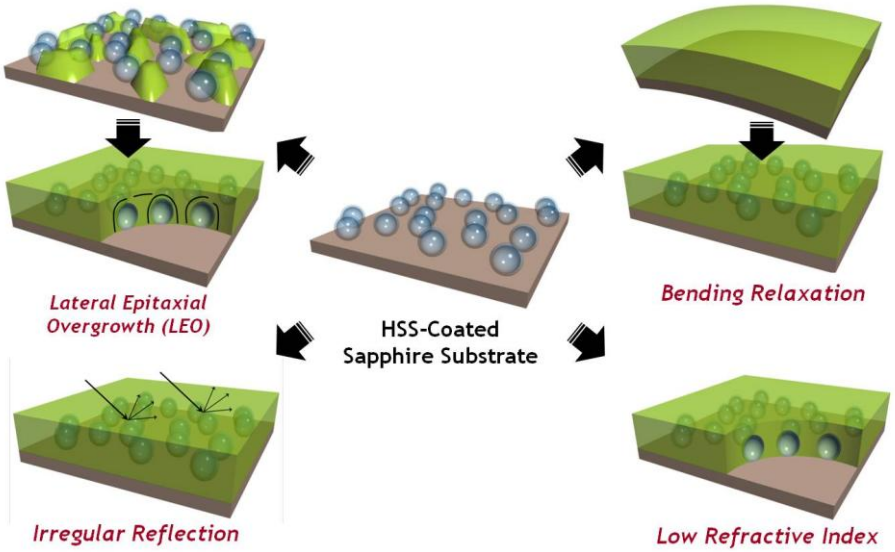

Figure 4. 1. Benefits from HSS-coated sapphire substrates.

4. 2. Experimental Details

4. 2. 1. Chemicals

Styrene (99 %), 2,2-azobis-(isobutyramidine) dihydrochloride (AIBA, 97 %), polyvinylpyrrolidone (PVP, Mw= 55K and 360K), tetraethyl orthosilicate (TEOS, 98 %), hexyltrimethoxysilane (HTMS, 98 %), ammonium hydroxide solution (aq, 28-30 %), polyallylamine hydrochloride (PAH, Mw= 70K), and polysodium 4-styrene sulfonate (PSS, Mw= 70K) were used as purchased from Aldrich. Sapphire substrates were purchased from Crystal-On (thickness: 340 μm).

4. 2. 2. Synthesis of PS/SiO_2 Core/Shell Nanospheres

Positively charged polystyrene nanospheres (PS NSs) were first synthesized using styrene as a monomer, AIBA as an initiator as well as the surfactant, and PVP (55K) as a stabilizer and a cosurfactant by dispersion polymerization. PS/SiO_2 core/shell nanospheres with negatively charged surface were then prepared using positively-charged PS nanosphere as a template, TEOS as a silica precursor, and ammonium hydroxide as a catalyst by the sol-gel method. The detail synthetic procedure is described elsewhere.[22]

4. 2. 3. Deposition of Hollow Silica Shell Monolayers on Sapphire Substrates

The sapphire substrates were first cleaned by piranha treatment (H_2SO_4 : H_2O_2 = 7 : 3 in volume ratio). To make negatively-charged surface, piranha

treated sapphire substrates were placed in RCA solution (H_2O : ammonium hydroxide : H_2O_2 = 5 : 1 : 1 in volume ratio) at 50 ℃ for 3 minute. After RCA treatment, PAH, positively-charged polyelectrolyte, in H_2O (1 mg/ml) was deposited on the sapphire substrates by spin casting. PSS, negatively-charged polyelectrolyte, in H_2O (1 mg/ml) was then deposited on the PAH-coated sapphire substrates by spin casting. And PAH deposition was repeated on PAH/PSS-coated sapphire substrates. In every deposition step, the residual, not adsorbed, polyelectrolyte on the substrates was removed using distilled water (2 times). To prepare HSS monolayer coated sapphire substrates, the PAH/PSS/PAH multilayered thin film-coated sapphire substrates were dipped in PS/SiO_2 NSs dispersion with different PS/SiO_2 NS concentration and dipping time. The residual, not adsorbed, PS/SiO_2 on the substrates was removed by dipping in distilled water (3 times). The PS/SiO_2 coated sapphire substrates were calcinated under air flow at 700 ℃ for 1 h to remove the PS core within PS/SiO_2 and the polyelectrolyte multilayered thin films on sapphire substrates.

4. 2. 4. Growth of GaN Films on HSS-Coated Sapphire Substrates

GaN films were grown on HSS-coated sapphire substrates using low pressure metal-organic chemical vapor deposition (MOCVD). The surface of HSS-coated sapphire substrates was first cleaned by thermal treatment at 1100 ℃. The buffer GaN grains, seed GaN, were grown on HSS-coated sapphire substrates by low temperature growth at 500 ℃. Trimethylgallium

(TMGa) and NH_3 were used as GaN precursors. After low temperature growth, high quality GaN films were grown on buffer GaN grain coated substrates by high temperature growth at 1080 ℃. The crystal quality of GaN films were manipulated by varying the growth pressure.

4. 2. 5. Fabrication of GaN LEDs Using HSS-Coated Sapphire Substrates

The blue GaN LEDs were prepared using 3 μm-thick GaN films grown on HSS-coated substrates as a buffer GaN, undoped GaN, layer. 2 μm-thick n-doped GaN films were grown on the buffer GaN layer. 4 bilayers of GaN/InGaN thin films were grown as a multi-quantum well (MQW) on the n-doped GaN layer. The thickness of GaN and InGaN thin film consisting MQW were 100 Å and 30 Å, respectively. 160 nm-thick p-doped GaN films were grown on the MQW layer. The multilayered GaN films were patterned by conventional lithography to form the matel pad on the n-doped GaN layer. Ti/Al/Au pads were deposited on the patterned n-doped GaN layer. Thin indium tin oxide (ITO) films were deposited on p-doped GaN layer. Ni/Au pads were deposited on the ITO layer.

4. 2. 6. Characterizations

The shape & size of PS NSs, PS/SiO_2 NSs and HSSs and morphology of PS/SiO_2 NSs and HSSs on sapphire substrates were characterized by Field-Emission Scanning Electron Microscope (FE-SEM; JSM 6071F, JEOL). The hollow structure of HSSs was observed by energy-filtered transmission

electron microscope (EF-TEM; LIBRA 120, Carl Zeiss). The weight fraction of PS cores within the PS/SiO_2 NSs was obtained by thermogravimetric analysis (TGA). The surface charge of PS NSs and PS/SiO_2 NSs was measure with electrophoretic light scattering spectrophotometer (ELS-8000, Ostka).

4. 3. Results and Discussion

4. 3. 1. Synthesis and Characterization of PS/SiO_2 NSs

Positively charged PS NSs were first synthesized using styrene as a monomer, AIBA as an initiator as well as the surfactant, and PVP as a stabilizer and a cosurfactant by dispersion polymerization (see Figure 4. 2). The size of PS NSs could be manipulated by control of the concentration of reactants. As the concentration of styrene and AIBA were increased, and as the concentration of PVP was decreased, the size of PS NSs was increased. The size of PS NSs was varied from 155 nm to 530 nm (see Figure 4. 3). The synthetic condition of PS NSs was presented in Table 4. 1. The synthesized PS NPs showed uniform size and narrow size distribution. The surface charge of PS NSs was measure with electrophoretic light scattering spectrophotometer. The ζ-potential of PS NSs was 31 mV. The surface of PS NSs was positively charged due to the positively charged initiator, AIBA.

The PS/SiO_2 core/shell NSs were synthesized using positively-charged PS NSs as templates, TEOS as a silica precursor, and ammonium hydroxide as a catalyst by sol-gel method. The silica shells were effectively formed on PS NS surface due to positively-charged PS NS surface. The thickness of SiO_2 shells could be manipulated by control the concentration of TEOS and ammonium hydroxide. As the concentration of TEOS and ammonium hydroxide were increased, the thickness of SiO_2 shells was increased. The thickness of SiO_2 shells was varied from 10 nm to 90 nm (see Figure 4. 4). The synthetic condition of SiO_2 shells was presented in Table 4. 2. The synthesized PS/SiO_2

NPs showed uniform size and narrow size distribution (see Figure. 4. 5). The ζ-potential of PS/SiO_2 NSs was -43 mV. The surface of PS NSs was negatively charged due to the residual silanol (Si-OH) groups on SiO_2 shells.

To make hollow silica shells, the PS cores within the PS/SiO_2 NSs were removed by calcination. The PS/SiO_2 NSs were heated using furnace under air flow at 700 ℃ for 1 h. The weight loss of PS/SiO_2 NSs was monitored by TGA according to the SiO_2 shell thickness (see Figure 4. 6). The thermal decomposition of PS cores started around 300 ℃. As the SiO_2 shell thickness was increased, the decomposition temperature was also increased, and the weight ratio of PS cores against the PS/SiO_2 was decreased. The HSSs obtained by thermal treatment showed same size & shape with corresponding PS/SiO_2 NSs (see Figure 4. 7 and 4. 8). However, in the case of PS/SiO_2 with thin SiO_2 shells less than 10 nm-thick, the HSSs collapsed because the mechanical strength of SiO_2 shells was not enough to maintain the hollow structure (see Figure 4. 9). As a result, a deflated beach ball shaped structure was obtained with thin SiO_2 shells after thermal treatment.

The shell composition and porosity were manipulated by control of silica precursors. Two types of silica precursors, TEOS and HTMS, were used for shell formation. HTMS have 6 numbered-alkyl, hexyl, chain which slow down the sol-gel reaction. The mixture of TEOS and HTMS were used for shell formation with different mixing ratio. The molar ratio of HTMS in TEOS/HTMS mixture was changed from 2 to 20 mol%. The thickness of SiO_2 shells was changed according to the HTMS mixing ratio (see Figure 4. 10 and 4. 11(a)). As mixing ratio of HTMS was increased, thickness of silica shells

was decreased. With 2, 5, 10, and 20 mol% of HTMS mixing ratio, 30, 21, 13, and 10 nm-thick SiO_2 shells were formed. Because the HTMS (trivalent precursor) have less reaction sites than TEOS (tetravalent precursor) and hexyl chains on HTMS hinder sol-gel reaction among the precursors, the reaction rate and yield of sol-gel reaction were decreased with HTMS.

The porosity of silica shells was also changed according to the HTMS concentration. The pore size and pore volume of HSSs synthesized using TEOS and HSSs synthesized using TEOS/HTMS mixture (TEOS : HTMS = 95 : 5 in molar ratio) were measured with N_2 adsorption BET analysis (see Figure 4. 11(b)). The pore volume of HTMS mixed sample was larger than the pore volume of reference, TEOS only, sample. The reason of increased pore volume is that the hexyl chains in HTMS were burn out during calcinations and leaving behind empty space. As a result, the number of pore was increased with higher HTMS mixing ratio. The porosity of SiO_2 shells influenced on the mechanical property of SiO_2 shells. The HSSs with high HTMS concentration (10 and 20 mol%) couldn't maintain the hollow structure and collapsed. This is the result from the reduced mechanical strength of SiO_2 shells due to the increased porosity.

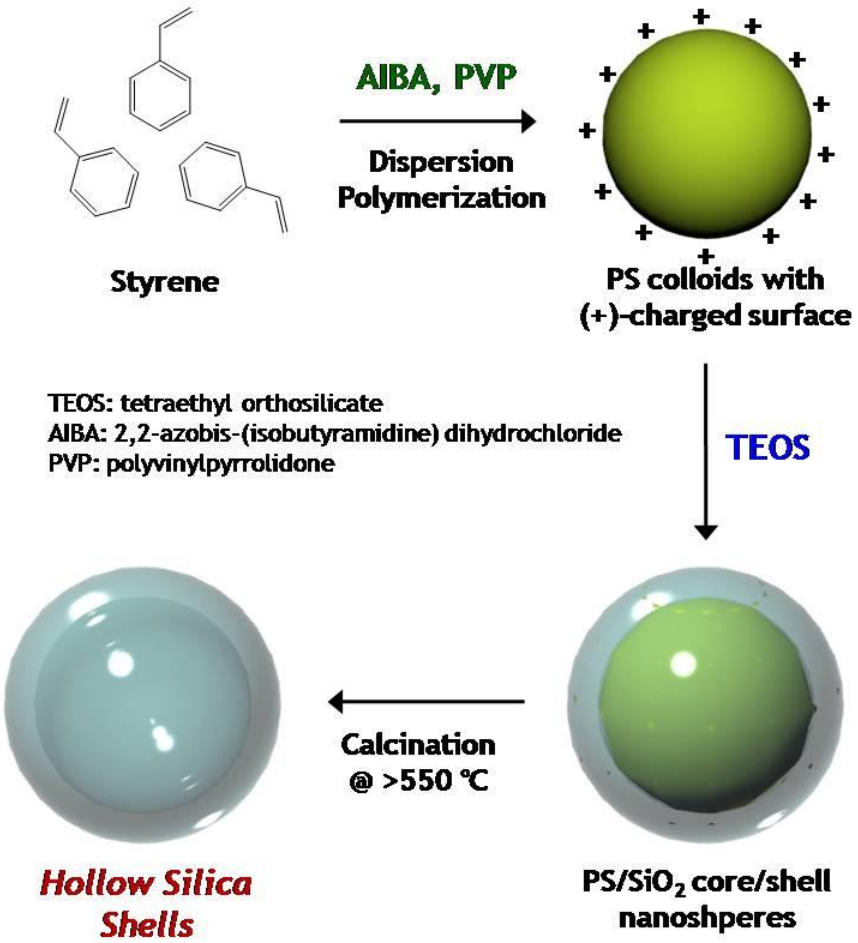

Figure 4. 2. A schematic on the preparation of hollow silica shells.

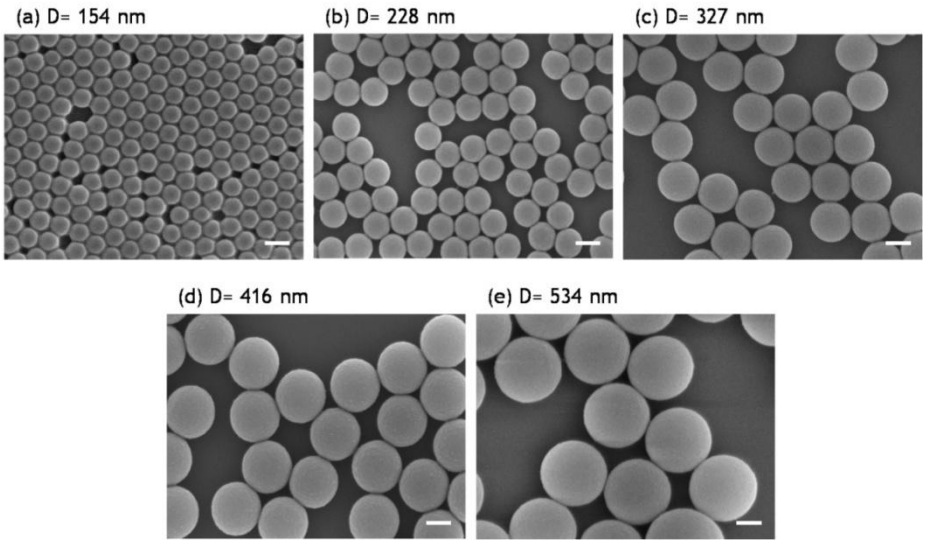

Figure 4. 3. FE-SEM images of PS NSs prepared with different size (D: diameter, scale bars: 200 nm).

Table 4. 1. Synthetic condition of PS NSs

H_2O (ml)	Styrene (ml)	AIBA (g)	PVP (g)	Diameter (nm)	PDI (%)
20	1	0.06	0.25	154	3.33
20	2	0.06	0.25	228	2.19
20	4	0.12	0.25	327	2.23
20	4	0.06	0.25	416	1.15
20	8	0.06	0.25	534	1.46

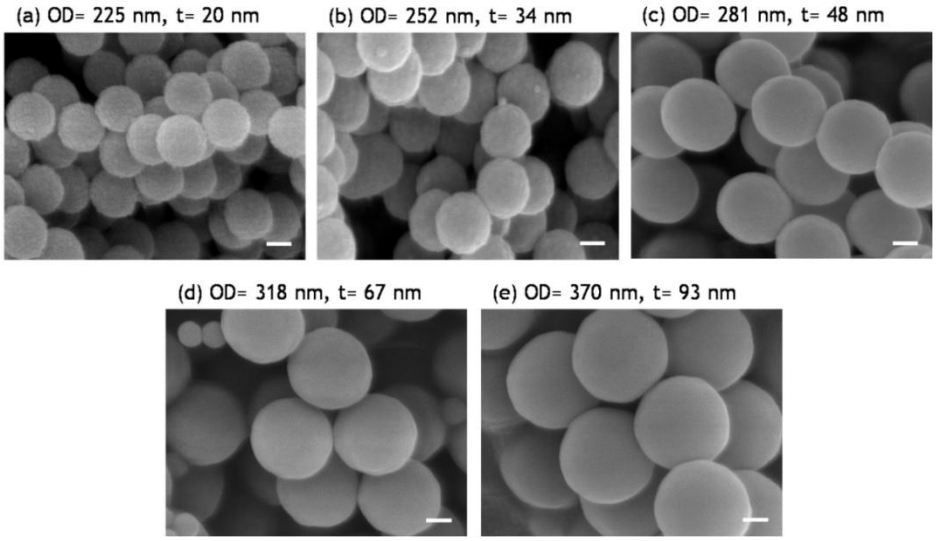

Figure 4. 4. FE-SEM images of PS/SiO_2 core/shell NSs prepared with different SiO_2 shell thickness (PS core diameter: 185 nm, OD: outer diameter, t: shell thickness, scale bars: 100 nm).

Table 4. 2. Synthetic condition of SiO_2 shells (size of PS core: 185 nm)

EtOH	PS (3.85 wt% in EtOH; ml)	TEOS (ml)	Ammonium Hydroxide (ml)	Outer Diameter (nm)	Shell Thickness (nm)
19	1	0.5	0.05	225	20
19	1	0.5	0.1	252	34
19	1	1.0	0.1	281	48
19	1	0.5	0.2	318	67
19	1	1.0	0.2	370	93

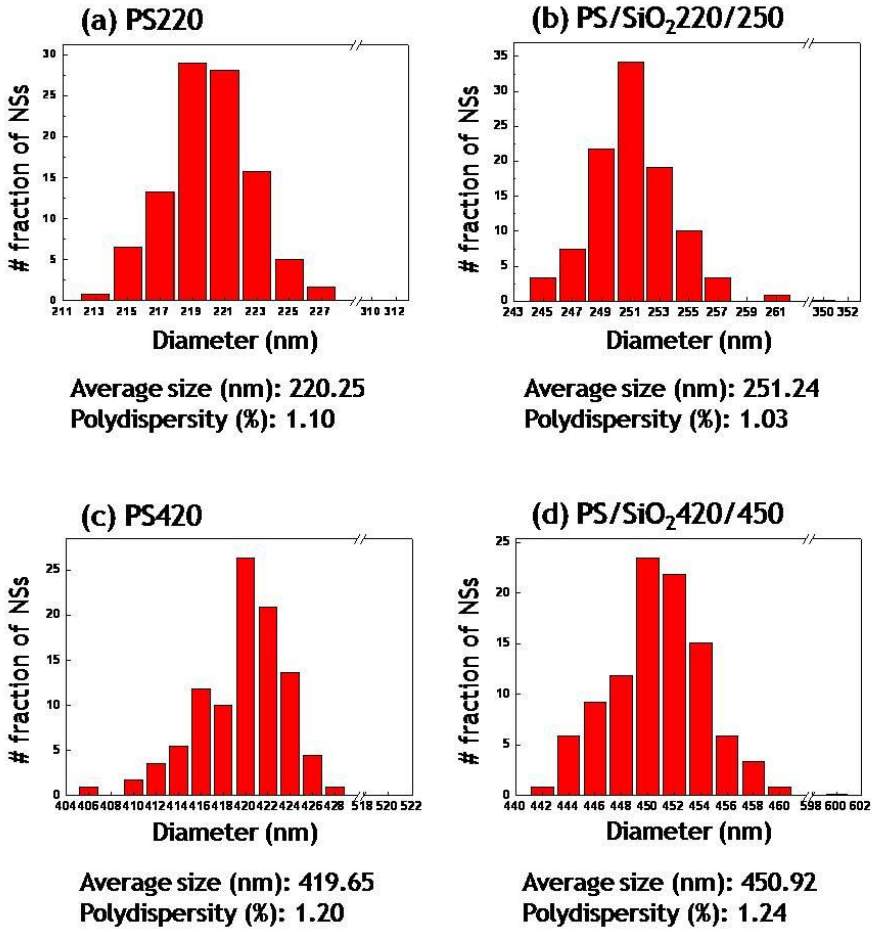

Figure 4. 5. Size distribution of (a) PS220, (b) PS/$SiO_2$220/250, (c) PS420, and (d) PS/$SiO_2$420/450. For PS#, # means a diameter (nm) of PS NS. For PS/SiO_2#$_1$/#$_2$, #$_1$ means a diameter (nm) of PS core and #$_2$ means an outer diameter (nm) of PS/SiO_2 NS.

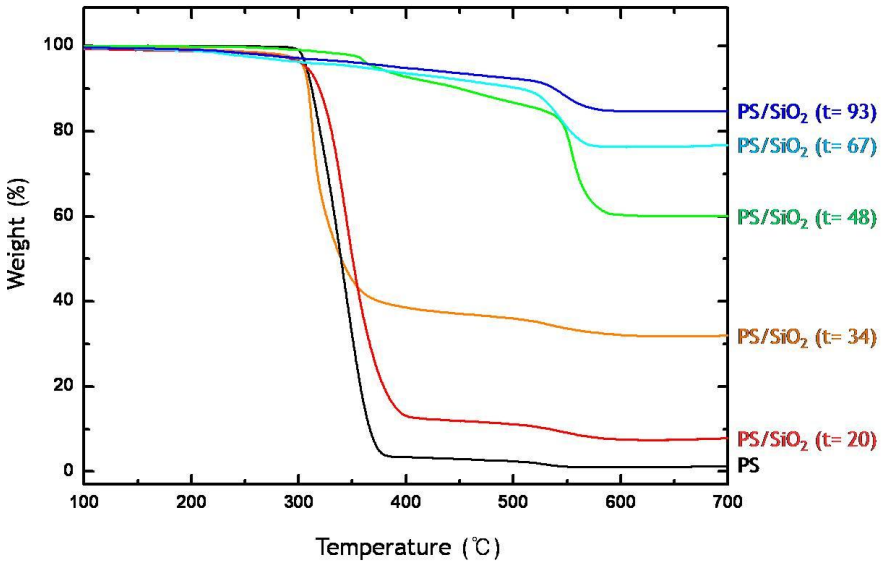

Figure 4. 6. TGA curves of PS NS and PS/SiO_2 NSs with different SiO_2 shell thickness (t: shell thickness (nm)).

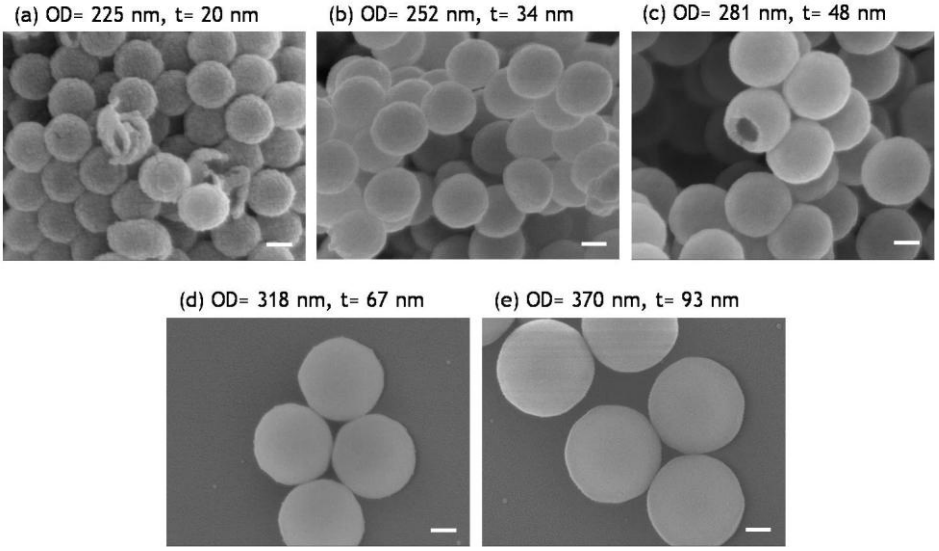

Figure 4. 7. FE-SEM images of hollow silica shells prepared with different SiO_2 shell thickness (core diameter: 185 nm, OD: outer diameter, t: shell thickness, scale bars: 100 nm).

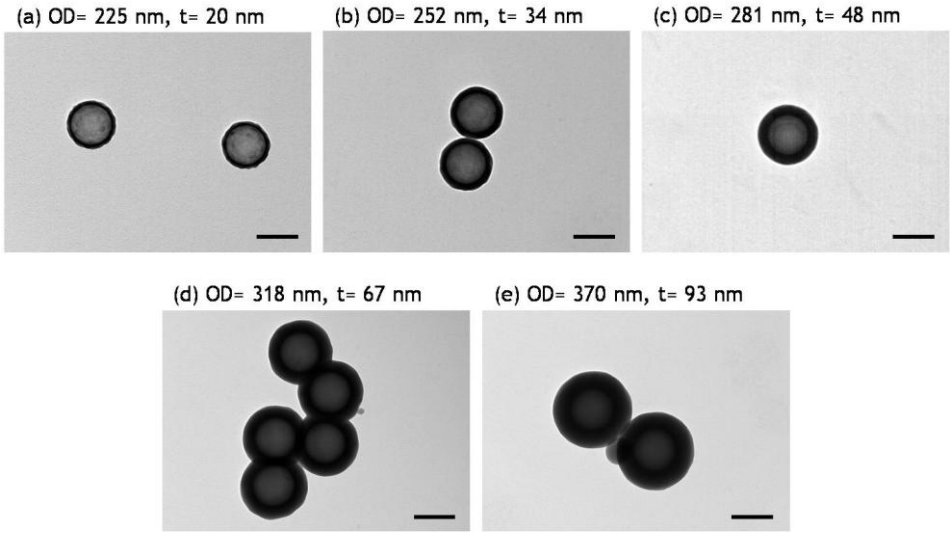

Figure 4. 8. TEM images of hollow silica shells prepared with different SiO_2 shell thickness (core diameter: 185 nm, OD: outer diameter, t: shell thickness, scale bars: 200 nm).

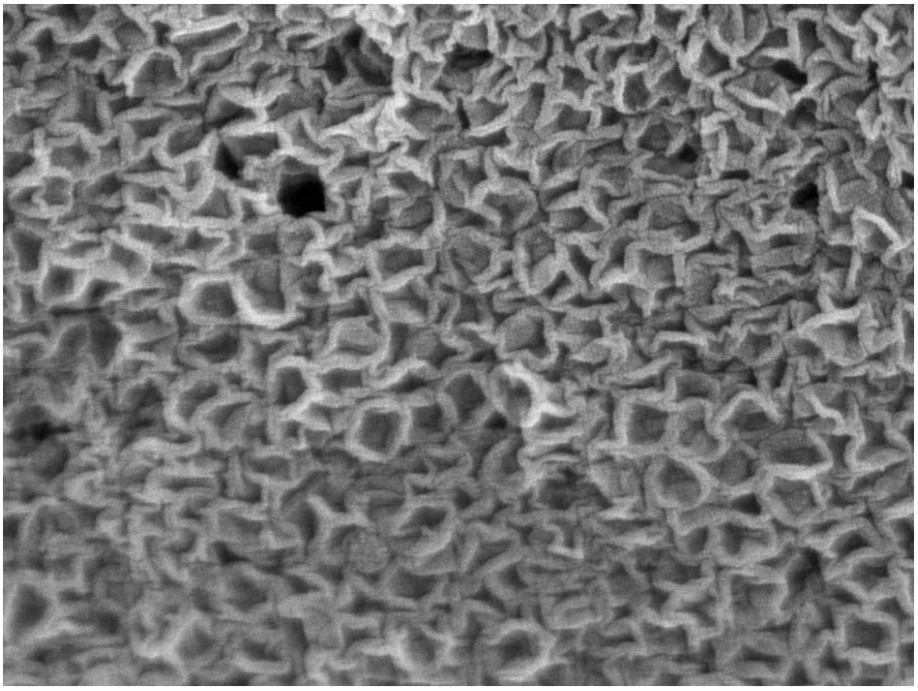

Figure 4. 9. FE-SEM image of deflated beach ball shaped structure of HSSs collapsed.

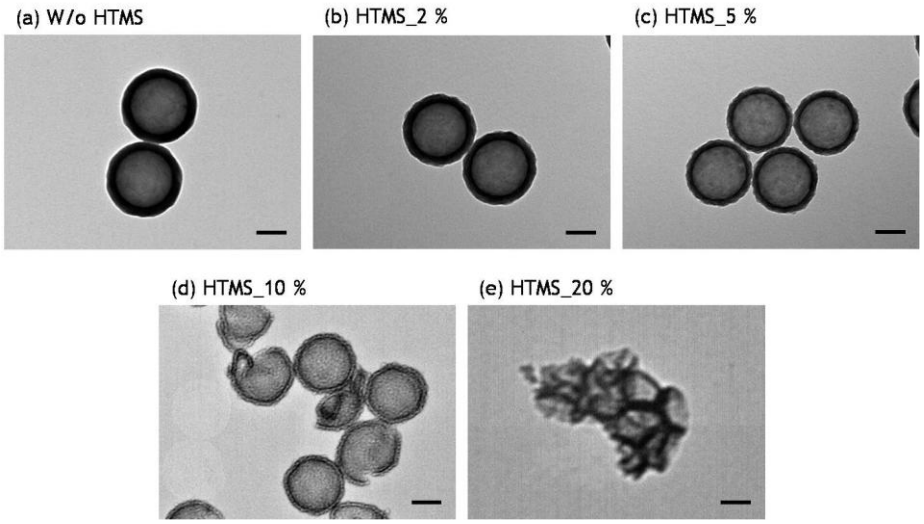

Figure 4. 10. TEM images of HSSs with different HTMS mixing ratio (scale bars: 100nm).

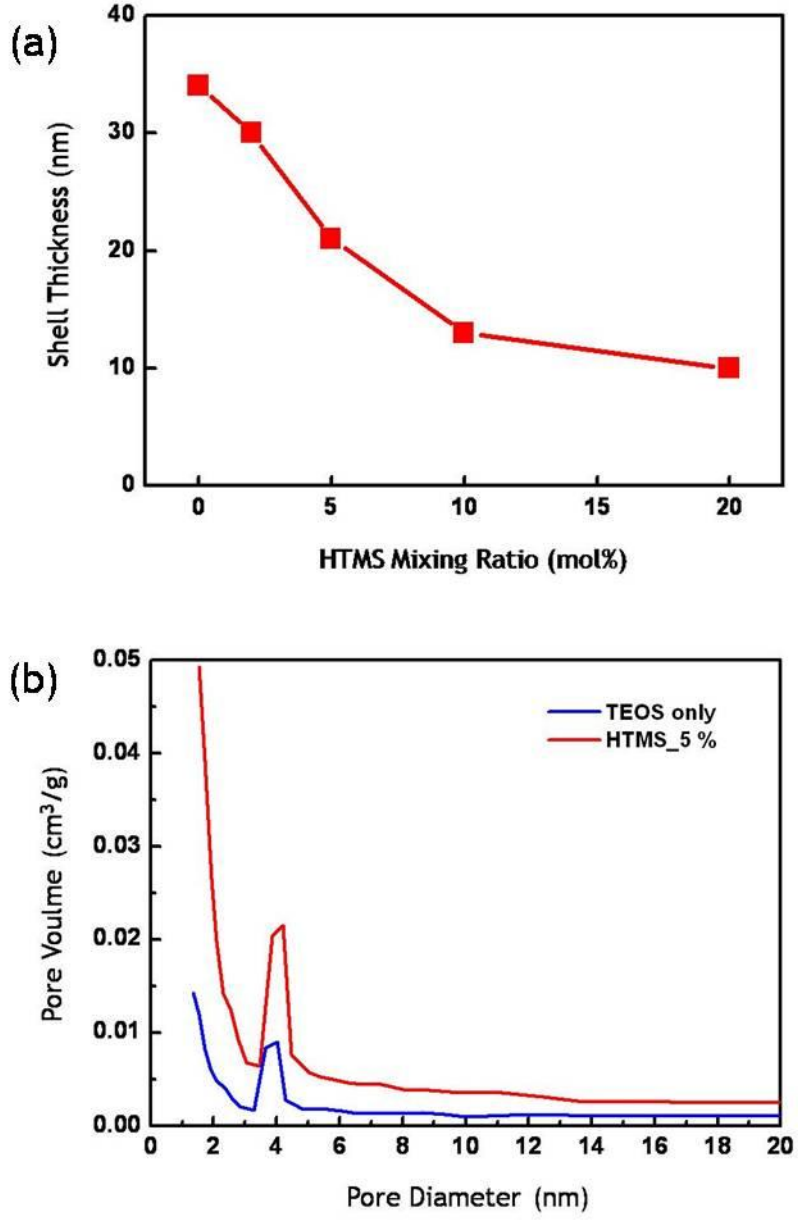

Figure 4. 11. (a) SiO_2 Shell thickness of HSSs with different HTMS mixing ratio. (b) Pore size and volume of HSS w/o HTMS and w/ 5 mol% of HTMS.

4. 3. 2. Preparation of Monolayered HSS Arrays Based on Electrostatic Interaction

To Form the monolayered PS/SiO_2 arrays on the sapphire substrates, the layer-by-layer deposition method based on electrostatic interaction was applied (see Figure 4. 12). The surface charge of sapphire substrates was first modified using polyelectrolytes. PAH, positively-charged polyelectrolyte, and PSS, negatively-charged polyelectrolyte, were alternately deposited on sapphire substrate. The surface charge of sapphire substrates was manipulated by control of sequence of PAH/PSS multilayered films. The positively-charged surface was obtained with PAH/PSS/PAH coated substrates, and negatively-charged surface was obtained with $(PAH/PSS)_2$ coated substrates.

To investigate the influence of surface charge on the morphology of PS/SiO_2 arrays, the PS/SiO_2 NSs were deposited on 3 different substrates, non-charged, positively-charged, and negatively-charged. In the cases of non-charged and negatively-charged substrates, the PS/SiO_2 arrays were not uniform and massive PS/SiO_2 aggregates were formed. On the other hand, the uniform and monolayered PS/SiO_2 arrays were formed with positively-charged substrates (see Figure 4. 13). This trend in the morphology change is related to the fact that the PS/SiO_2 NSs have negatively-charged surface. While the negatively-charged PS/SiO_2 NSs could be effectively bound on positively-charged substrates, the PS/SiO_2 NSs were mobile and reoriented by external force such as capillary force with non-charged & negatively-charged substrates.

The surface coverage of PS/SiO_2 NSs on sapphire substrates was controlled according to the dipping time (see Figure 4. 14). The monolayered PS/SiO_2 arrays were also prepared with different-sized PS/SiO_2 NSs (see Figure 4. 15). PS/SiO_2 NSs with 250, 355, and 450 nm of outer diameter were coated based on dipping method. All the PS/SiO_2 NSs were uniformly deposited on substrates.

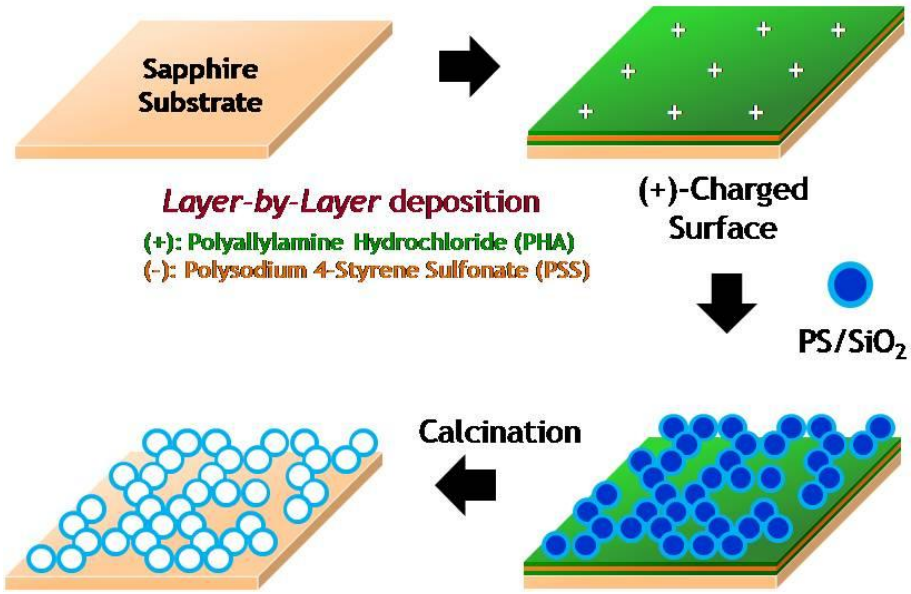

Figure 4. 12. A schematic on the preparation of HSS coated sapphire substrates.

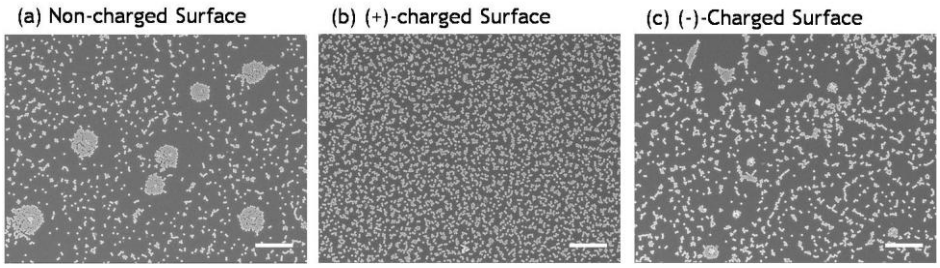

Figure 4. 13. HSS morphologies coated on (a) non-charged, (b) (+)-charged, and (c) (-)-charged surface (size of HSSs: 230 nm, scale bars: 5 μm).

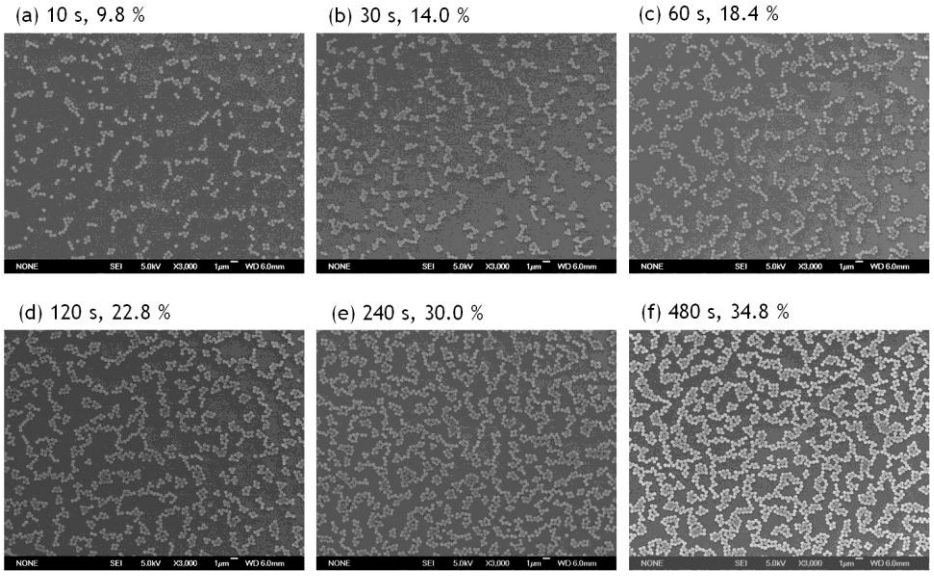

Figure 4. 14. Morphology of PS/SiO_2 monolayers prepared with (a) 10 s, (b) 30 s, (c) 60 s, (d) 120 s, (e) 240 s, and (f) 480 s of dipping time (outer diameter of HSS: 450 nm).

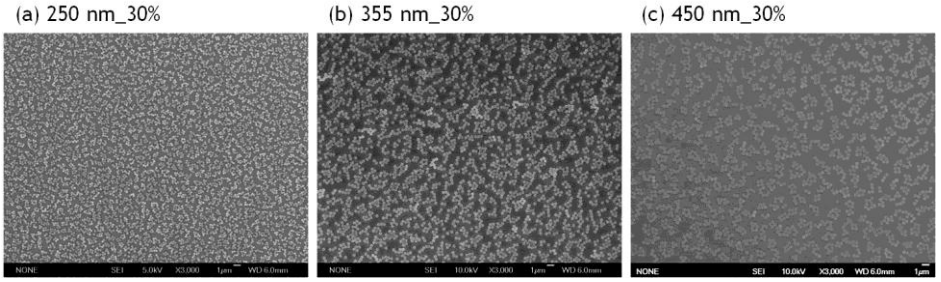

Figure 4. 15. Morphology of PS/SiO_2 monolayers prepared with (a) 250 nm-sized, (b) 355 nm-sized, and (c) 450 nm-sized PS/SiO_2 HNSs.

4. 3. 3. Growth of High Quality GaN Films Using HSS-Coated Sapphire Substrates

GaN films were grown on HSS-coated sapphire substrates using low pressure metal-organic chemical vapor deposition (MOCVD). The growth step of GaN films were presented in Figure 4. 16. 250 nm-sized HSSs coated sapphire substrates with 30 % of surface coverage were used. The surface of HSS-coated sapphire substrates was first cleaned by thermal treatment at 1100 ℃. The buffer GaN grains, seed GaN, were grown on HSS-coated sapphire substrates by low temperature growth at 500 ℃. After low temperature growth, high quality GaN films were grown on buffer GaN grain coated substrates by high temperature growth at 1080 ℃. According to the growth time of high temperature, the thickness of GaN films was controlled (see Figure 4. 17). In the early stage of GaN film growth, we confirmed the ELO of GaN films.

The bending of dislocations was observed by cross-sectional HR-TEM (see Figure 4. 18). The morphology of dislocations in GaN film grown on HSS-coated sapphire substrate was compared with reference sample, GaN film grown on bare sapphire substrate. While the dislocations within reference sample have grown in a straight line, the dislocations within HSS-coated samples have bended according to the surface of HSSs.[23] The dislocations on GaN film surface were directly observed by cathodoluminescence (CL) measurement (see Figure 4. 19(a), (b)).[24] The dislocations appeared as black dots in CL images and the dislocation density could be calculated by counting

the # of black dot. In HSS-coated sample, the dislocation density was far less than reference sample. The GaN films were grown with different growth pressure and the dislocation density of GaN films were characterized as a function of growth pressure (see Figure 4. 19(c)). The dislocation density was decreased as the growth pressure was increased regardless of sample type. It means that high quality GaN films were grown under high growth pressure.

The crystallinity of GaN films were characterized by X-ray diffraction (XRD) measurement.[25] The XRD curves of GaN films were measured according to 2 different lattice plane, (002) and (102) (see Figure 4. 20(a), (b)). In (102) plane, the FWHM of the HSS-coated samples was decreased considerably compared with reference sample. However, in (002) plane, the FWHM of HSS-coated samples were slightly higher than reference sample's. It means the crystallinity of HSS-samples are lower than reference sample in (002) plane. This is why there are three types of dislocations and each dislocation influences on the crystallinity of GaN films in different.[26] The (002) plane is influenced by screw and mixed dislocations, while the (102) plane is influenced by all the three types of dislocations including edge dislocation. In GaN film, the edge dislocation is dominant more than two third of total dislocations and edge dislocation can be easily bended by ELO. On the other hand, screw and mixed dislocations are rarely bended by ELO. Consequently, the HSSs influenced on the crystallinity of (102) plane, but rearly influenced on (002) plane. In addition, we assume that crysallinity of (002) plane is decreased by dopping of Si atom from HSSs to GaN film. As a result, the FWHM of (102) plane is decreased and the FWHM of (002) plane

is increased. The crystallinity of GaN films were characterized as a function of growth pressure (see Figure 4. 20(c)). In the case of the (102) plane, the FWHM of XRD curves was decreased as the growth pressure was increased regardless of sample type. It means that the crystallinity of GaN films on (102) plane was increased as the growth pressure as increased. On the other hand, the FWHM of XRD curves was slightly increased as the growth pressure was increased on (002) plane.

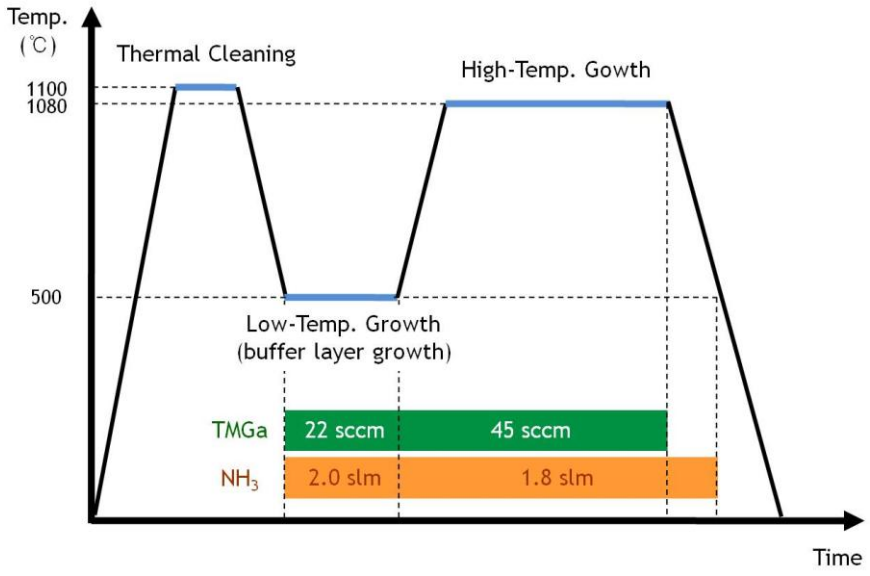

Figure 4. 16. Growth step of GaN films.

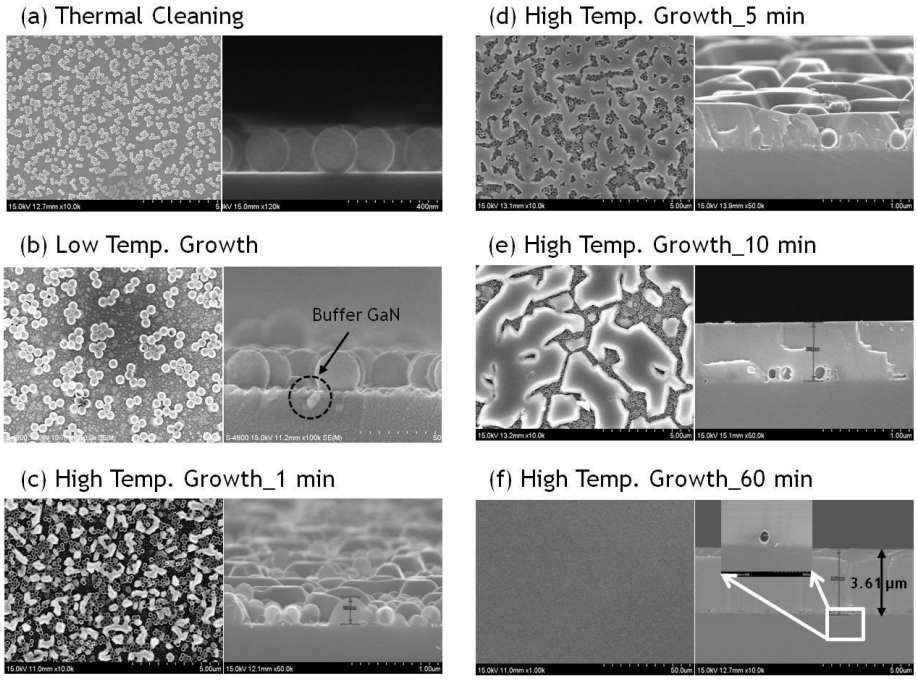

Figure 4. 17. Morphology of (a) HSS-coated sapphire substrate after thermal cleaning, (b) buffer GaN after low temperature growth, and GaN films grown after (c) 1 min, (d) 5 min, (e) 10 min, and (f) 60 min of high temperature growth.

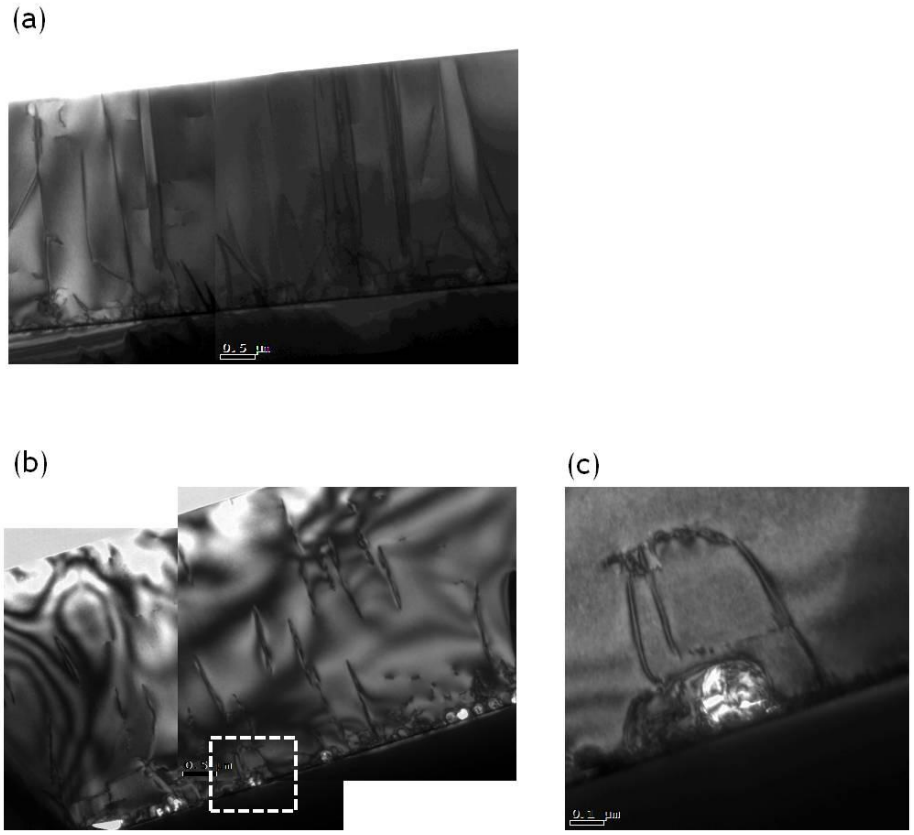

Figure 4. 18. Cross-sectional HR-TEM images of (a) reference GaN film, (b) GaN film grown on HSS-coated sapphire substrate, and (c) magnified image of HSS-coated sample.

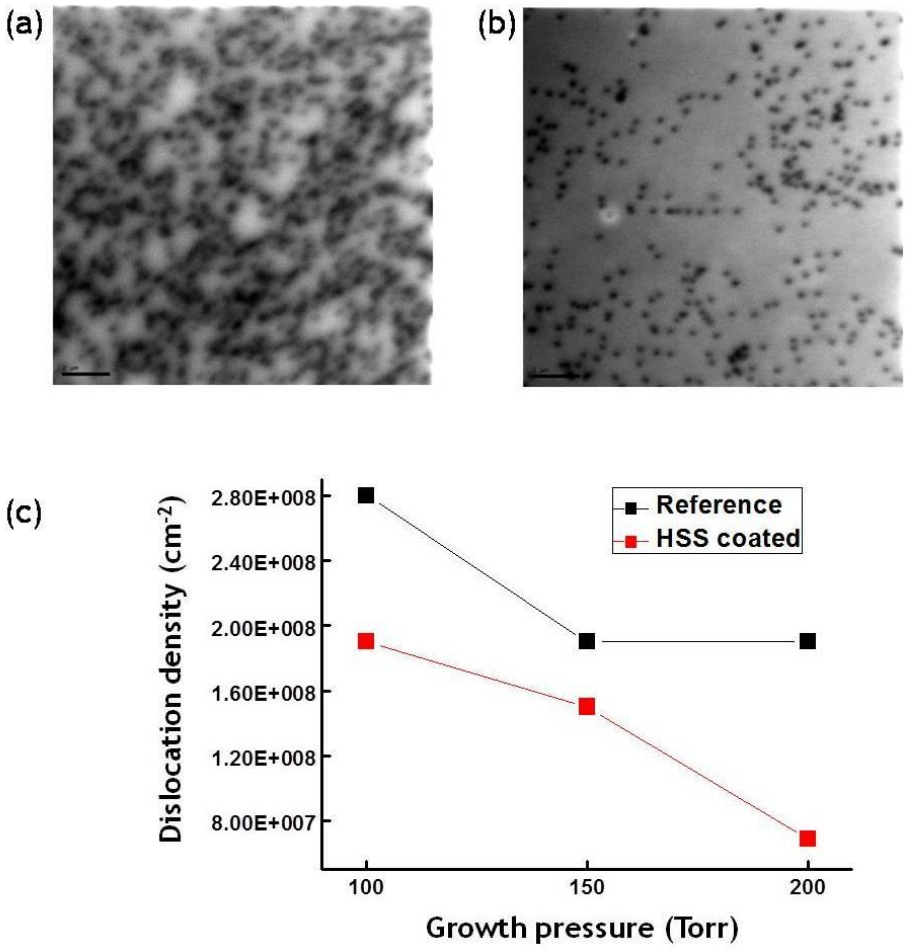

Figure 4. 19. CL images of of (a) reference GaN film and (b) GaN film grown on HSS-coated sapphire substrate. (c) Dislocation density of GaN films as a function of growth pressure.

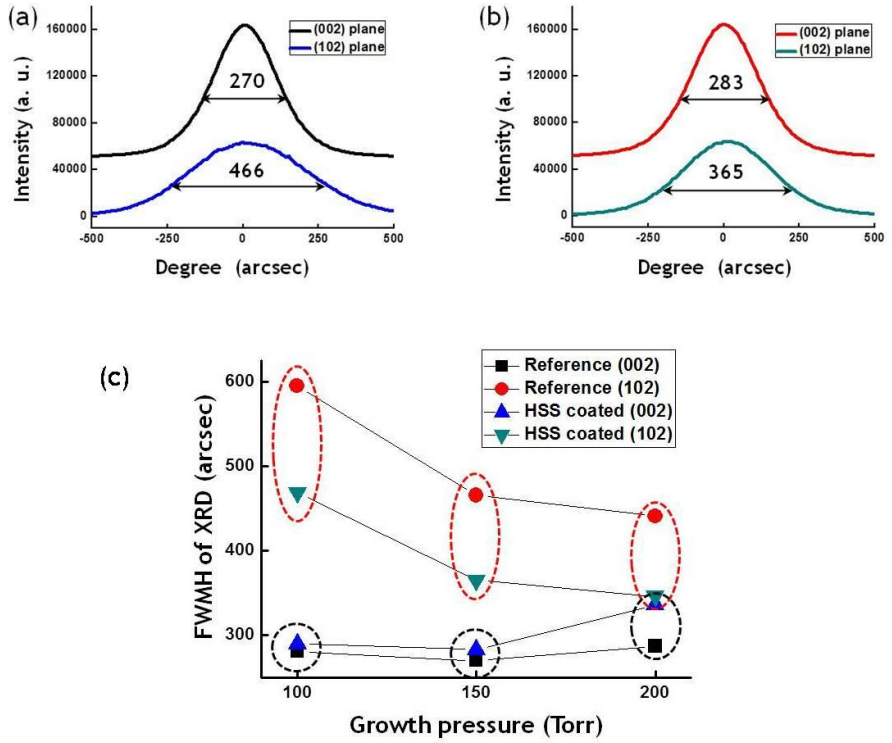

Figure 4. 20. XRD curves of (a) reference GaN film and (b) GaN film grown on HSS-coated sapphire substrate. (c) FWHM of XRD of GaN films as a function of growth pressure.

4. 3. 4. Preparation of LEDs Using GaN Films Grown onto HSS-Coated Sapphire Substrates and Characterization of Device Performance

The blue GaN LEDs were fabricated using multilayered GaN films. The buffer GaN, undoped GaN, layer was first grown on substrates and n-doped GaN, MQW, p-doped GaN, ITO electrod, and metal pads were deposited in order (see Figure 4. 21). The photoluminescence (PL) emission of GaN LEDs was mapped in 2D plane (see Figure 4. 22(a)). In the mapping images, the bluish area indicates low intensity region and the reddish area indicates high intensity region. In the case of the reference LED, whole area was covered with bluish region even the highest intensity region. On the other hand, In the case of HSS-coated LED, yellow and green regions were appeared from the edge of the area and reddish region was widely discovered at central region. The maximum PL intensity of HSS-coated LED was about three times more than reference LED's.

The electroluminescence (EL) emission of GaN LEDs was characterized. (see Figure 4. 22(b)). The EL curves were measured as a function of current. In the both case, the EL intensity of GaN LEDs were gradually increased as the current was increased. However, the maximum EL intensity of HSS-coated LED was far higher than reference LED's. The maximum EL intensity of HSS-coated LED with 20 mA of current was about three times more than reference LED's. The output power and I-V curves of GaN LEDs were also characterized (see Figure 4. 23). The output power of HSS-coated LED was increased about 80 % when compared with output power of reference LED. In

addition, the operation voltage of HSS-coated LED was slightly increased when compared with reference LED.

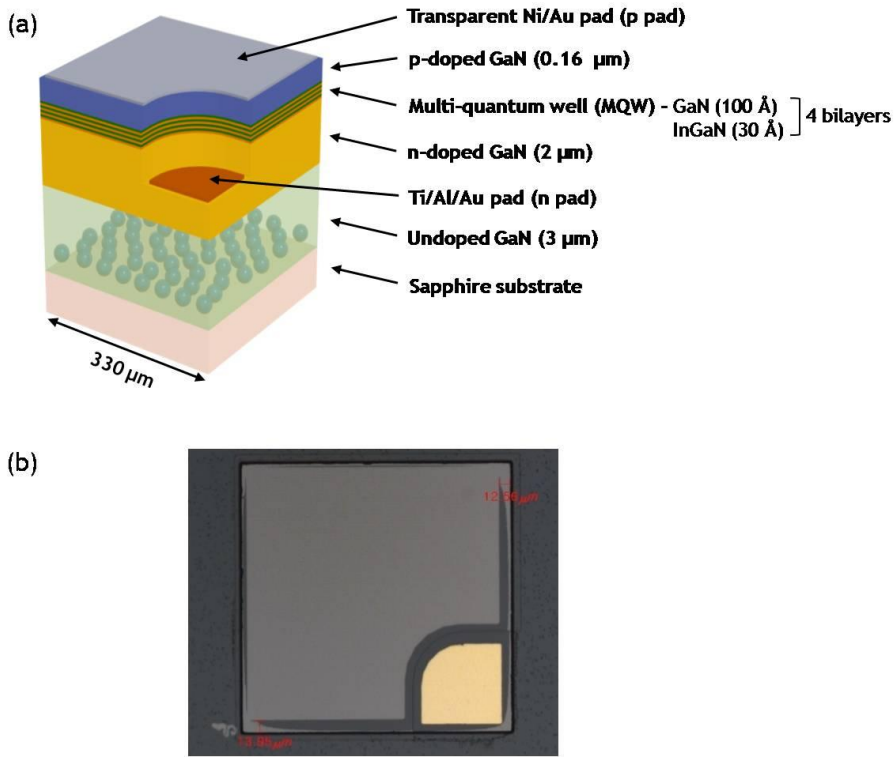

Figure 4. 21. (a) Device structure and (b) photograph of GaN-based LEDs.

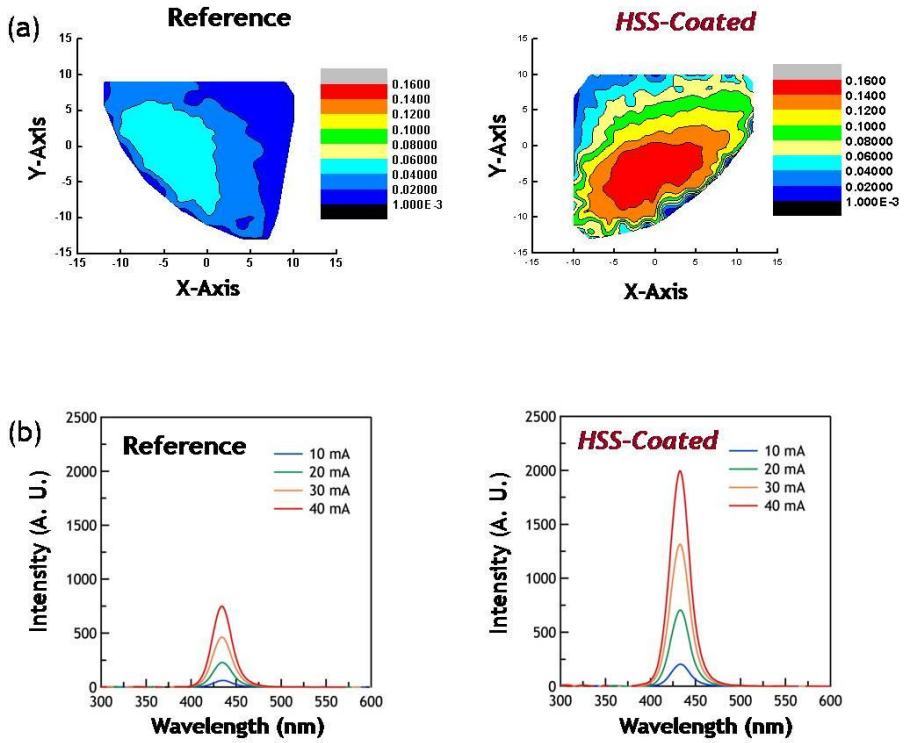

Figure 4. 22. (a) Mapping images of PL intensity and (b) EL curves of LEDs based on reference GaN film and GaN film grown on HSS-coated sapphire substrate.

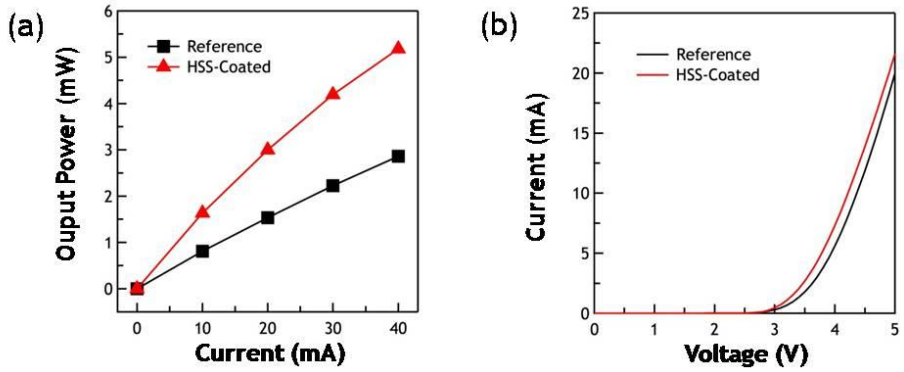

Figure 4. 23. (a) Output power and (b) I-V curves of reference GaN film and GaN film grown on HSS-coated sapphire substrate.

4. 4. Conclusion

Bowing-free and high quality GaN films were prepared using hollow silica shell (HSS)-coated sapphire substrates. HSSs were readily prepared by sol-gel reaction and HSS monolayers were uniformly deposited on large-aread sapphire substrates based on simple solution process. During the GaN film growth, ELO of GaN films were induced by HSSs located on sapphire substrates. GaN films grown on HSS-coated sapphire substrates showed decreased dislocation density and improved crystallinity. In addition, wafer bowing problem was effectively relieved and the compressive stress in GaN films were relaxed by the deformation of HSS and wafer bowing problem on GaN films were relieved. With these advantages, bowing-free and highly efficient GaN LEDs were prepared.

4. 5. References

(1) Nakamura, S.; Mukai, T.; Senoh, M. *Appl. Phys. Lett.* **1994**, *64*, 1687.

(2) Waltereit, P.; Brandt, O.; Trampert, A.; Grahn, H. T.; Menniger, J.; Ramsteiner, M.; Reiche, M.; Ploog, K. H. *Nature* **2000**, *406*, 865.

(3) Ling, S.-C.; Wang, T.-C.; Ko, T.-S.; Lu, T.-C.; Kuo, H.-C.; Wang, S.-C. *J. Cryst. Growth* **2008**, *301*, 2330.

(4) Huang, Y.; Sun, K. W.; Fischer, A. M.; Wei, Q. Y.; Juday, R.; Ponce, F. A.; Kato, R.; Yokogawa, T. *Appl. Phys. Lett.* **2011**, *98*, 261914.

(5) Barchuk, M.; Holý, V.; Milievi ć, B.; Krause, B.; Baumbach, T.; Hertkorn, J.; Scholz, F. *J. Appl. Phys.* **2010**, *108*, 043521.

(6) Youk, Y.; Kim, D. Y. *Opt. Commun.* **2006**, *262*, 206.

(7) Ueda, K.; Tsuchida, Y.; Hagura, N.; Iskandar, F.; Okuyama, K.; Endo, Y. *Appl. Phys. Lett.* **2008**, *92*, 101101.

(8) Lin, C. H.; Kuo, H. C.; Lai, C. F.; Huang, H. W.; Leung, K. M.; Yu, C. C.; Lo, J. R. *Semicond. Sci. Tech.* **2006**, *21*, 1513.

(9) Kim, J. K.; Luo, H.; Xi, Y.; Shah, J. M.; Gessmann, T.; Schubert, E. F. *J. Electrochem. Soc.* **2006**, *153*, G105.

(10) Lee, Y. J.; Lu, T. C.; Kuo, H. C.; Wang, S. C.; Liou, M. J.; Chang, C. W.; Hsu, T. C.; Hsieh, M. H.; Jou, M. J.; Lee, B. J. *Jpn. J. Appl. Phys.* **2006**, *45*, 643.

(11) Sakai, A.; Sunakawa, H.; Usui, A. *Appl. Phys. Lett.* **1997**, *71*, 2259.

(12) Parish, G.; Keller, S.; Kozodoy, P.; Ibbetson, J. P.; Marchand, H.; Fini, P. T.; Fleischer, S. B.; DenBaars, S. P.; Mishra, U. K. *Appl. Phys. Lett.* **1999**, *75*,

247.

(13) Nam, O.-H.; Bremser, M. D.; Zheleva, T. S.; Davis, R. F. *Appl. Phys. Lett.* **1997**, *71*, 2638.

(14) Chiu, C. H.; Yen, H. H.; Chao, C. L.; Li, Z. Y.; Yu, P.; Kuo, H. C.; Lu, T. C.; Wang, S. C.; Lau, K. M.; Cheng, S. J. *Appl. Phys. Lett.* **2008**, *93*, 081108.

(15) Oh, T. S.; Kim, S. H.; Kim, T. K.; Lee, Y. S.; Jeong, H.; Yang, G. M.; Suh, E.-K. *Jpn. J. Appl. Phys.* **2008**, *47*, 5333.

(16) Frajtag, P.; El-Masry, N. A.; Nepal, N.; Bedair, M. *Appl. Phys. Lett.* **2011**, *98*, 023115.

(17) Lai, W.-C.; Yang, Y.-Y.; Peng, L-C.; Yang, S.-W.; Lin, Y.-R.; Sheu, J.-K. *Appl. Phys. Lett.* **2010**, *97*, 081103.

(18) Li, Q.; Lin, Y.; Creighton, J. R.; Figiel, J. J.; Wang, G. T. *Adv. Mater.* **2009**, *21*, 2416.

(19) An, S. J.; Hong, Y. J.; Yi, G.-C.; Kim, Y.-J.; Lee, D. K. *Adv. Mater.* **2006**, *18*, 2833.

(20) Li, Q.; Figiel, J. J.; Wang, G. T. *Appl. Phys. Lett.* **2009**, *94*, 231105.

(21) Zhang, L.; D'Acunzi, M.; Kappl, M.; Auernhammer, G. K.; Vollmer, D. *Langmuir* **2009**, 25, 2711.

(22) Song, X.; Gao, L. *J. Phys. Chem. C* **2007**, *111*, 8180.

(23) Gradečak, S.; Stadelmann, P.; Wagner, V.; Ilegems, M. *Appl. Phys. Lett.* **2004**, *85*, 4648.

(24) Bastek, B.; Bertram, F.; Christen, J.; Wernicke, T.; Weyers, M.; Kneissl, M. *Appl. Phys. Lett.* **2008**, *92*, 212111.

(25) Heying, B.; Wu, X. H.; Keller, S.; Li, Y.; Kapolnek, D.; Keller, B. P.;

DenBaars, S. P.; Speck, J. S. *Appl. Phys. Lett.* **1996**, *68*, 643.

(26) Elsner, J.; Jones, R.; Sitch, P. K.; Porezag, V. D.; Elstner, M.; Frauenheim, Th.; Heggie, M. I., Ö berg, S.; Briddon, P. R. *Phys. Rev. Lett.* **1997**, *79*, 3672.

Chapter 5. Ag/ SiO_2 Hybrid Hollow Shells with Improved Reflectivity and Light Absorption Property

5. 1. Introduction

Silver nanoparticles (Ag NPs) have attracted intensive attention due to their excellent material properties such as surface plasmon resonance,[1,2] high reflectivity,[3-5] antibacterial nature,[6,7] catalysis,[8] and high electric conductivity.[9] Recently, many research groups have reported various synthetic routes for Ag NPs[10] and functional hybrid materials based on Ag NPs.[11-14] Ag NP containing spheres for catalytic applications[8], Ag NP sensors,[15,16] and reflective layers based on Ag NPs were prepared. In the field of analytic applications, Ag NPs have been thoroughly studied for surface enhanced Raman scattering (SERS).[1,2]

Herein, we prepared Ag NP/ SiO_2 hybrid hollow shells (Ag/SiO_2 HHSs) with improved reflectivity and light absorption property. Ag NPs were directly grown on the PVP-coated PS NS surface and SiO_2 shells were coated onto the Ag NP-decorated PS NS surface (see Figure 5. 1). The size and # density of Ag NPs grown on PS NS surface were tunable by varying the synthetic condition. Ag/SiO_2 HHSs prepared presented distinguished optical properties. Ag/SiO_2 HHSs showed enhanced reflectivity when compared with HSS

without Ag NPs due to the high reflectivity of Ag NPs. Furthermore, the light absorbance of Ag NPs within Ag/SiO_2 HHSs was remarkably increased when compared with pristine Ag NPs by the light trapping effect of hollow inner space within Ag/SiO_2 HHSs.

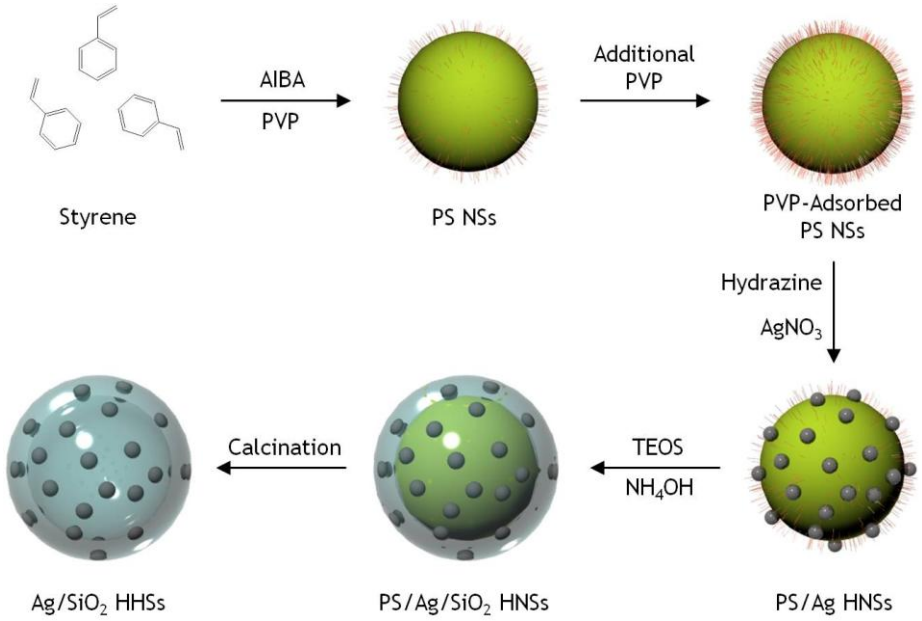

Figure 5. 1. Schematic illustration for the preparation of Ag/SiO_2 HHSs.

5. 2. Experimental Details

5. 2. 1. Chemicals

Styrene (99 %), 2,2-azobis-(isobutyramidine) dihydrochloride (AIBA, 97 %), polyvinylpyrrolidone (PVP, Mw= 10K, 55K, and 360K), tetraethyl orthosilicate (TEOS, 98 %), ammonium hydroxide solution (aq, 28-30 %), $AgNO_3$ (99 %), hydrazine hydrate ($N_2H_4 \cdot xH2O$, N_2H_4 ~ 50-60%), polyallylamine hydrochloride (PAH, Mw= 70K), and polysodium 4-styrene sulfonate (PSS, Mw= 70K) were used as purchased from Aldrich.

5. 2. 2. Synthesis of PS/Ag/SiO_2 Hybrid Nanospheres

Positively charged polystyrene nanospheres (PS NSs) with 420 nm of diameter were first synthesized using styrene as a monomer, AIBA as an initiator as well as the surfactant, and PVP (55K) as a stabilizer and a cosurfactant by dispersion polymerization. To improve the direct reduction of Ag on the PS NS surface, additional PVP was adsorbed on PS NS surface. 0.5 ml of PS dispersion (3.85 wt% in EtOH), 0.25 ml of hydrazine hydrate solution (2 mg/ml in H_2O), and 0.25 ml of $AgNO_3$ solution (60 mg/ml in H_2O) were injected into the EtOH/H_2O mixture in order (PS NS : $AgNO_3$: N_2H_4 = 1 : 1 : 1/30 in wt ratio). The total volume of mixture was fixed at 10 ml. The mixture was stirred at room temperature for 12 h. Synthesized PS/Ag hybrid nanospheres (PS/Ag HNSs) were purified repeatedly using EtOH and distilled water by precipitation/redispersion methods to remove or unreacted reactants. To induce the effective SiO_2 shell formation on the PS/Ag HNS surface,

additional PVP (360K) was adsorbed on PS/Ag HNS surface. PVP-adsorbed PS/Ag HNSs were dispersed in 20 ml of EtOH and stirred using magnetic stirring bar. 1 ml of ammonium hydroxide was injected in PS/Ag dispersion. 0.1 ml of TEOS was then added to the mixture dropwise for 1 h while maintaining vigorous stirring at room temperature. After the injection of TEOS and 1h of further reaction, PS/Ag/SiO_2 HNSs prepared were purified repeatedly using EtOH and distilled water.

5. 2. 3. Deposition of Ag/SiO_2 Monolayers on Positively-Charged Substrates

The substrates (sapphire or quartz) were first cleaned by piranha treatment (H_2SO_4 : H_2O_2 = 7 : 3 in volume ratio). To make negatively-charged surface, piranha treated substrates were placed in RCA solution (H_2O : ammonium hydroxide : H_2O_2 = 5 : 1 : 1 in volume ratio) at 50 ℃ for 3 minute. After RCA treatment, PAH, positively-charged polyelectrolyte, in H_2O (1 mg/ml) was deposited on the substrates by spin casting. PSS, negatively-charged polyelectrolyte, in H_2O (1 mg/ml) was then deposited on the PAH-coated substrates by spin casting. And PAH deposition was repeated on PAH/PSS-coated substrates. In every deposition step, the residual, not adsorbed, polyelectrolyte on the substrates was removed using distilled water (2 times). To prepare Ag/SiO_2 monolayer coated substrates, the PAH/PSS/PAH multilayered thin film-coated substrates were dipped in PS/Ag/SiO_2 HNSs dispersion with different PS/Ag/SiO_2 concentration and dipping time. The residual, not adsorbed, PS/Ag/SiO_2 on the substrates was removed by washing

with distilled water (3 times). The PS/Ag/SiO_2 coated substrates were calcinated under N_2 flow at 700 ℃ for 1 h to remove the PS core within PS/Ag/SiO_2 HNS and the polyelectrolyte multilayered thin films on the substrates.

5. 2. 4. Characterizations

The morphology of Ag/SiO_2 HHSs was obtained by energy-filtered transmission electron microscope (EF-TEM; LIBRA 120, Carl Zeiss) and the Ag/SiO_2 arrays were characterized by a Field-Emission Scanning Electron Microscope (FE-SEM; JSM 6071F, JEOL). The transmittance and reflectance of Ag/SiO_2 coated substrates was measured with a UV-Vis-NIR spectrometer combined with an integrating sphere detector (Cary Series UV-Vis-NIR Spectrometer, Agilent Technologies).

5. 3. Results and Discussion

5. 3. 1. Preparation and Characterization of Ag/SiO_2 Hybrid Hollow Shells

The Ag NPs was synthesized on the surface of PVP-coated PS NSs by the direct reduction of Ag ions.[17-19] The mechanism of reduction of Ag ion on PVP was presented in Figure 5. 2. The size and the # density of Ag NPs were controlled by varying the solvent mixing ratio, the molecular weight of PVP, and the concentration of reactants.

$EtOH/H_2O$ mixture was used as a solvent for synthesis of Ag NPs. To investigate the influence of solvent mixing ratio on the size and the # density of Ag NPs, the mixing ratio of EtOH : H_2O was varied from 1 : 9 to 9 : 1 in volume ratio (see Figure 5. 3). The feed ratio of PS NS : $AgNO_3$: hydrazine was fixed at 1 : 1 : 1/30 in wt ratio. As the volume ratio of H_2O was increased, the average size of Ag NPs was increased and the # density of Ag NPs was decreased. On the other hand, As the volume ratio of EtOH was increased, the average size of Ag NPs was decreased and the # density of Ag NPs was increased. In addition, the uniformity of Ag NPs was decreased with higher EtOH mixing ratio. With 7 : 3 volume ratio of $EtOH/H_2O$ mixture, the reasonably uniform AgNPs with high # density were synthesized. Thus, the mixing ratio of EtOH : H_2O was fixed at 7 : 3 for further synthesis of Ag NPs.

To investigate the influence of molecular weight of PVP on size and # density of Ag NPs, Ag NPs were synthesized using PVP coated PS NSs with 3 differenent PVP molecular weight, 10K, 55K, and 360K (see Figure 5. 4). The

feed ratio of PS NS : $AgNO_3$: hydrazine was fixed at 1 : 1 : 1/30 in wt ratio. Ag NPs synthesized showed similar particle size and # density in all synthetic condition. However, Ag NPs with 10K of PVP showed slightly broad particle size distribution when compared other samples. Among the 3 types of samples, Ag NPs with 55K of PVP showed the highest # density and reasonable particle size & size distribution. Thus, the molecular weight of PVP was fixed at 55K for further synthesis of Ag NPs.

To determine the effect of reactant concentration on the size and # density of Ag NPs, we repeated the synthesis of Ag NPs with various concentrations of hydrazine and $AgNO_3$. First, hydrazine concentration was varied with fixed PS NS and $AgNO_3$ concentration (see Figure 5. 5). Ag NPs were synthesized with 0.125, 0.25, 0.375, and 0.5 ml of hydrazine hydrate solution (2 mg/ml in H_2O) while the amount of other reactants were fixed (0.5 ml of PS dispersion (3.85 wt% in EtOH), and 0.25 ml of $AgNO_3$ solution (60 mg/ml in H_2O)). The feed ratio of PS NS : $AgNO_3$: N_2H_4 was varied from 1 : 1 : *1/60* to 1 : 1 : *1/15* in wt ratio. As the concentration of hydrazine increased, the size and # density of Ag NPs also increased. However, Ag NPs with the highest hydrazine concentration showed decreased # density and large-sized particles with broad particle size distribution. In the case of 1 : 1 : *1/20* feed ratio, Ag NPs with the highest # density and reasonable particle size & size distribution were synthesized. Second, $AgNO_3$ concentration was varied with fixed PS NS and hydrazine concentration (see Figure 5. 6). Ag NPs were synthesized with 0.125, 0.25, 0.375, and 0.5 ml of $AgNO_3$ solution (60 mg/ml in H_2O) while the amount of other reactants were fixed (0.5 ml of PS dispersion (3.85 wt%

in EtOH), and 0.25 ml of hydrazine hydrate solution (2 mg/ml in H_2O)). The feed ratio of PS NS : $AgNO_3$: N_2H_4 was varied from 1 : *0.5* : 1/30 to 1 : *2* : 1/30 in wt ratio. As the concentration of $AgNO_3$ increased, the size and # density of Ag NPs also increased. However, Ag NPs with the highest $AgNO_3$ concentration showed large-sized particles with broad particle size distribution. In the case of 1 : *1.5* : 1/30 feed ratio, Ag NPs with the highest # density and reasonable particle size & size distribution were synthesized.

The PS/Ag/SiO_2 HNSs were synthesized using PVP-coated PS/Ag HNSs as templates, TEOS as a silica precursor, and ammonium hydroxide as a catalyst by sol-gel method. The silica shells were uniformly deposited on bumped surface of PS/Ag HNS due to the positive charge and the PVP adsorbed on PS/Ag HNS surface. The thickness of SiO_2 shells were almost constant about 15 nm regardless of size and # density of Ag NPs (see Figure 5. 7). The surface of PS NSs was negatively charged due to the residual silanol (Si-OH) groups on SiO_2 shells. To make Ag/SiO_2 HHSs, the PS cores within the PS/Ag/SiO_2 HNSs were removed by calcination. The PS/Ag/SiO_2 HNSs were heated using furnace under N_2 flow at 700 ℃ for 1 h. The weight loss of PS/SiO_2 NSs was monitored by TGA according to the themperature (see Figure 5. 8). The thermal decomposition of PS cores started around 350 ℃. The Ag/SiO_2 HHSs obtained showed same size & shape with corresponding PS/Ag/SiO_2 HNSs (see Figure 5. 9).

PS/Ag HNSs with different # density were prepared with fixed Ag NP size by repeated Ag reduction (see Figure 5. 10). 20 nm-sized Ag NPs were first synthesized on the PS NS surface and additional PVP was adsorbed on the

PS/Ag HNSs prepared for further Ag NP synthesis. With the PVP-adsorbed PS/Ag HNSs, same synthetic process of Ag NP was then repeated. The # density of Ag NPs within the PS/Ag HNSs was gradually increased as the synthetic procedure was repeated (see Figure 5. 11 and Table 5. 1). The average size and the # density of Ag NPs synthesized on PS surface were 16.1 nm and 18.5 each/NS at first reduction (PS/Ag20_#1). The # density of Ag NPs was linearly increased according to further reaction. The # density of Ag NPs of double (PS/Ag20_#2), triple (PS/Ag20_#3), and quadruple (PS/Ag20_#4) reaction was 48.3, 75.1, and 98.7 each/NS, respectively. On the other hand, the average size of Ag NPs was rarely increased according to further reaction. The average size of Ag NPs of double, triple, and quadruple reaction was 20.9, 23.5, and 24.3 each/NS, respectively. All the Ag NPs synthesized showed reasonably similar particle size.

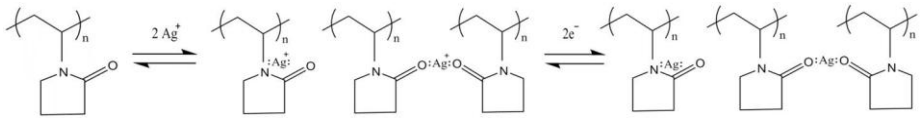

Figure 5. 2. Mechanism of Ag ion reduction on PVP.

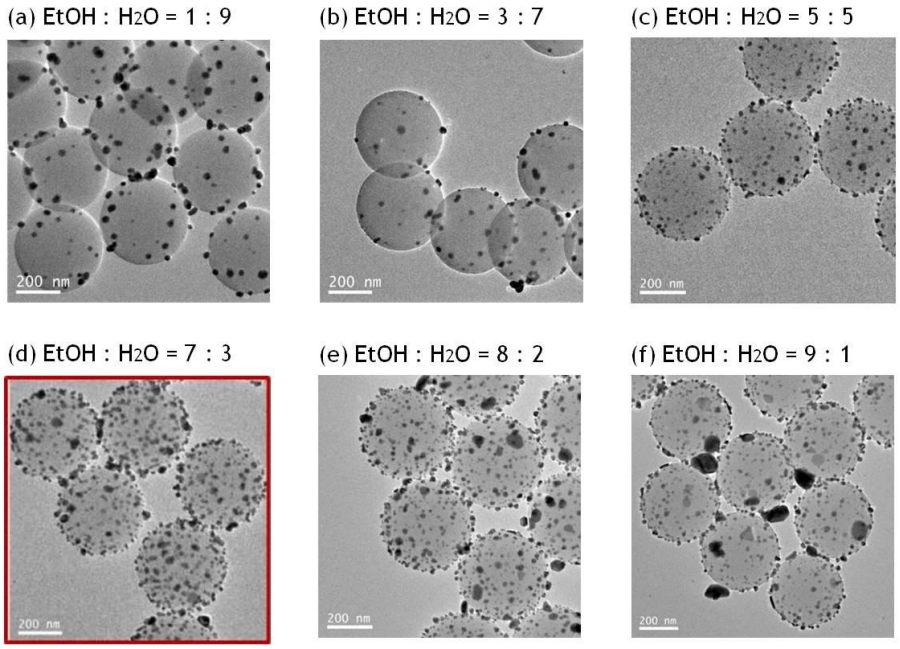

Figure 5. 3. TEM images of PS/Ag HNSs prepared with (a) 1 : 9, (b) 3 : 7, (c) 5 : 5, (d) 7 : 3, (e) 8 : 2, and (f) 9 : 1 of EtOH : H_2O mixing ratio.

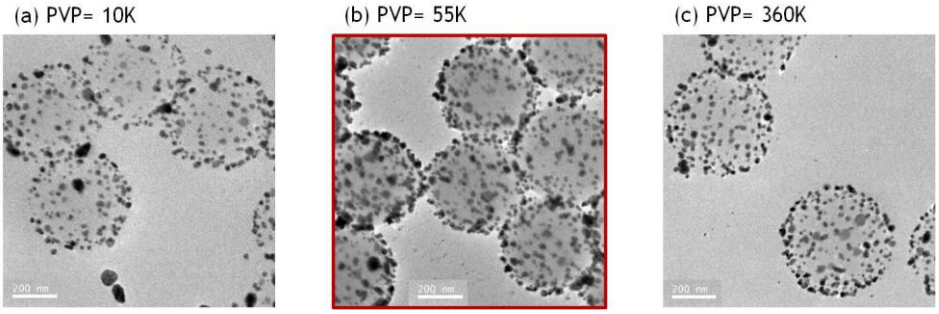

Figure 5. 4. TEM images of PS/Ag HNSs prepared with (a) 10K, (b) 55K, and (c) 360K of PVP.

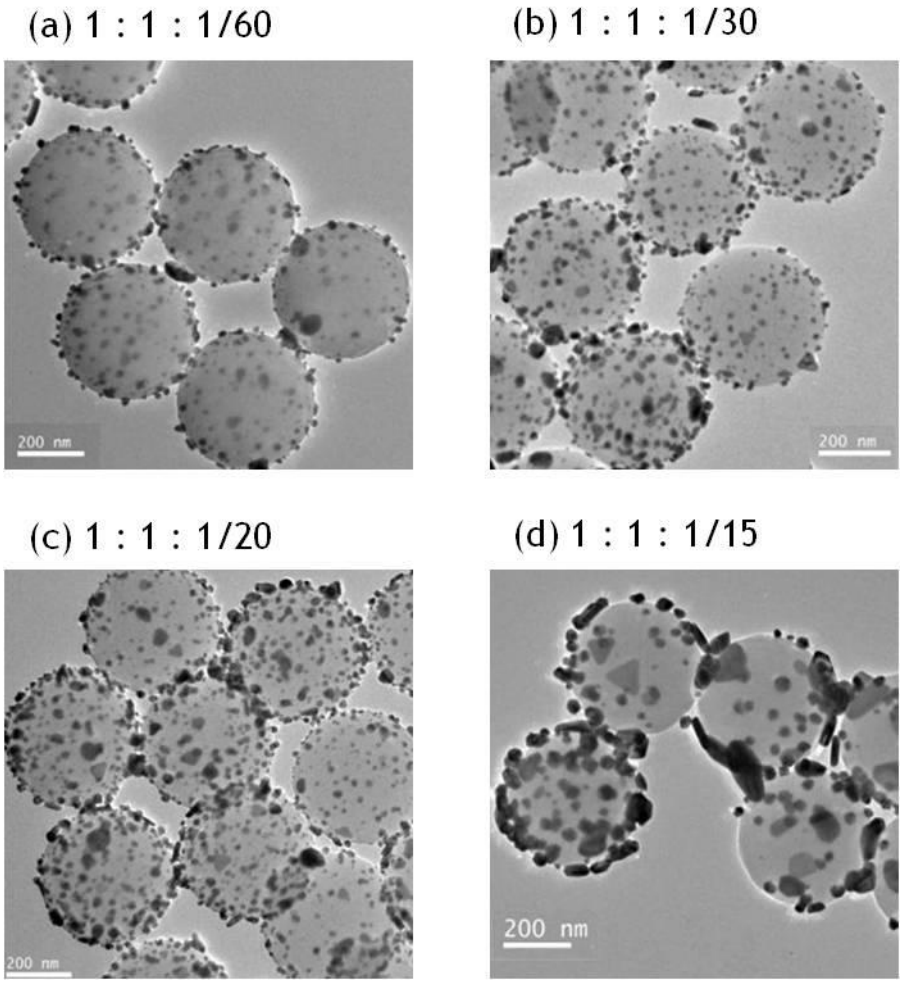

Figure 5. 5. TEM images of PS/Ag HNSs prepared with (a) 1 : 1 : 1/60, (b) 1 : 1 : 1/30, (c) 1 : 1 : 1/20, and (d) 1 : 1 : 1/15 of PS NS : $AgNO_3$: N_2H_4 feed ratio in weight.

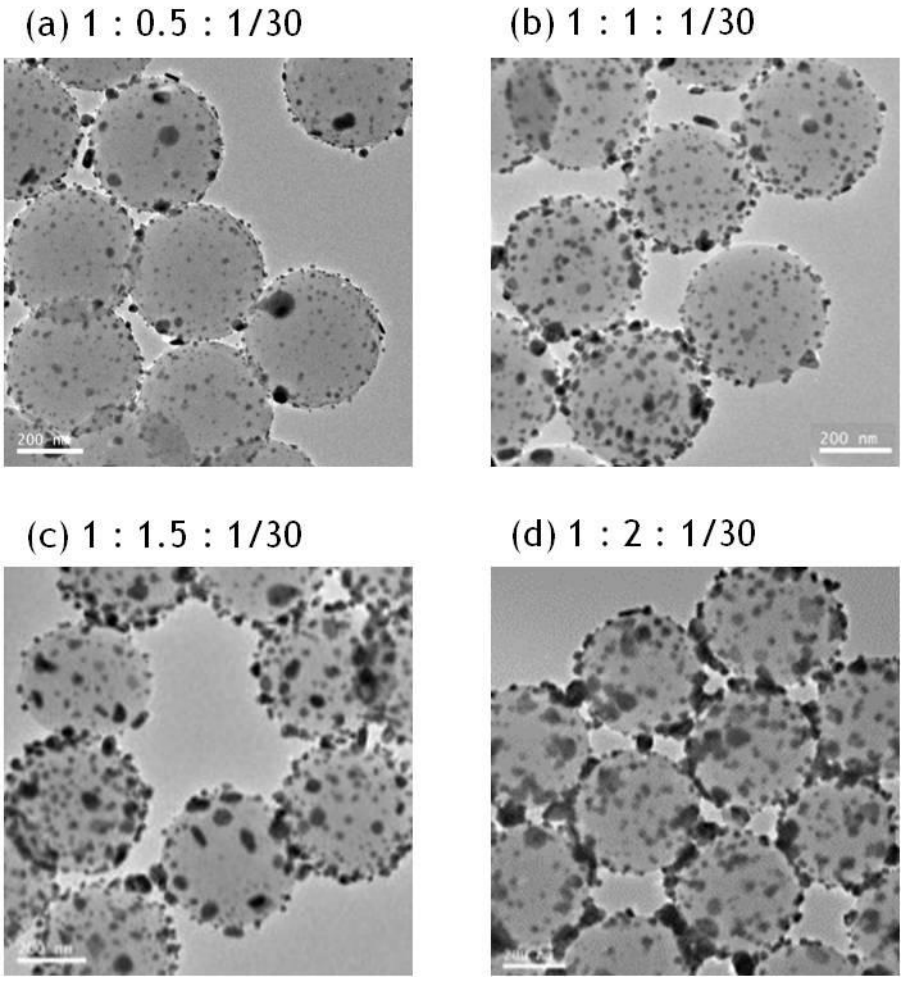

Figure 5. 6. TEM images of PS/Ag HNSs prepared with (a) 1 : 0.5 : 1/30, (b) 1 : 1 : 1/30, (c) 1 : 1.5 : 1/30, and (d) 1 : 2 : 1/30 of PS NS : $AgNO_3$: N_2H_4 feed ratio in weight.

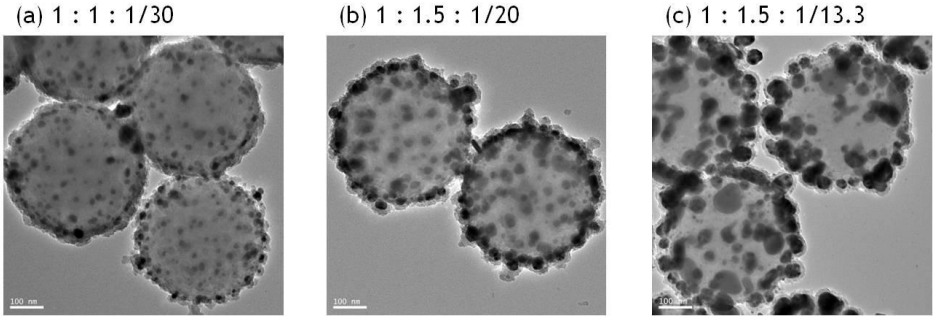

Figure 5. 7. TEM images of PS/Ag/SiO_2 HNSs prepared with (a) 1 : 1 : 1/30, (b) 1 : 1.5 : 1/20, and (c) 1 : 1.5 : 1/13.3 of PS NS : $AgNO_3$: N_2H_4 feed ratio in weight.

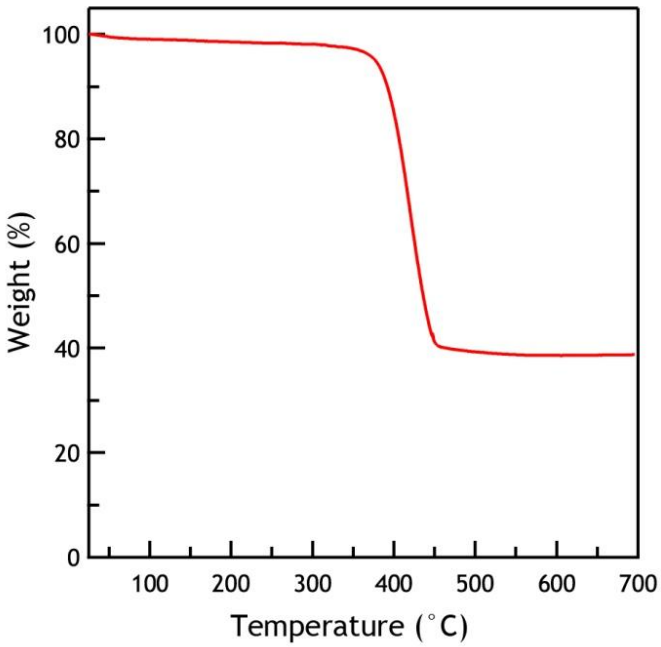

Figure 5. 8. TGA curve of PS/Ag/SiO_2 HNS.

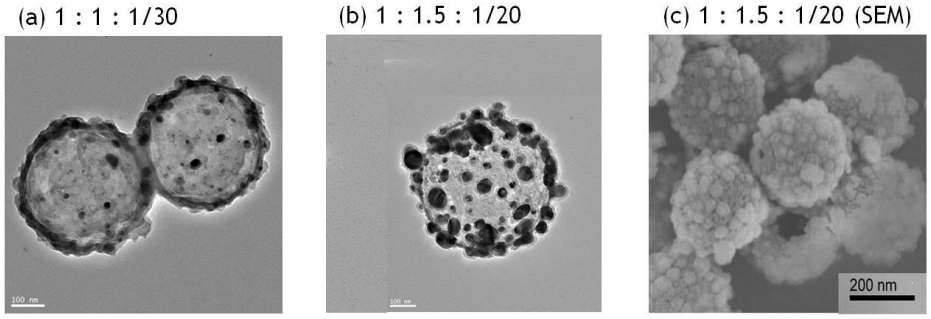

Figure 5. 9. TEM images of Ag/SiO_2 HHSs prepared with (a) 1 : 1 : 1/30 and (b) TEM and (c) FE-SEM images of Ag/SiO_2 HHSs prepared with 1 : 1.5 : 1/20 of PS NS : $AgNO_3$: N_2H_4 feed ratio in weight.

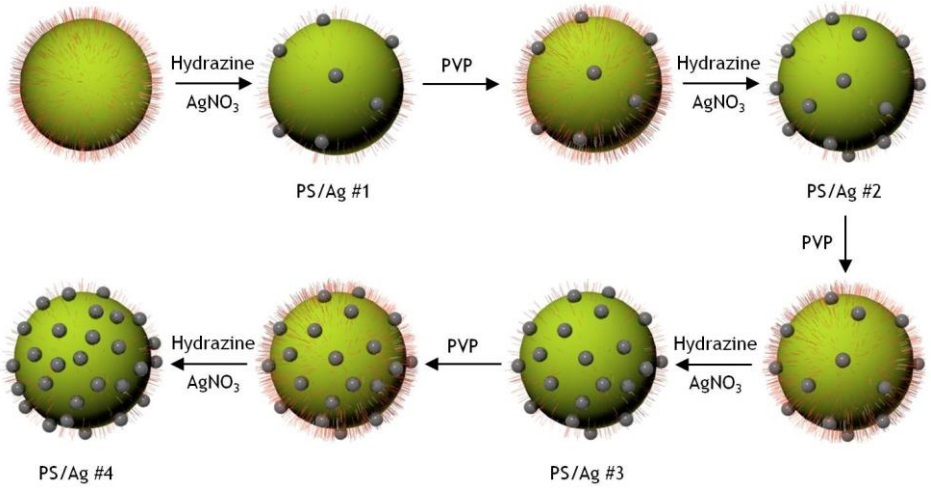

Figure 5. 10. Schematic illustration for the preparation of PS/Ag HNSs by repeated reduction of Ag NPs.

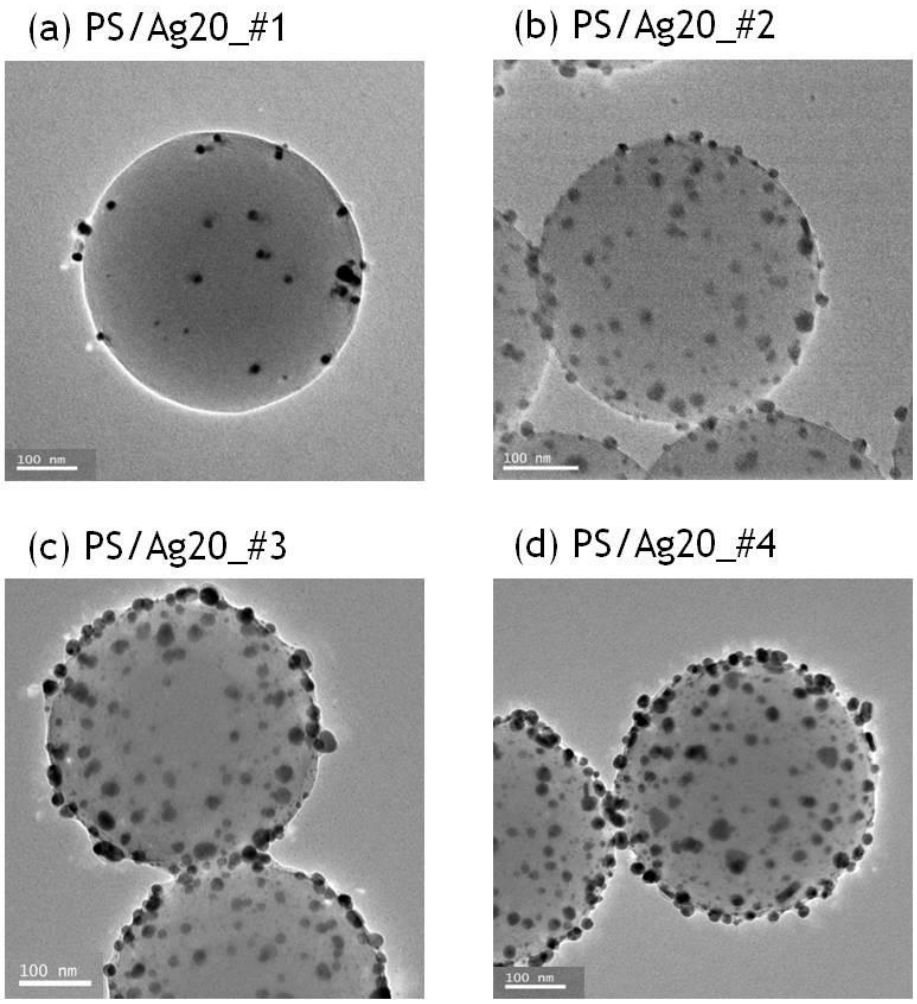

Figure 5. 11. TEM images of (a) PS/Ag20_#1, (b) PS/Ag20_#2, (c) PS/Ag20_#3, and (d) Ps/Ag20_#4.

Table 5. 1. Absorbance of Ag/SiO_2 HHSs as a function of loading amount of Ag NPs

	# Density of Ag NPs (each/NS)	**Weight of Ag NPs (mg/NS)**	**Absorbance (%)**	**Peak λ (nm)**
$Ag/SiO_2$20_#1	18.5	1.99	1.71	379
$Ag/SiO_2$20_#2	48.3	5.22	8.71	374
$Ag/SiO_2$20_#3	75.1	8.28	18.15	380
$Ag/SiO_2$20_#4	98.7	10.98	26.96	384

5. 3. 2. Preparation of Ag/SiO_2 Monolayer Coated Substrates

To form the monolayered $PS/Ag/SiO_2$ arrays on the sapphire substrates, the layer-by-layer deposition method based on electrostatic interaction was applied. The surface charge of sapphire substrates was first modified using polyelectrolytes. PAH, positively-charged polyelectrolyte, and PSS, negatively-charged polyelectrolyte, were alternately deposited on sapphire substrate. The surface charge of sapphire substrates was manipulated by control of sequence of PAH/PSS multilayered films. The positively-charged surface was obtained with PAH/PSS/PAH multilayered film coated substrates. The uniform and monolayered $PS/Ag/SiO_2$ arrays were formed with positively-charged substrates. The reason of uniform deposition of $PS/Ag/SiO_2$ HNSs was electrostatic interaction between positively charged substrate and negatively charged $PS/Ag/SiO_2$ surface. The surface coverage of $PS/Ag/SiO_2$ was varied with dipping time. As the dipping time increased, the surface coverage of $PS/Ag/SiO_2$ also increased. The monolayered Ag/SiO_2 was obtained by calcinations of monolayered $PS/Ag/SiO_2$ and the surface coverage of Ag/SiO_2 monolayer was same with $PS/Ag/SiO_2$ monolayer (see Figure 5. 12).

To investigate the influence of Ag loading amount on coating property, we prepared $PS/Ag/SiO_2$ monolayers with different Ag loading amount. 4 types of $PS/Ag/SiO_2$ HNSs ($PS/Ag/SiO_2$20_#1-4) were deposited on substrate with different dipping time, 60, 120, and 240 s. All the $PS/Ag/SiO_2$ HNSs formed uniform and monolayered arrays and showed almost same surface coverage with same dipping time regardless of Ag loading amount (see Figure 5. 13).

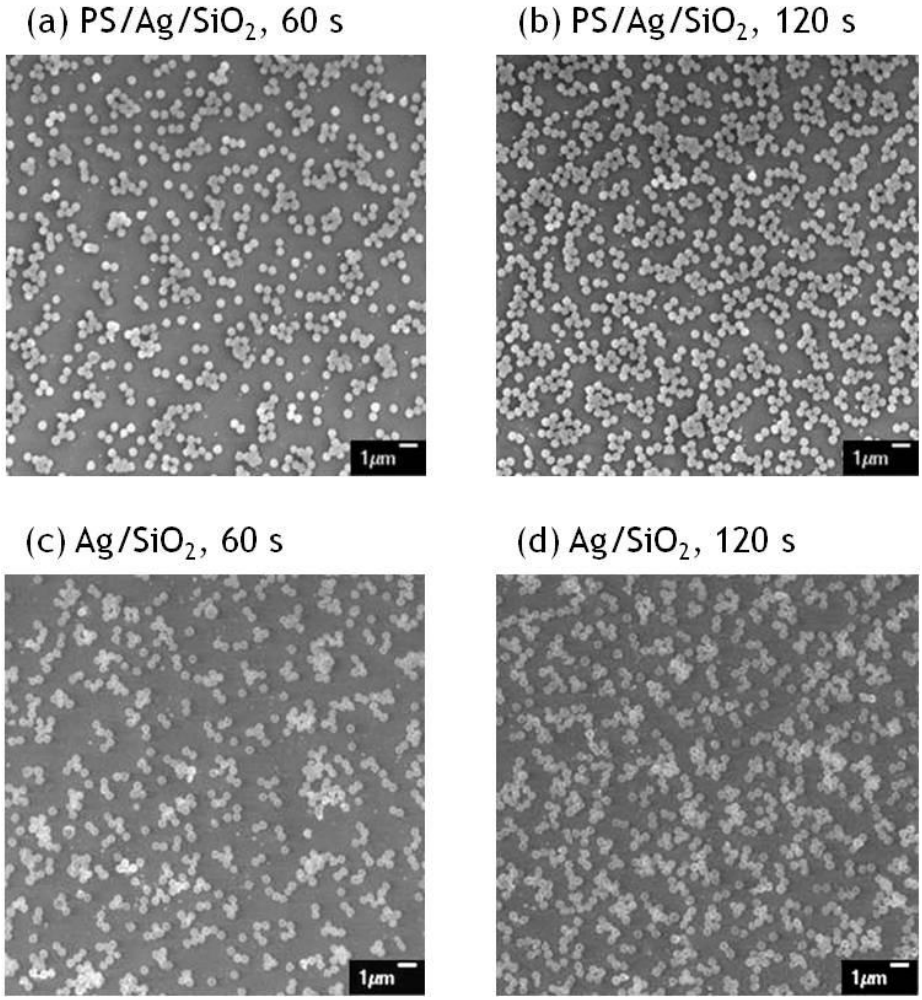

Figure 5. 12. Morphology of $PS/Ag/SiO_2$ monolayers with (a) 60 s and (b) 120 s of dipping time and Ag/SiO_2 monolayers after calcination with (c) 60 s and (d) 120 s of dipping time.

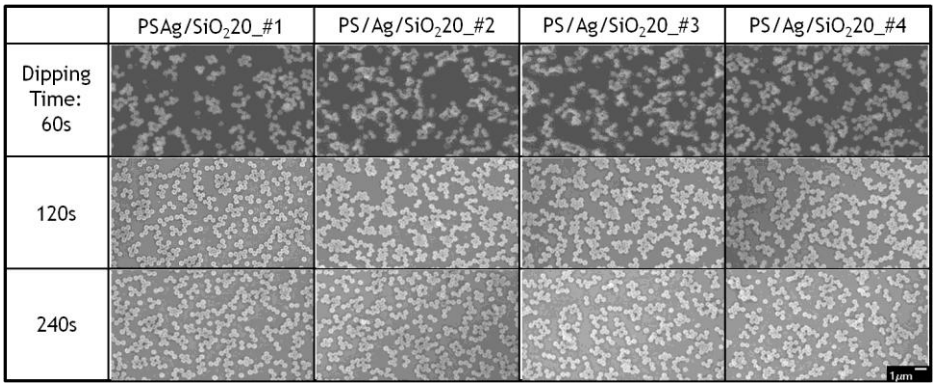

Figure 5. 13. Morphology of Ag/SiO_2 HHSs with different particle type and dipping time.

5. 3. 3. Reflectivity of Ag/SiO_2 Monolayers

To determine the effect of Ag NPs on the reflectivity, the reflectance of Ag/SiO_2 monolayer was measured with UV-Vis-NIR spectrometer combined with an integrating sphere detector. The reflectance of HSS monolayer without Ag NPs, reference sample, 20 nm-sized Ag NPs containing HHS, and 80 nm-sized Ag NPs containing HHS were used for characterization and the surface coverage of hollow sphere monolayers was fixed at 30 % (see Figure 5. 14). The reflectance of HSS monolayer without Ag NPs, reference sample, was 14.5 % of reflectance at 500 nm. The Ag/SiO_2 monolayers with 20 nm-sized Ag NPs and 80 nm-sized Ag NPs showed 15.9 and 20.4 % of reflectance at 500 nm, respectively (see Figure 5. 15). The reflectance of 20 nm-sized Ag NPs containing sample was slightly increased when compared with reference sample. On the other hand, the increase of reflectance of 80 nm-sized Ag NPs containing sample was far higher than 20 nm-sized Ag NPs containing sample. We assume that the reason of difference in the increase of reflectance is surface coverage of the Ag NPs. Because 80 nm-sized Ag NPs have relatively large cross-sectional area than 20 nm-sized Ag NPs, the surface coverage of 80 nm-sized Ag NPs also have larger surface coverage than 20 nm-sized Ag NPs. Due to the larger surface coverage, 80 nm-sized Ag NPs reflected way more visible light. The increase of reflectance at short wavelength region is smaller than the increase of reflectance at long wavelength region due to the light absorption by Ag NPs around 400 nm.

To confirm the influence of the Ag NP loading amount on the reflectivity, the reflectance of Ag/SiO_2 monolayers with different Ag NP # density was

measured (see Figure 5. 16). The average size of Ag NPs was about 20 nm. All the samples showed almost same reflectance regardless of the Ag NP loading amount because the size of Ag NPs were not enough large to reflect light effectively. Consequently, we assume the size of Ag NPs have to be risen to increase the reflectivity of Ag/SiO_2 HHSs.

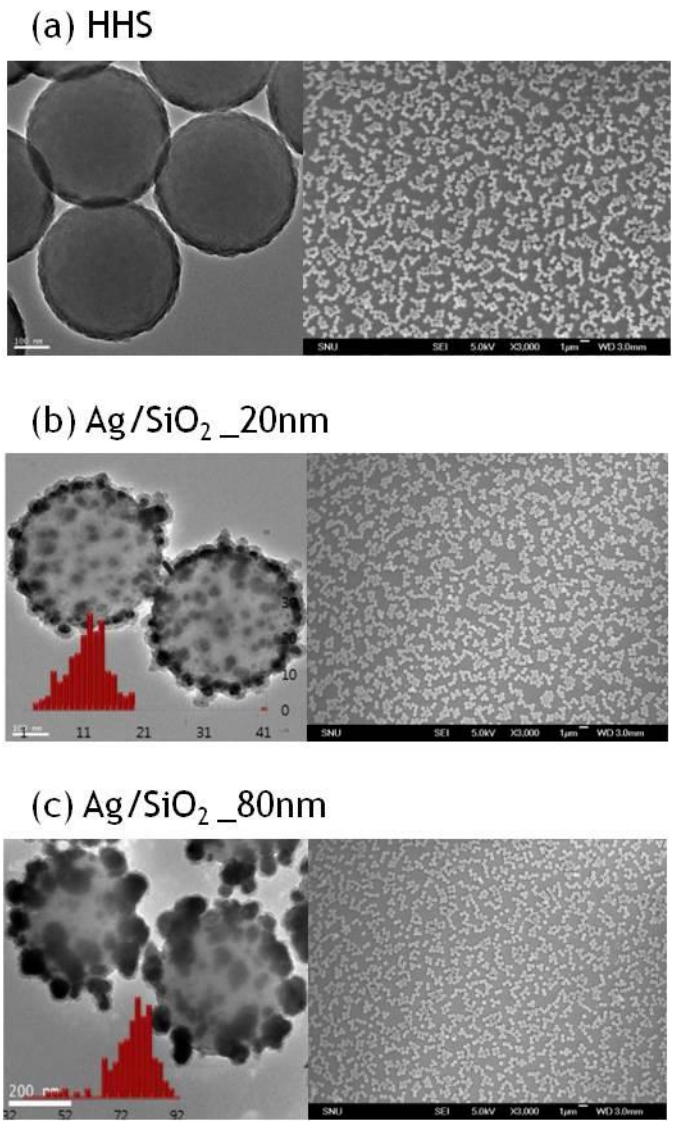

Figure 5. 14. TEM images (left) and monolayers (right) of (a) HSS, (b) Ag/SiO_2 HHS (20 nm-sized Ag NPs), and (c) Ag/SiO_2 HHS (80 nm-sized Ag NPs).

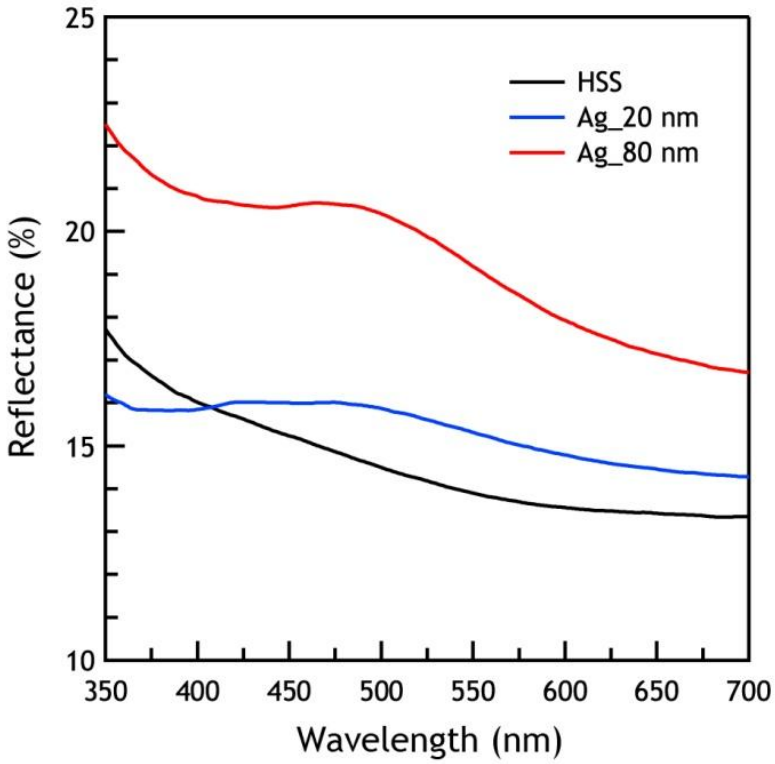

Figure 5. 15. Reflectance of HSS, Ag/SiO_2 HSSs containing 20 nm- and 80 nm-sized Ag NPs monolayers with 30 % of surface coverage.

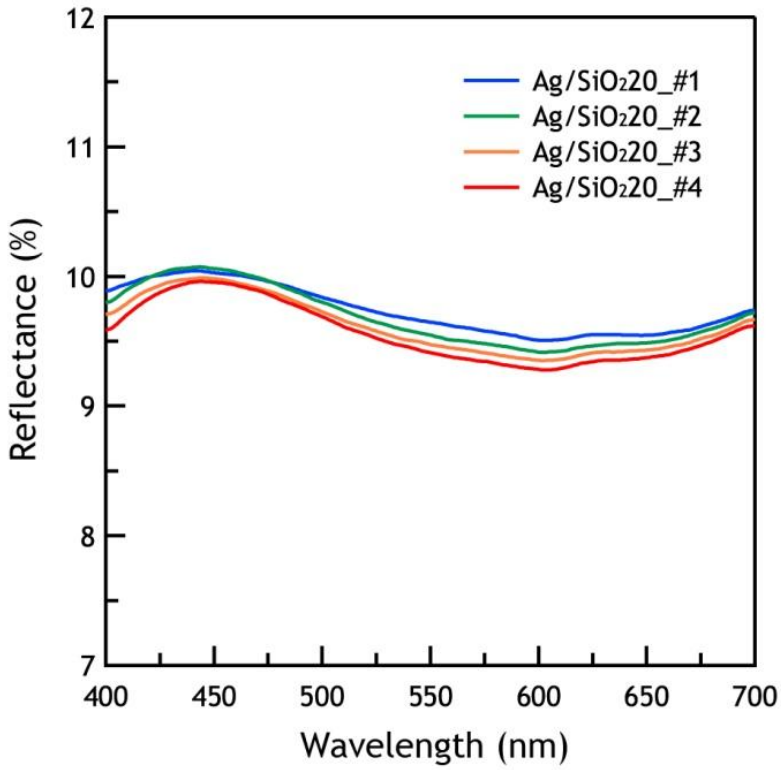

Figure. 5. 16. Reflectance of Ag/SiO_2 HSS monolayers with different Ag NPs amounts.

5. 3. 4. Light Absorption Property of Ag/SiO_2 Monolayers

For the comparative study on the light absorption property of Ag NPs within Ag/SiO_2 HHSs, we first characterized absorbance change of pristine Ag NP dispersions with different concentration. The absorbance of pristine Ag NP dispersions with 0.5, 1.0, 2.0, 4.0, and 8.0 mg/L of concentration was measured with UV-Vis spectrometer (see Figure 5. 17(a)). The absorbance of pristine Ag NPs linearly increased according to the concentration of the Ag NPs (see Figure 5. 17(b)).

The absorbance change of Ag NPs within Ag/SiO_2 HHS also characterized according to the loading amount of the Ag NPs. The Absorbance of Ag NPs within the Ag/SiO_2 HSSs ($Ag/SiO_2$20_#1 - 4) was measured with UV-Vis-NIR spectrometer combined with an integrating sphere detector (see Figure 5. 18(a)). The surface coverage of Ag/SiO_2 HHSs was fixed at 30 %. While the absorbance of pristine Ag NPs increased linearly according to the concentration of the Ag NPs, the absorbance of Ag NPs within the Ag/SiO_2 HHSs was more rapidly increased according to the # density of Ag NPs (see Figure 5. 18(b)). The absorbance of Ag NPs with 18.5, 48.3, 75.1, and 98.7 each/NS of # density showed 1.7, 8.7, 18.2, and 27.0 % of absorbance, respectively. The # density of Ag NPs was converted to weight ratio of Ag NPs, and the absorbance of Ag NPs was characterized according to the weight ratio. Similar to the case of # density, the absorbance of Ag NPs within the Ag/SiO_2 HHSs was also more rapidly increased according to the weight ratio when compared with linear increase of pristine Ag NPs (see Figure 5. 18(c)). We expect that the reason of rapid increase of absorbance is due to the

enhanced coupling effect of surface Plasmon resonance between Ag NPs within Ag/SiO_2 HSSs.[20, 21] As the # density of Ag NPs within Ag/SiO_2 HSSs was increased, the interparticle distance of Ag NPs was decreased. Because the coupling effect of surface Plasmon resonance between Ag NPs is depend on interparticle distance of Ag NPs, the coupling effect is enhanced with larger # density of Ag NPs. As a result, the light absorption by the Ag NPs within Ag/SiO_2 HHSs was enhanced.

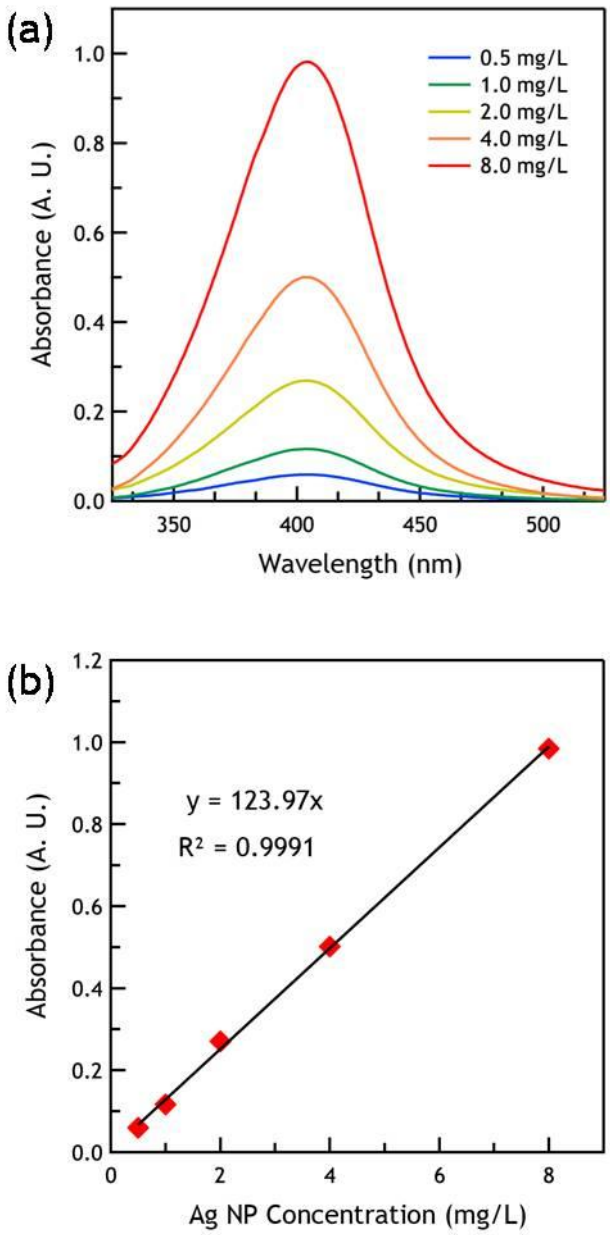

Figure 5. 17. (a) Absorption spectra and (b) absorbance of pristine Ag NP dispersions with different concentration.

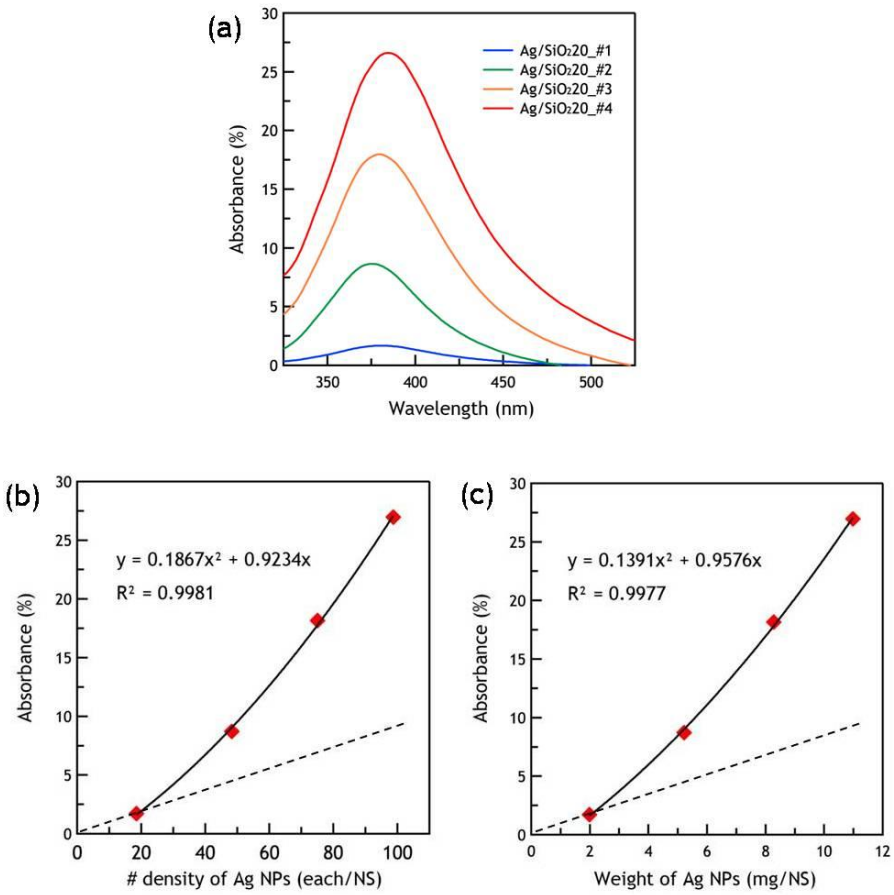

Figure 5. 18. (a) Absorption spectra of Ag/SiO_2 monolayers with different # density of Ag NPs. Absorbance of Ag/SiO_2 monolayers with different # density of Ag NPs as a function of (b) # density and (c) weight of Ag NPs.

5. 4. Conclusion

PS/Ag HNSs were prepared using PS NSs as a template, $AgNO_3$ as a Ag precursor, and hydrazine hydrate as a reducing agent. The size and the # density of Ag NPs were manipulated by varying the solvent mixing ratio, the molecular weight of PVP, and the concentration of reactants. PS/Ag/SiO_2 HNSs were then prepared using PS/Ag HNSs and TEOS, silica precursor. The Ag/SiO_2 monolayers were formed on the quartz substrate based on electrostatic interaction. The Ag/SiO_2 monolayers showed enhanced reflectivity when compared with HSS monolayer without Ag NPs due to the high reflectivity of Ag NPs. Furthermore, The Ag/SiO_2 monolayers presented improved light absorption property when compared with pristine Ag NPs due to the enhanced coupling effect of surface Plasmon resonance between Ag NPs within Ag/SiO_2 HSSs.

5. 5. References

(1) Ç ulha, M.; Kahraman, M.; Tokman, N.; Tükoğlu, G. *J. Phys. Chem. C* **2008**, *112*, 10338.

(2) Stranahan, S. M.; Titus, E. J.; Willets, K. A. *ACS NANO* **2012**, *6*, 1806.

(3) Shen, L.; Ji, J.; Shen, J. *Langmuir* **2008**, *24*, 9962.

(4) Southward, R. E., Thompson, D. W.; Clair, A. K. St. *Chem. Mater.* **1997**, *9*, 501.

(5) Chen, Y.-S., Tal, A.; Torrance, D. B.; Kuebler, S. M. *Adv. Funct. Mater.* **2006**, *16*, 1739.

(6) Dror-Ehre, A.; Mamane, H.; Belenkova, T.; Markovich, G.; Adin, A. *J. Colloid Interf. Sci.* **2009**, *339*, 521.

(7) Mahmoudi, M.; Serpooshan, V. *ACS NANO* **2012**, *6*, 2656.

(8) Jiang, Z.-J.; Liu, C.-Y.; Sun, L.-W. *J. Phys. Chem. B* **2005**, *109*, 1730.

(9) Jiang, H.; Moon, K.; Li, Y.; Wong, C. P. *Chem. Mater.* **2006**, *18*, 2969.

(10) Oliveira, M. M.; Ugarte, D.; Zanchet, D.; Zarbin, A. J. G. *J. Colloid Interf. Sci.* **2005**, *292*, 429.

(11) Kelly, F. M.; Johnston, J. H. *ACS Appl. Mater. Interfaces* **2011**, *3*, 1083.

(12) Kang, Y. S.; Kang, S. W.; Kim, H.; Kim, J. H.; Won, J.; Kim, C. K.; Char, K. *Adv. Mater.* **2007**, *19*, 475.

(13) Kang, S. W.; Char, K.; Kim, J. H.; Kim, C. K.; Kang, Y. S. *Chem. Mater.* **2006**, *18*, 1789.

(14) Cassagneau, T.; Fendler, J. H. *J. Phys. Chem. B* **1999**, *103*, 1789.

(15) Kirubaharan, C. J.; Kalpana, D.; Lee, Y. S.; Kim, A. R.; Yoo, D. J.; Nahm,

K. S.; Kumar, G. G. *Ind. Eng. Chem. Res.* **2012**, *51*, 7441.

(16) Maduraiveeran, G.; Ramaraj, R. *Anal. Chem.* **2009**, *81*, 7552.

(17) Xiong, Y.; Washio, I.; Chen, J.; Cai, H.; Li, Z.-Y.; Xia, Y. *Langmuir* **2006**, *22*, 8563.

(18) Yin, B.; Ma, h.; Wang, S.; Chen, S. *J. Phys. Chem. B* **2003**, *107*, 8898.

(19) Huang, H. H.; Ni, X. P.; Loy, G. L.; Chew, C. H.; Tan, K. L.; Loh, F. C.; Deng, J. F.; Xu, G. Q. *Langmuir* **1996**, *12*, 909.

(20) Malynych, S.; Chumanov, G. *J. Am. Chem. Soc.* **2003**, *125*, 2896.

(21) Lu, Y.; Liu, G. L.; Lee, L. P. *Nano Lett.* **2005**, *5*, 5.

국문 초록

유기실리케이트(Organosilicate)는 유기물부를 포함하는 산화규소물질로서, 산화규소 기반의 골조와 유기물 기반의 작용기가 공존함으로 인해 산화규소 고유의 물성과 유기 작용기의 기능성을 동시에 가진다는 장점을 가진다. 또한 유기실리케이트는 우수한 광투명성, 높은 열적 광학적 안정성, 다양한 공정가능성, 조절 가능한 물성 및 생친화성 등의 장점을 가져 지난 수십년간 고기능성 물질로서 주목을 받아왔다. 최근에는 유기실리케이트 기반의 나노물질인 실리카 중공구조체(Hollow Silica Shell) 역시 높은 기능성으로 인해 높은 주목을 받고 있다. 실리카 중공구조체는 내부 중공, 넓은 표면적, 낮은 전기 및 열 전도도, 낮은 밀도 등의 물성으로 인해 나노 약물전달체, 나노 반응기, 고성능 촉매, 저밀도 충진재, 단열재, 난연재 등으로의 응용이 가능하며, 많은 연구그룹으로부터 실리카 중공구조체를 기반으로 하는 다기능성 나노 하이브리드 물질에 대한 연구 결과가 보고되고 있다. 본 연구에서는 유기실리케이트 고분자 및 실리카 중공구조물을 기반으로 하는 다기능성 하이브리드 물질을 제조하고 이를 다양한 응용분야에 적용하는 연구를 수행하였다.

제 1장에서는 유기실리케이트와 실리카 중공구조체의 장점 및 응용가능성에 대해 간략히 서술하였으며, 제 2장에서는 Thiol 작용기를 가지는 유기실리케이트 리간드를 이용하여 양자점(Quantum Dot)을 표면치환하고 표면치환된 양자점을 유기실리케이트 매트릭스에 분산시켜 양자점/유기실리케이트 하이브리드를 제조하는 연구 결과를 보고하였다. 양자점 표면과 강한 반응성을 가지는 Thiol 작용기로 인해 양자점 표면을 효과적으로 치환할 수 있었고, 표면치환된 양자점은 양자점 고유의

높은 광학적 특성을 유지하면서 유기실리케이트 매트릭스와 높은 친화성을 보였다. 또한 양자점을 매트릭스 내에 균일하게 분산함으로써 다양한 장점을 얻을 수 있었으며, 그 첫째로 양자점을 매트릭스 내에서 응집되지 않도록 함으로써 양자점의 효율을 감소시키는 원인 중 하나인 농도소광(Concentration Quenching)을 최소화 하였다. 둘째로는 양자점을 유기실리케이트 매트릭스 내부에 깊이 담지시킴으로써 외부 자극으로부터 양자점을 효과적으로 보호할 수 있도록 하였고, 셋째로는 매트릭스 내에서 양자점이 거대응집체를 이루지 않게 함으로써 양자점으로 인한 광산란을 최소화하여 유기실리케이트 고유의 우수한 광투명성을 유지할 수 있도록 하였다. 또한 유기실리케이트 고유의 뛰어난 공정성으로 인해 단순한 용액공정으로 손쉽게 대면적의 박막 제조가 가능하였고, 더불어 비 전통적 패터닝 방법을 통해 균일한 양자점/유기실리케이트 패턴 제조가 가능하였다.

제 3장에서는 가시광선 영역에서 높은 광투명성을 가지는 실리카 중공구조체 표면에 자외선 차단기능을 가지는 타이타니아(Titania) 층을 형성시키고 이를 유기실리케이트 매트릭스 내에 담지하여 다기능성 하이브리드 단열막을 제조하는 연구 결과를 보고하였다. 가시광 하에서 투명한 작은 크기의 실리카 중공구조체를 합성하기 위해 50 nm 이하의 작은 고분자 응집체를 템플레이트로 사용하였으며, 실리카 껍질 및 타이타니아 층은 모두 Sol-Gel 반응을 통해 손쉽게 제조할 수 있었다. 제조된 하이브리드 단열막은 높은 광투명성을 유지하면서 타이타니아로 인한 자외선 차단효과 및 내부의 중공 구조로 인한 열 전도도 감소효과를 보였다.

제 4장에서는 실리카 중공구조체가 코팅된 사파이어 기판을 이용하여 높은 결정성과 낮은 결함밀도를 가지는 GaN 박막을 성장시키고, 이를 이용하여 고휘도 GaN LED를 제조하는 연구 결과를 보고하였다. 실리카 중공구조체는 균일한 배열의 단일층

형태로 사파이어 기판 위에 도포 되었으며 GaN 박막 성장시 GaN의 수평에피성장(Epitaxial Lateral Overgrowth)을 유도하는 마스크 역할로 도입되었다. 또한 실리카 중공구조체로 인해 기판 표면에 만들어진 요철 구조는 빛의 난반사를 유도하고, 내부 중공으로 인한 GaN 박막의 굴절률 감소는 GaN 박막과 사파이어 기판의 굴절률 차에 의한 전반사효과를 완화시켜 GaN LED의 외부양자효율을 증가시키는 효과를 보였다. 이와 더불어 실리카 중공구조체가 GaN의 고온성장과 냉각시 발생하는 응력을 완화시켜줌으로써 기판의 휨현상을 감소시켜주는 역할을 하였다. 이러한 방법은 손쉬운 Sol-Gel 반응과 용액공정을 통해 이루어져 기존의 실리카 마스크 또는 패턴된 사파이어 기판을 이용하는 GaN 성장법 대비 훨씬 적은 비용과 공정조건이 요구되며 또한 실리카 중공구조체의 도입을 통해 다양한 효과를 동시에 가져올 수 있다는 장점을 가진다.

제 5장에서는 내부에 은 나노입자가 담지된 하이브리드 실리카 중공구조체를 제조하고 그 광학적 특성을 분석하는 연구 결과를 보고하였다. 은 나노입자는 PVP가 흡착된 폴리스티렌 입자 표면에 은 이온을 직접 환원시키는 방법으로 합성하였으며, 합성된 은 나노입자의 크기와 입자 밀도는 반응물의 농도, 용매의 혼합비, PVP의 분자량 등을 조절함으로써 제어할 수 있었다. 은 나노입자가 코팅된 폴리스티렌 입자 표면에 실리카 껍질을 형성시키고, 폴리스티렌 입자를 열분해 방법을 통해 제거함으로써 은 나노입자가 담지된 실리카 중공구조체를 제조할 수 있었으며 이를 기판위에 도포하여 광학적 특성을 관찰하였다. 반사도 측정결과 은 나노입자의 높은 반사율로 인해 기판의 반사도가 증가하는 효과를 보였으며 반사도 증가 효과는 은 나노입자의 크기가 클 수록 배가되었다. 또한 은 나노입자의 광흡수도 분석 결과 은 나노입자의 입자 밀도가 증가함에 따라 광흡수도 증가율이 더 빠르게 증가하는

현상이 관찰되었다. 이는 실리카 중공구조체 내부에 존재하는 은 나노입자의 밀도가 증가함에 따라 입자 간의 거리가 감소하고 이에 기인하여 은 나노입자의 표면플라즈몬공명(Surface Plasmon Resonance)의 커플링(Coupling) 효과가 증폭된 결과이다.

주요어: 유기실리케이트, 하이브리드, 실리카 중공구조체, LED(s), GaN, 광학(소자), 광전자(소자), 단열, 은 (나노입자)

학번: 2006-21360